Development of a method to study inter-organelle lipid transport *in vivo*: mammalian Betaine Lipid Transport (mBLT)

Camille Laurent

St. Hughs College
Department of Biochemistry
University of Oxford

Thesis submitted for the degree in Master of Science by Research in Biochemistry

January 2026
Word Count: 21,824

Acknowledgements

I would like to thank my supervisor Dr. Benoit Kornmann for giving me the opportunity to work in his wonderful lab, where scientific questions are explored with genuine creativity, curiosity and depth. I learned a lot from my experience about the nonlinear process of research, about the non-intuitive value of negative results, and about the joy that a good experiment can bring.

To my primary supervisor, Dr. Ying-Chen Lin, thank you for patiently guiding me through this project. Above all I am grateful for your kindness, which made me feel at home in the big world of academia. I am also thankful for Dr. Christian Coville-Cooke, Dr. Agnes Michel, and Anitha Nair who were very generous with their time, and wonderful people to work alongside every day.

Dr. James Holder, thank you for sharing your expertise with mammalian cell culture and alongside Dr. Elisa Vitello, making the general lab environment an exciting and supportive one.

Dame Dr. Carol Robinson, thank you greatly for allowing me to use the Orbitrap Eclipse for my lipidomics analyses. This work would not have been possible without the help of Dr. Carla Kirschbaum, whose expertise in mass spectrometry was instrumental in shaping this project, and enabled its development into something truly promising and even more exciting. It was a privilege to work with you and learn

from you. Jack Bennett, thank you for taking the time to show me how to perform better analyses on my data, and exploring possible refinements to my methods.

Matt, Izzy, Ava, Michael, Yaks, Alex, and Cara thank you for being the best lab mates that I could have asked for. I will cherish the memories that I have of our time together both in and outside of the lab.

Finally, to Mom, Dad, Charlotte, and Emma, thank you for providing me with the love and support that I needed to finish this project. I would not have been able to maintain my sanity if not for your reassurance and encouragement throughout this - I am extremely grateful for you, and extremely lucky to have you. Finally, I'd like to give a shoutout to my Australian shepherd (and best friend), Oliver, who makes me laugh and smile every day.

Table of Contents

Abstract

Studying lipid transport *in vivo* has remained a major challenge. This is because transport occurs through vesicular trafficking as well as through lipid transfer proteins, many of which exhibit redundancies and function in a context-dependent manner. By confining the stepwise synthesis of betaine lipids across two membranes, betaine lipid transport (BLT) provides a biorthogonal strategy to study lipid transport *in vivo* with spatial and temporal control. Betaine lipids synthesis proceeds via two successive enzymatic reactions: BtaA converts diacylglycerol (DAG) to DGHS, which is then converted to DGTS by BtaB. In BLT, BtaA and BtaB are artificially targeted to any two membranes, such that the accumulation of DGTS serves as a readout for directional lipid transport; in combination with metabolic labelling, temporal changes in transport can be assessed. This study strongly demonstrates the feasibility of adapting BLT for use in mammalian cells, following its initial development in yeast. Due to the complexity of the mammalian lipidome versus that of yeast, single quadrupole mass spectrometry did not provide adequate resolution for the robust detection of betaine lipids. Tandem mass spectrometry was therefore required to confirm ectopic betaine lipid synthesis and demonstrate that co-expression of BtaA and BtaB could report on basal lipid transport. However, low lipid abundance ultimately limited an assessment of changes in lipid transport during mitophagy, which provides an ideal context for obtaining proof-of-concept for mBLT. To guide further development, this study outlines the key biological and technical constraints which must be addressed to enable robust quantification of lipid transport using mBLT.

Abbreviations

BLT — Betaine Lipid Transport

Bta1 — Betaine Lipid Synthase (Full-Length)

BtaA — Betaine Lipid Synthase (Domain A, carboxypropyltransferase)

BtaB — Betaine Lipid Synthase (Domain B, methyltransferase)

C18 — Octadecylsilane

CCCP — Carbonyl cyanide m-chlorophenyl hydrazone

CMS — Compact Mass Spectrometer

DDA — Data Dependent Acquisition

DGHS — Diacylglyceryl-hydroxymethyl-β-homoserine

DGTS — Diacylglyceryl-N,N,N-trimethylhomoserine

DOX — Doxycycline

EIC — Extracted Ion Chromatogram

ERMES — Endoplasmic Reticulum Mitochondria Encounter Structure

FLAG — Hydrophobic peptide (DYKDDDDK)

FWHM — Full Width Half-Maximum

HILIC — Hydrophilic Interaction Liquid Chromatography

HPLC — High-Performance Liquid Chromatography

IMM — Inner Mitochondrial Membrane

IS — Internal Standard

LTP — Lipid Transfer Protein

MCS — Membrane Contact Site

METALIC — Mass Tagging-Enabled TrAcking of Lipids in Cells

MRN — Median-of-Ratios Normalization

MS — Mass Spectrometry

MS-DIAL — Mass Spectrometry Data Independent AnaLysis

MS/MS — Tandem Mass Spectrometry

OMM — Outer Mitochondrial Membrane

ORP — Oxysterol-Binding Protein-Related Protein

P2A — Porcine Teschovirus-1 Self-Cleaving 2A Peptide

PM — Plasma Membrane

RSLC — Rapid Separation Liquid Chromatography

SAM — S-adenosyl Methionine

SATAY — Saturated Transposon Analysis in Yeast

SIM — Selected Ion Monitoring

SMP — Synaptotagmin-like Mitochondrial Lipid-Binding Protein

SRM — Selected Reaction Monitoring

StARkin — Steroidogenic Acute Regulatory (StAR) Protein-Related Lipid-Transfer Domain Superfamily

TLC — Thin-Layer Chromatography

TMD — Transmembrane Domain

TMEM16 — Transmembrane Protein 16

TOM20 — Translocase of Outer Mitochondrial Membrane 20kDa Subunit

TREx — Tetracycline-Regulated Expression System

TULIP — Tubular Lipid-Binding Protein Domain Superfamily

VAP — VAMP-Associated Protein

Introduction:

Foreword

The structure and function of biological membranes are dictated by the diversity and relative abundance of their fundamental building blocks: lipids. At the level of bulk composition, lipid profiles vary substantially between organs, tissues, cell types, and intracellular organelles, implying that distinct lipid environments are required to support specialized functions. However, how cells establish and maintain this compositional diversity remains poorly understood. Cellular lipid diversity rivals that of protein diversity, yet lipid function, metabolism, and transport remain far less comprehensively characterised. By and large, this disparity can be attributed to the fundamental difference in their biogenesis: unlike proteins, lipids are not genomically encoded but are instead produced via highly interconnected biochemical networks that necessarily rely on efficient transport mechanisms. Lipid transport, which includes both vesicular and non-vesicular mechanisms, not only shapes the membrane compositions of individual organelles but also enables their rapid remodelling in response to cellular demands. Despite such central importance, we have not yet been able to disentangle the redundancy of these lipid transport pathways nor their relative contributions to organelle membrane homeostasis, which is frequently perturbed in disease. This is largely due to the absence of experimental methods capable of resolving the spatial and temporal specificity with which inter-organelle lipid transport occurs.

The classification of lipids and their cellular roles

The molecular structure of lipids governs their classification into three major classes in eukaryotes: glycerolipids, sphingolipids, and sterols. These lipid classes differ principally in their hydrophobic backbones, where a glycerolipid contains a glycerol esterified to two fatty acyl chains at the *sn*-1 and *sn*-2 positions, where stereospecific numbering (*sn*) defines any of the three glycerol carbons. By contrast, sphingolipids are based on a sphingosine base, in which a single fatty acyl chain is amide-linked to the C2 amino group, with the sphingosine backbone itself providing the second hydrophobic moiety. Sterols instead comprise a rigid, fused tetracyclic ring system and lack esterified fatty acyl chains. Across lipid classes, chemical diversity arises through distinct but related mechanisms. In glycerolipids and sphingolipids, variation in fatty acyl chain length, degree of unsaturation, and double-bond position contributes substantially to molecular diversity. Additional diversity arises from variation in the polar headgroups attached to their hydrophobic backbones. Despite vast differences in chemical structure, the cellular roles of lipids can be generalized into structural (membrane-forming) roles, or roles involved in signalling, or energy storage. Crucially, neither the structure nor function of a lipid is static: lipid structure can be remodelled at the level of their acyl-chains or turnover of their polar headgroup. Indeed, lipid functions can be highly context dependent, such that a lipid which primarily resides within the membrane can suddenly assume a signalling role.

Lipid biogenesis and transport via vesicular trafficking:

Eukaryotic cells harbour an elaborate endomembrane system that constitutes the endocytic and secretory pathways, which are indispensable for cellular homeostasis. The secretory pathway delivers proteins synthesised at the endoplasmic reticulum (ER) to distinct membrane-bound organelles, including the Golgi apparatus, early and late endosomes, the plasma membrane (PM), and lysosomes. The transport of ER-derived proteins relies on tightly regulated vesicular trafficking events, in which transport vesicles bud from one membrane-bound compartment and fuse with another. The functional identity of each organelle is defined not only by its protein complement, but also by the lipid composition of its membranes, and consequently that of the vesicles that traffic to and from it (Bonifacino and Glick 2004; van Meer et al. 2008). Thus, the secretory pathway provides a major route for the transport of lipids synthesized at the ER, which is the principal site of synthesis for the bulk of phospholipids, cholesterol as well as substantial amounts of triacylglycerol (TAG), sterol esters, and ceramide which serves as the precursor for complex sphingolipids which are primarily synthesized at the Golgi (Holthuis and Menon 2014; Stefan et al. 2017). However, lipid composition is not simply inherited from donor membranes. Following delivery to a given compartment, lipid species are selectively metabolised. Therefore, local enzymatic activity, or more broadly put, local lipid metabolism, constitutes a major determinant of the steady-state lipid composition of an organelle.

Non-vesicular lipid transport between leaflets or at membrane contact sites (MCS)

While vesicular trafficking delivers bulk lipid material to organelles, membrane lipids are not homogeneously distributed following delivery. Lipid organization is structured both laterally, with segregation into compositionally distinct domains, and in trans, through asymmetric distribution between two membrane leaflets. Spontaneous so-called lipid flip-flop can occur between two leaflets; however, this process occurs very slowly. Lipid asymmetry is therefore actively maintained by the activity of type IV P-type ATPases, canonically referred to as flippases, which confine specific phospholipids to the cytosolic leaflet of membranes by translocation or flipping from the luminal leaflet (Coleman et al. 2013). Such asymmetry can also be disrupted by the activity of lipid scramblases. For example, scramblases of the transmembrane protein 16 (TMEM16) family function in a Ca^{2+}-dependent manner, while members of the XK-related family function in a caspase-dependent manner to effectively scramble phospholipids between leaflets in a bi-directional, energy-independent manner (Suzuki et al. 2013; Falzone et al. 2018). The activity of flippases and scramblases are particularly important in the context of lipid-mediated signalling, where regulated changes in phospholipid topology can generate distinct functional outcomes. For example, during apoptosis, phosphatidylserine (PS) becomes exposed on the outer leaflet of the plasma membrane, typically through inhibition of flippase activity together with activation of scramblases; at the outer leaflet PS functions as an “eat-me” signal to promote efferocytosis by phagocytes (Yeung et al., 2008; Leventis and Grinstein, 2010).

While flippases and scramblases control lipid redistribution between the two leaflets of a single bilayer, analogous energetic and kinetic constraints also limit the

spontaneous exchange of lipids between two different organellar membranes. The existence of dedicated proteins which solve this problem was first implicated over 50 years ago using an *in vitro* liposome exchange assay, which led to the purification of a soluble protein capable of catalyzing the transfer of phosphatidylinositol (PI) between distinct liposome populations (Helmkamp et al., 1974). Since then, hundreds of lipid transfer proteins (LTPs) have been identified, most of which function at membrane contact sites (MCSs): regions of close (10-30nm) apposition between two organelles (Voeltz et al. 2024). Beyond lipid transfer, MCSs function as organizational hubs that coordinate organelle division, trafficking, biogenesis, as well as signalling between them.

The structures and conformations adopted by LTPs are extremely diverse, where shared folds among certain families do not necessarily imply shared specificities for certain lipids. To access lipids for transport and to direct their disposal, LTPs contain well-conserved motifs or domains that allow for their targeting to two different organelles (Prinz 2014). In some cases, such targeting is achieved through stable anchoring via transmembrane domains or constitutive association with local adaptor proteins (Murley et al. 2015). However, organelle targeting can also be reversible, and context-dependent (Loewen et al. 2003; Chang et al. 2013). In some cases, LTP targeting is favoured by their association with adjacent LTPs (Tong et al. 2018). Nonetheless, LTPs are unified in their ability to provide a hydrophobic environment for lipids to traverse the aqueous cytosol. Members of the well-conserved kin of relatives (kin) of steroidogenic acute regulatory protein (StARkin) superfamily, as well as the oxysterol-binding protein (OSBP)-related proteins (ORPs), typically

function in single units as “box” shuttles, where a lipid is extracted from the donor membrane, enclosed within an internal cavity, and shuttled across the cytoplasm for deposition into an acceptor membrane (Raychaudhuri et al. 2006; Chung et al. 2015; Wong and Levine 2016). LTPs that use this transport mechanism rely on transient interactions with donor and acceptor membranes, with close membrane apposition maintained by other proteins known as tethers. Other LTPs are bridge-like, forming a continuous lipid-binding path in which membrane tethering is directly coupled to lipid transfer. Bridge-like LTPs can also be multimeric, as exemplified by the ER-mitochondrial encounter structure (ERMES), a multi-protein complex that mediates phospholipid transfer between the ER and mitochondria in yeast (Kornmann et al., 2009). In such systems, multiple proteins containing synaptotagmin-like mitochondrial lipid-binding protein (SMP) domains can assemble via head-to-head dimerization to generate an extended hydrophobic seam that supports lipid movement between membranes (Wozny et al. 2023; Schauder et al. 2014). However, it has become increasingly plausible that multimeric LTP complexes do not adopt a single productive conformation but instead interconvert between a few different ones (Kawano et al., 2018). One appealing interpretation of this modularity is that complex assembly and architecture can be tuned to the distance between the apposed organellar membranes (Covill-Cooke et al. 2024). Additionally, just as redundancy exists at the level of lipid metabolic pathways, multiple LTPs and tethering proteins can operate in parallel at the same membrane contact site. At the ER-plasma membrane contact site, for instance, lipid exchange is mediated by extended synaptotagmins (E-Syts) 1-3, as well as the box-like LTPs ORP5, ORP8,

and ORP2 which depend on the tethering activity of VAMP-associated proteins (VAPs) (Loewen et al. 2003; Hewlett et al. 2021; Nath et al. 2020). An unresolved question relates to how these overlapping transport routes quantitatively contribute to net lipid inter-organelle transport and to what extent this depends on the sustainment of membrane contact sites by the tethering proteins.

LTPs contribute substantially to local lipid supply not only for organelles outside the secretory pathway, such as mitochondria or peroxisomes, but also for membranes that are classically served by vesicular trafficking. In doing so, LTP-mediated transport is not likely redundant to vesicular transport but instead complements it by satisfying temporal and spatial requirements for delivery that bulk transport cannot meet. Consistent with this idea, early biochemical estimates revealed that the rate of phosphatidylcholine (PC) exchange between the endoplasmic reticulum and the plasma membrane is substantially faster than can be accounted for by vesicular transport alone (Kaplan and Simoni, 1985). The physiological importance of LTP-mediated transport is further underscored by processes that impose particularly stringent temporal or spatial constraints. The need for rapid replenishment of PI to generate PI(4,5)P_2 during sustained signalling at the plasma membrane (Kim et al., 2015), or the rapid formation and expansion of phagophore membranes during autophagy (Mari et al. 2011; Hollenstein and Kraft 2020) represent such examples.

While vesicular-mediated lipid transport is often directional and concerted, LTP-mediated transfer can be biased by several distinct mechanisms that impose directionality on a process which is otherwise rate-limited by lipid desorption or

diffusion. One common strategy is counter-exchange, typical of bispecific LTPs, in which a steep gradient of one lipid, maintained by localized synthesis and turnover, provides the thermodynamic drive to move a second lipid in the opposite direction (de Saint-Jean et al. 2011; Chung et al. 2015). Directionality can also arise when the acceptor membrane functions as a sink, so that the transferred lipid partitions more favourably into the acceptor lipid environment than into the donor. In addition, some LTPs exhibit lipid-dependent conformational changes that alter the membrane preference between the empty and lipid-bound state, thereby biasing loading and unloading at distinct membranes (Mesmin et al. 2013). Lipid transfer can also be driven by metabolic trapping in the acceptor compartment, in which conversion of the delivered lipid biases net flux. This is exemplified in yeast, where ER-derived phosphatidylserine (PS) is decarboxylated to phosphatidylethanolamine (PE) in the inner mitochondrial membrane following transfer to mitochondria (Chan and McQuibban 2012). In certain systems, lipid transfer is instead achieved through direct coupling to an ATP-binding cassette (ABC) transporter, such is the case for the bacterial Lpt system (Okuda et al. 2012).

Lipid transfer proteins in disease:

Mutations in LTPs are associated with a variety of diseases and disorders in humans (Paillusson et al. 2016). A well-characterized example involves a host of autosomal recessive mutations found among all four homologs (A-D) of VPS13. Despite their ubiquitous expression across tissues, mutations in these homologs are associated

with distinct neurological disorders. Mutations in *VPS13A-C* often result in a complete loss-of-function and give rise to chorea-acanthocytosis, a progressive movement disorder (*VPS13A*; Ueno et al. 2001), Cohen syndrome (*VPS13B*; Kolehmainen et al. 2003), and early-onset Parkinson's disease (PD) (*VPS13C*; Lesage et al. 2016). This may in part be attributable to differences in their subcellular localization: VPS13A and VPS13C localize to contact sites spanning from the ER to mitochondria, or endolysosomal compartments, respectively. VPS13B has been shown to localize to the interfaces between Golgi compartments, as well as more recently between Golgi-derived vesicles and mitochondria (Kumar et al. 2018; Ugur et al. 2024; Lee et al. 2025). The localization of VPS13D is not yet well-defined, although it has been shown to bind to the ER as well as to mitochondria and peroxisomes via interaction with the Rho-GTPase, Miro, when Miro is over-expressed (Guillén-Samander et al. 2021). Most functional studies on *VPS13*-associated disorders attribute pathology to a loss of tethering functions which affect normal trafficking and morphology. For example, loss of *VPS13C* in human induced pluripotent stem cells (hiPSC)-derived dopaminergic neurons results in an increase in lysosomal size and increased inter-lysosomal tethering which broadly disrupts of their motility and function (Schröder et al. 2024). The extent to which defects in the lipid transfer activity independently contribute to the pathophysiology of *VPS13C*-associated PD is less well established.

Existing Methods to Study Lipid Transport*:*

Because lipid transport is intrinsically coupled to metabolism, which is organelle-specific and dependent on the identity of contacting membranes, no single experimental approach can capture all aspects of this process. As a result, a diverse array of *in vitro* and *in vivo* methodologies has been developed to probe lipid transport with different levels of mechanistic resolution. *In vitro* reconstituted membrane systems have been particularly valuable for dissecting the lipid specificity of LTPs and for crude assessments of the kinetics of transfer (Saheki et al. 2016; Chen et al. 2025). These assays typically involve mixing two synthetic liposome populations, where donor liposomes contain fluorophore-conjugated lipids (often arranged as fluorescence resonance energy transfer (FRET) pairs), and acceptor liposomes serve as lipid sinks. By co-incubation, relative lipid transfer rates can be inferred from changes in fluorescence. Subsequent efforts to better approximate native MCS architecture and composition have adapted these approaches by replacing synthetic liposomes with liposomes generated from homogenized tissue extracts, or even whole organelles where recovery after fractionation is sufficient (Kamerkar et al., 2021). Even with optimization, these reconstitution approaches do not fully capture the complexity of native MCS at the level of protein and lipid composition, nor the regulatory context that further shapes them *in vivo*.

Approaches used to monitor interorganelle lipid transport *in vivo* have mostly relied on the use of radiolabelled lipid precursors or click-chemistry-based pulse-chase experiments. However, the granularity with which transport can be assessed using such assays depends on the lipid's synthesis being confined to a single organelle,

such that its synthesis necessarily implies prior transport. One of the few well-established examples in which this logic has been applied involves monitoring PS transport into mitochondria by following its conversion to PE via decarboxylation by the mitochondrial PS decarboxylase Psd1, in which the appearance of PE serves as a readout of PS flux into mitochondria (Shiao et al., 1995). However, subsequent work in yeast has called the validity of this assay into question. Firstly, a fraction of Psd1 has been shown to localize to the endoplasmic reticulum, raising the possibility that PS decarboxylation can occur without mitochondrial import (Friedman et al. 2018). Second, labelled PE generated by PS decarboxylation may undergo headgroup turnover and be re-incorporated into phosphoethanolamine via the Kennedy pathway, independent of direct inter-organelle transport (Birner et al. 2001). Such limitations motivated the development of METALIC (Mass tagging-Enabled TrAcking of Lipids In Cells) in the Kornmann lab, an *in vivo* approach which enables the analysis of lipid transport between the ER, and in theory, any other organelle, using artificially targeted bacterial lipid-modifying enzymes (Shiino et al. 2021; John Peter et al. 2022). Using this approach, it was found that lipid transport mediated by Vps13-Mcp1 contributes minimally to ER-mitochondria phospholipid exchange, whereas ERMES contributes substantially, consistent with their deletion phenotypes (John Peter et al. 2022). One drawback of METALIC is that lipid transport can only be studied between the ER and other organelles. Additionally, this approach does not inform on the directionality of lipid transport.

Betaine Lipid Transport (BLT)

To overcome the limitations of existing *in vivo* approaches described above, the Kornmann lab is developing a more versatile method capable of studying lipid transport with both spatial and directional specificity: Betaine Lipid Transport (BLT). This method relies on the ectopic synthesis of betaine lipids, non-phosphorous glycerolipids found in bacteria and lower eukaryotic species including some algae and fungi, but absent in *Saccharomyces cerevisiae* and metazoans (Künzler and Eichenberger 1997; Riekhof et al. 2005). It has been shown that growth defects in phosphatidylcholine (PC)-deficient can be rescued by exogenously expressing Bta1 (Betaine Lipid Synthase 1), a single bifunctional enzyme which synthesizes betaine lipids using two lipid-modifying domains: BtaA, a SAM-dependent carboxypropyltransferase, converts diacylglycerol (DAG) into diacylglyceryl-hydroxymethyl-β-homoserine (DGHS), which BtaB, a SAM-dependent N-methyltransferase, then converts into diacylglyceryl-N,N,N-trimethylhomoserine (DGTS) (Riekhof et al. 2014) (Fig. 1A). The fact that DGTS can functionally substitute for PC in *S.cerevisiae* implies that it is distributed across PC-containing organelles, which represents virtually all organelles. Indeed, in some Bta1-expressing species, DGTS is the predominant bilayer-forming lipid, while PC is entirely absent (Riekhof et al. 2005; Hoffmann and Shachar-Hill 2023). This assumption underpins the BLT approach, in which DGTS synthesis serves as a bioorthogonal readout for lipid flux.

As shown in Figures 1A, BLT leverages the stepwise nature of DGTS synthesis: by separating BtaA and BtaB and artificially targeting them to two different organelles,

DGTS synthesis is rendered dependent on DGHS transport. Therefore, DGTS accumulation serves as a readout for the directional lipid transport between these two organelles. Newly synthesized lipids can be traced by pulsing cells with deuterated methionine (2,3,3,4,5-D_5; methyl-D_3), which gets incorporated into S-Adenosylmethionine (SAM), a cofactor required for BtaA and BtaB-mediated synthesis: BtaA transfers a SAM-derived 3-aminocarboxylpropyl group to generate DGHS which introduces a + 5 Da mass shift during pulsing (d5DGHS) (Fig. 1B). Following transport, d5DGHS is converted to d14DGTS by three sequential transfers of SAM-derived methyl groups, introducing a total mass shift of + 14 Da.

Because d14DGTS synthesis requires prior transport of d5DGHS, the relative abundance of d14DGTS reflects the amount of d5DGHS that has been transported over the pulse. Normalizing d14DGTS to the total pool of newly synthesized DGHS species (d5DGHS + d14DGTS) therefore, provides a measure of the rate of lipid transport, which is independent of changes in BtaA and BtaB activity (Fig. 1B).

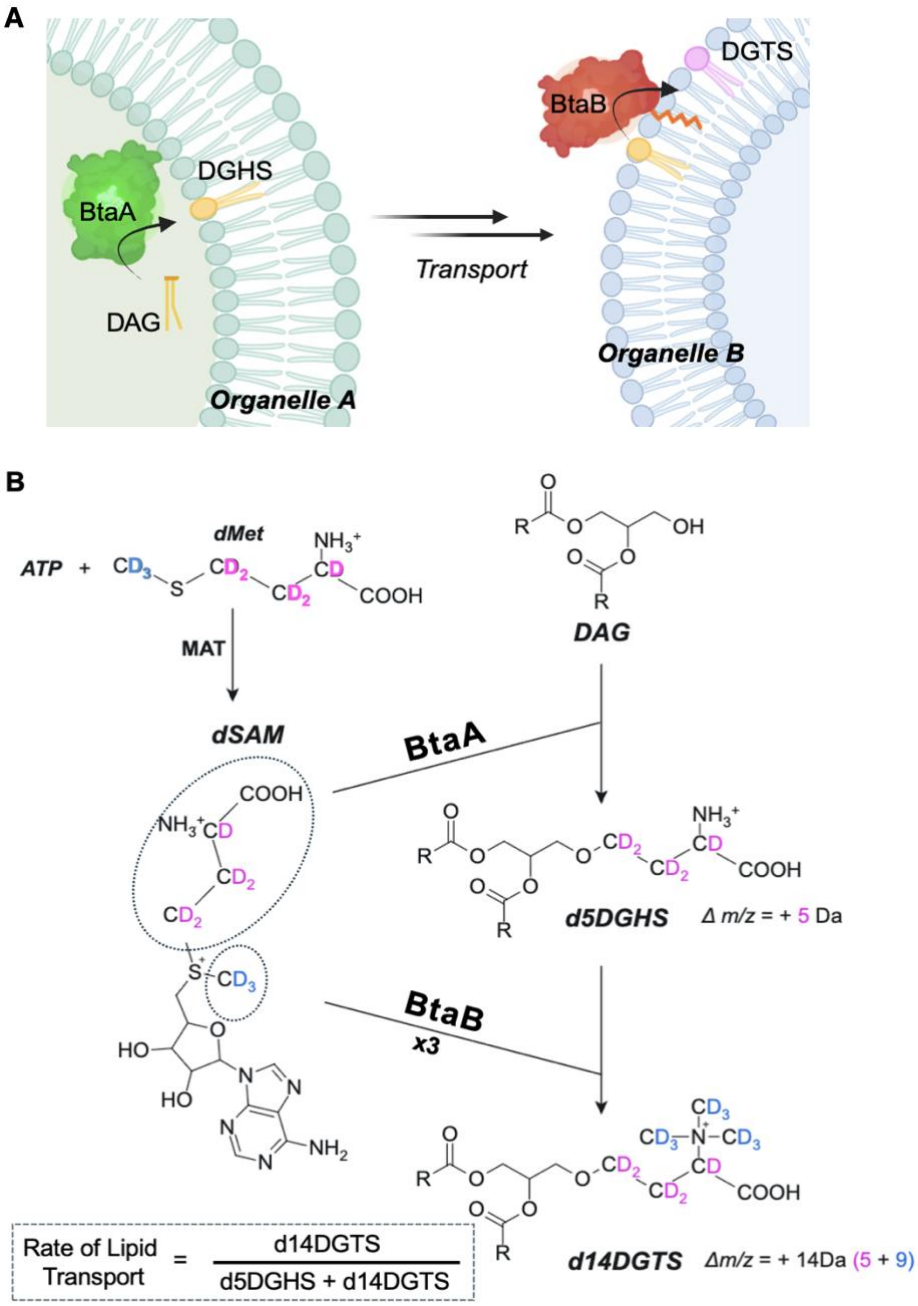

Figure 1. Schematics to demonstrate how mBLT can be used to study inter-organelle lipid transport. (A) BtaA synthesizes DGHS from DAG at organelle A, and following transport of DGHS, BtaB, converts it to DGTS. The identity of organelles A and B, and thus route for lipid transport can be determined by the targeting sequences appended to BtaA and BtaB which can provide lumenal (as in the case of BtaA) or membrane-attached localization. This figure was created on BioRender **(B)** Determining a rate of lipid transport requires selective quantification of newly synthesized DGHS and DGTS (d5DGHS and d14DGTS) generated during pulsing with deuterated methionine (2,3,3,4,5-D_5; methyl-D_3). Accordingly, the mass shift between DGHS and d5DGHS is 5 Daltons (Da). These 5Da are

derived from the deuterium atoms found on the circled 3-amino-3-carboxypropyl moiety of SAM (pink). The mass shift between DGTS and d14DGTS (formed from d5DGHS) is equal to 14 Da, where 9 Da are derived from 3 successive methylation reactions.

The initial development of BLT was carried out in *S.cerevisiae,* an ideal model system for establishing this approach for several reasons. Firstly, *S.cerevisiae* sits in close evolutionary proximity to Bta1-expressing fungal species, minimizing the likelihood of toxicity arising from heterologous expression. Additionally, the characterization of intracellular lipid trafficking and more recent identification of lipid transfer proteins has largely been performed in yeast. Lastly, in comparison to the mammalian lipidome, the yeast lipidome is very well-characterized and relatively simple (Santos and Riezman 2012). This simplicity is particularly advantageous for mass spectrometry-based analyses required for BLT, where accurate resolution of lipid species separated by small mass shifts is required.

Following its initial development, BLT was applied in yeast to investigate the relative contributions of different LTPs, and tethering proteins known to localize at the ER-plasma membrane contact site and thereby assess functional redundancies between components. This was achieved by targeting BtaA to the ER membrane, and BtaB to the plasma membrane and quantifying changes in lipid transport across yeast deletion strains for these different proteins (*Lin, Laurent* et.al, in prep.). The findings of this work showcase the power of BLT as a platform which can be used to shed light on the redundancy of co-operating LTPs and tethers by quantifying directional inter-organelle lipid transport.

Summary

The aim of this study was to establish a proof-of-concept for the application of BLT in mammalian cells, hereafter referred to as mammalian BLT (mBLT). In doing so, I first validated the functionality of the full-length enzyme, Bta1, in HeLa cells by confirming the presence and abundance of DGHS and DGTS relative to endogenous lipids, and the kinetics of their synthesis by metabolic labelling. Notably, the detection of DGHS and DGTS required high-resolution tandem mass spectrometry (MS/MS), because, unlike in yeast, these lipids could not be resolved from endogenous lipids by chromatographic separation and single quadrupole MS. Moving towards studying inter-organelle lipid transport, I next explored approaches to generate the monofunctional enzymes, BtaA and BtaB, where mutagenesis of either domain in the full-length protein proved effective, while truncation of the domains did not. Using these variants, I demonstrated that basal lipid transport could be observed when BtaA and BtaB were co-targeted to the ER or differentially targeted to the mitochondrial matrix and the outer lysosomal membrane.

As described above, a crucial component of mBLT is its ability to report on temporal changes in lipid transport by metabolic labelling, rather than merely basal lipid transport. To establish proof-of-concept for this component, mBLT should be applied under conditions where inter-organelle lipid transport is anticipated to increase or decrease over time. The mitochondrial quality control process, mitophagy, provides such a context. In this configuration, targeting BtaA to the mitochondria and BtaB to the lysosomal membrane is expected to yield a time-dependent (non-linear) increase

in lipid transport owing to increased effective proximity, and ultimate culmination in the mitochondria within the autophagolysosome. Despite performing the experiment, obtaining this proof-of-concept was ultimately limited by low lipid abundance, likely caused by suboptimal enzymatic activity and poor co-transfection efficiency. Nonetheless, the findings presented within this study strongly demonstrate the feasibility of adapting BLT to mammalian cells and delineate key biological and technical constraints that must be further addressed to enable the robust quantification of inter-organelle lipid transport.

Results

Chapter 1: Expression of full-length Bta1 in HeLa Cells

Expression and visualization of Bta1 targeted to the mitochondrial matrix

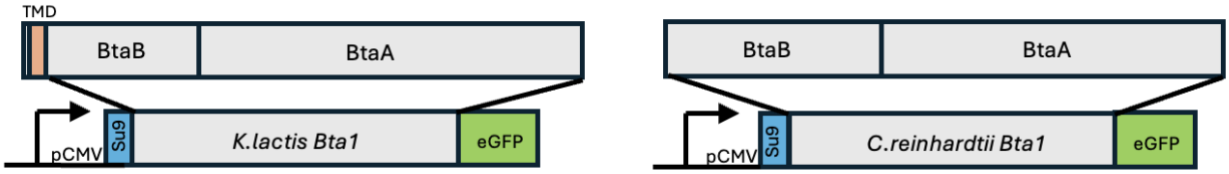

Figure 2. Construct maps for Su9-*Kl*Bta1-eGFP (left), and Su9-*Cr*Bta1-eGFP (right). The sizes of BtaA and BtaB domains are shown to scale with the amino acid residue count.

The goal of this thesis was to adapt the BLT method to mammalian cells to study inter-organelle lipid transport under normal cellular conditions, and ultimately to also approach disease states. For ease of handling and transfection, HeLa cells, an immortalized cell line derived from a human cervical cancer (Scherer et. al., 1953), were used. The first question I addressed was whether Bta1 could be heterologously expressed in HeLa cells. To this end, I generated two full-length Bta1 constructs using sequences from two evolutionarily distant species, *Kluyveromyces lactis* (*Kl*Bta1), and *Chlamydomonas reinhardtii (Cr*Bta1*),* which were validated and used for BLT in yeast. Notably, during the initial development of BLT, a transmembrane domain (TMD) was predicted at the N'terminus of *Kl*Bta1 using hidden Markov models. This TMD was removed to ensure faithful targeting to the mitochondrial matrix afforded by N-terminal fusion to the sequence of ATP synthase subunit 9 (Su9), from *Neurospora crassa* (Vestweber et al., 1988; Fig. 2). Bta1 activity in the

mitochondrial matrix was tested first because matrix localisation afforded by the Su9 presequence is robust. In addition, it is well established that mitochondria actively import the cofactor S-adenosylmethionine (SAM) into the matrix via the SAM carrier protein, SAMC, thus favouring the activity of SAM-dependent Bta1 and enabling downstream assays of lipid transport between mitochondria and other organelles (Agrimi et al. 2004). Codon-optimized sequences for Su9-*Cr*Bta1 and Su9-*Kl*Bta1 were designed for synthesis and subsequently cloned into a pcDNA.5 FRT/TO vector with eGFP at its C' terminus, for visualization.

To assess mitochondrial morphology following transfection in HeLa cells, Su9-eGFP was expressed alone (Fig. 3). As seen in Figure 3, Su9-eGFP-expressing cells exhibited a continuous, reticular mitochondrial network, while expression of Su9-*Kl*Bta1-eGFP or Su9-*Cr*Bta1-eGFP was associated with visibly altered mitochondrial morphology characterized by reduced network connectivity, and circular or ring-like shapes suggestive of mitochondrial stress. This phenotype may be due to the lipid-synthesizing activity of Bta1, or alternatively, the general stress associated with overexpression and mitochondrial import of a large protein. While overexpression of Su9-eGFP allows for visualization of the mitochondrial network, the independent assessment of signal overlap with an endogenous mitochondrial marker such as TOM20 via immunostaining would provide a more direct evaluation of mitochondrial morphology.

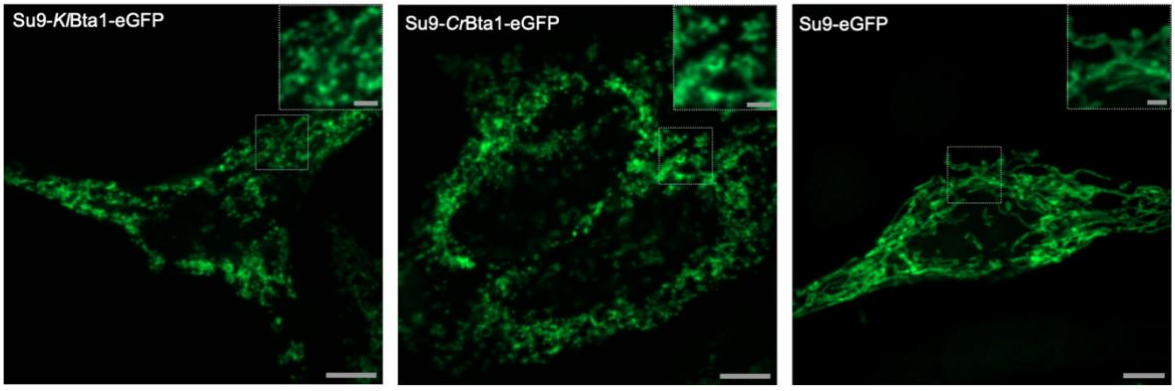

Figure 3. Expression of mitochondrially targeted Bta1-eGFP fusion proteins in HeLa cells. From left to right, representative images of HeLa cells expressing Su9-*Kl*Bta1-eGFP (left), Su9-*Cr*Bta1-eGFP (middle) or simply Su9-GFP (right) are shown. Scale bar(s) = 10 µm (bottom right), 5 µm (inset).

Assessment of the activity of transiently expressed Bta1 targeted to the mitochondrial matrix in HeLa cells by LC–MS

After confirming faithful localisation of the above constructs to the mitochondrion, I next sought to assess the lipid-synthesizing activity of Bta1 using hydrophilic interaction liquid chromatography (HILIC) coupled to a single-quadrupole mass spectrometer (LC-MS) which operates at unit-mass resolution. Mass spectra were acquired in selected ion monitoring (SIM) mode using positive electrospray ionization (ESI^+). In SIM mode, the quadrupole mass analyzer selectively transmits predefined *m/z* values within specified retention-time windows, thereby improving sensitivity of DGTS and DGHS detection relative to full-scan acquisition. Positive ESI was employed because DGHS readily forms a singly protonated ion via its amine group, whereas DGTS carries a permanent positive charge on the quaternary ammonium found on the trimethylhomoserine headgroup.

To benchmark the expected lipid signals, I first consulted unpublished experiments performed in yeast by Ying-Chen Lin, a postdoctoral fellow in the Kornmann lab, and my supervisor at the outset of this project. In yeast, DGHS and DGTS signals were identified by comparing extracted ion chromatograms (EICs), generated by integrating signal intensity over time for *m/z* values corresponding to expected DGHS and DGTS species. Assignment of these signals was further supported by analysis of samples expressing the enzymatic components of Bta1, BtaA and BtaB, either individually or in combination. Under this logic, DGHS synthesis requires expression of BtaA alone, whereas DGTS synthesis requires co-expression of both BtaA and BtaB, and neither lipid should be detected upon expression of BtaB alone. The strategy of independently expressing BtaA and BtaB is described in detail in Chapter 2.

As shown in Figure 4, co-expression of ER-targeted BtaA and mitochondrially targeted BtaB in yeast resulted in the appearance of peaks corresponding to 32:1, 32:2, 34:1, and 34:2 DGHS and DGTS. Crucially, these peaks are absent in the extracted ion chromatograms (EICs) from the control sample, where fluorescent constructs targeted to the ER and mitochondria, without BtaA or B, were co-expressed. These data were used for qualitative comparisons to the experiments I performed, described below.

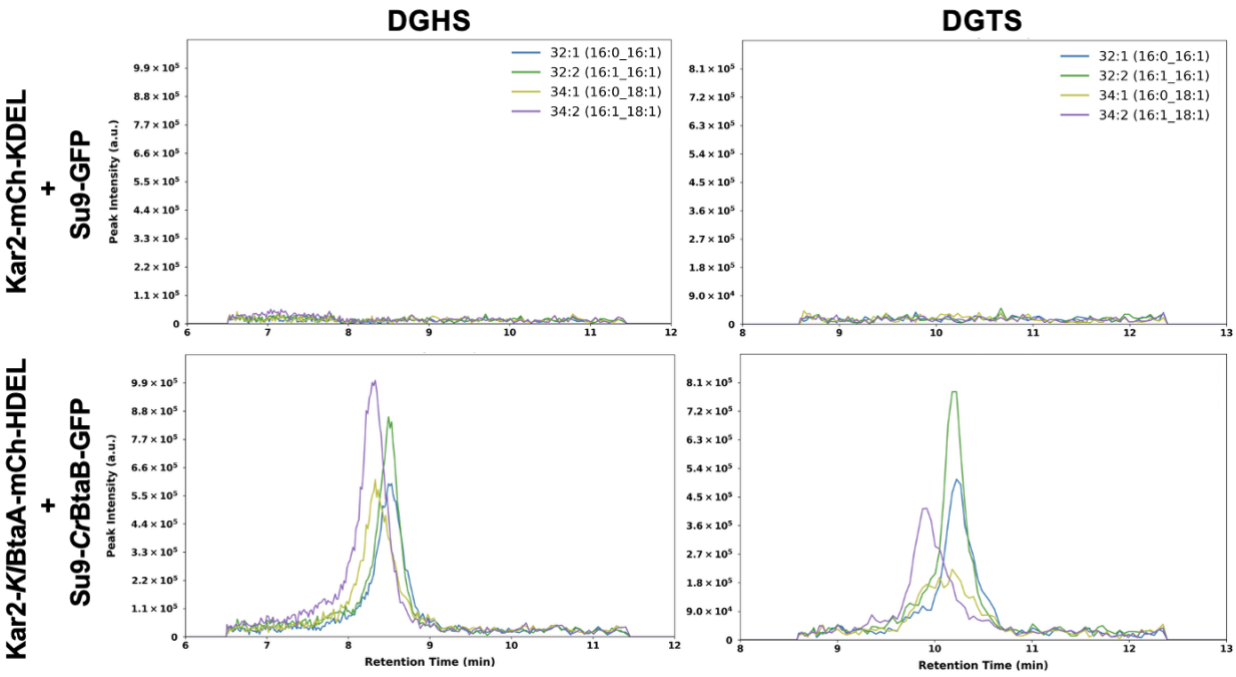

Figure 4. Detection of $[DGHS+H]^+$ and $[DGTS+H]^+$ by SIM HPLC-MS in yeast co-expressing Kar2-KlBtaA-mCh-HDEL and Su9-CrBtaB-GFP. Shown are representative overlays of EICs for DGHS (left) and DGTS (right) species found in yeast expressing both ER-targeted BtaA and mitochondrially targeted BtaB (lower panels) or control constructs (upper panels) that are targeted to the ER and mitochondria, but do not contain BtaA or B. The different molecular species are indicated in different colors. Chromatograms were generated with a mass extraction window of ± 0.5 m/z, reflecting the unit-mass resolution (FWHM ~0.7 Da) of the single quadrupole, which discriminates ions only at the nominal-mass level.

In the following LC-MS experiments conducted in HeLa cells, I used *K.lactis* Bta1 (*Kl*Bta1) depicted above (Fig. 2) because of the evolutionary proximity of *K.lactis* (yeast)-humans, compared to the *C. reinhardtii* (alga)-human distance. For comparison, lipid extracts from Su9-eGFP-alone expressing cells were used as a negative control. In HeLa cells, peaks corresponding to DGHS and DGTS precursor ions were observed in samples expressing Su9-*Kl*Bta1-eGFP (Fig. 5). However, these same peaks were also observed in samples overexpressing Su9-eGFP and were of comparable intensity. These peaks therefore may correspond to

endogenous lipids which exhibit similar chromatographic behaviour and are isobaric at unit-mass resolution to DGTS and DGHS. Given that HILIC separates lipids based on headgroup polarity, the “contaminating” peaks observed in said samples may correspond to endogenous lipids with similarly zwitterionic headgroups, such as PC, or sphingomyelin (SM). Moreover, the comparable signal intensities for DGTS and DGHS between samples indicate that any potential Bta1-dependent signal lies at or below the effective detection limit, the lowest signal that can be distinguished from the background. Taken together, these data were insufficient to establish that Bta1 is functional when overexpressed in HeLa cells.

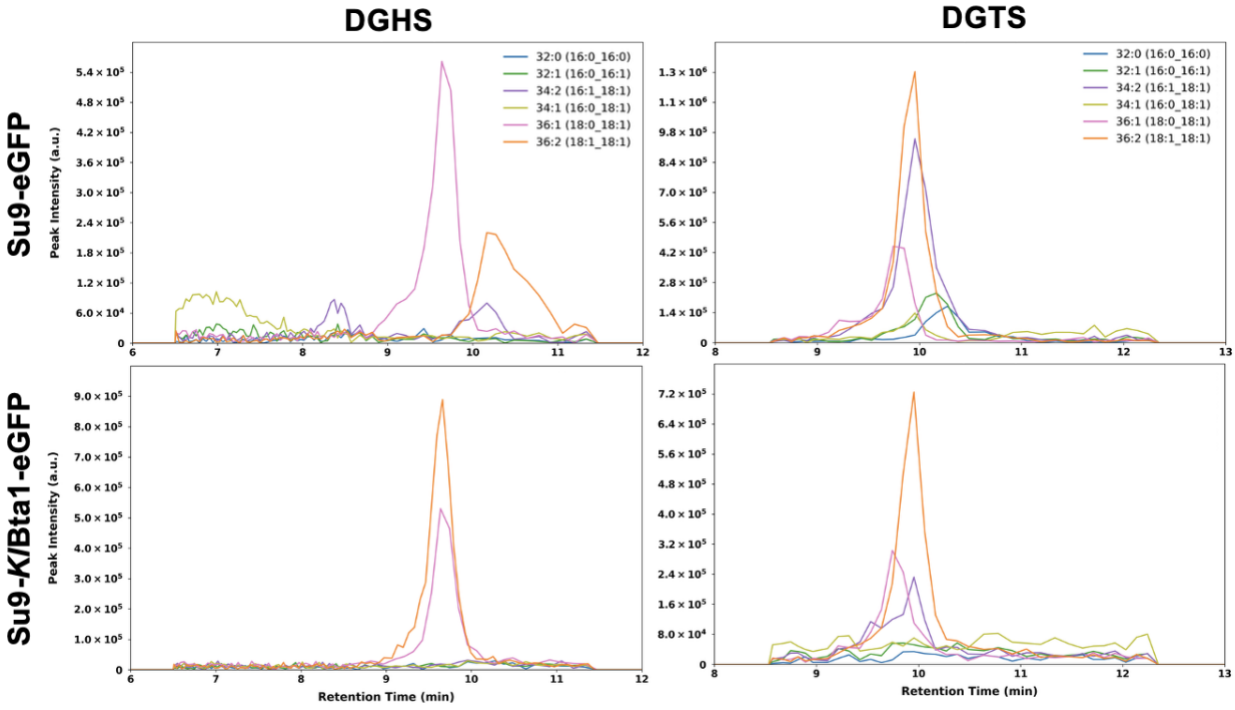

Figure 5. Detection of [DGHS+H]⁺ and [DGTS+H]⁺ by SIM HPLC-MS in HeLa cells expressing either Su9-eGFP or Su9-*K*/Bta1-eGFP. Shown are representative overlays of EICs for DGHS (left) and DGTS (right) species in HeLa expressing Su9-eGFP alone (top panel), or mitochondrially targeted Bta1 (bottom). Chromatograms were generated with a mass extraction window of ±0.5 m/z, reflecting the unit-mass resolution (FWHM ~0.7 Da) of the single quadrupole, which discriminates ions only at the nominal-mass level.

Under the working (and optimistic) assumption that Bta1 was functional when expressed, I addressed the challenge of detecting DGHS and DGTS among co-eluting isobars by performing chromatographic isolation before lipidomic analyses. As an initial strategy, one-dimensional thin-layer chromatography (TLC) was performed on whole-cell lipid extracts from Su9-*K*lBta1-eGFP-expressing HeLa cells (Fig. 6). To enable localisation of the DGTS migration region, extracts were spiked with an excess of a deuterated DGTS standard (N,N,N-trimethyl(d9)-DGTS) (d9DGTS). The TLC solvent system enabled broad separation of lipid classes, allowing the general DGTS migration region to be identified by location of the standard, as ectopically synthesized DGTS was otherwise not detectable under the staining conditions used. DGHS could not be independently localised by TLC, because a lipid standard was not available at the time of this experiment and had to be custom-synthesized by an external supplier. Following analysis by TLC, the silica in the lipid standard's migration region were scraped and re-extracted with the aim of recovering endogenously synthesized DGTS for SIM LC-MS analysis. However, no peaks corresponding to DGTS beyond that of the standard were identifiable (data not shown). While this result was consistent with the absence of Bta1-dependent DGTS production, inefficient lipid recovery from the silica, or ion suppression by the d9DGTS standard may have also limited detection. In retrospect, mitochondrial fractionation could also have been explored as a method to increase the relative abundance of DGTS and DGHS in lipid extracts by enriching for the subcellular compartment to which Bta1 was targeted.

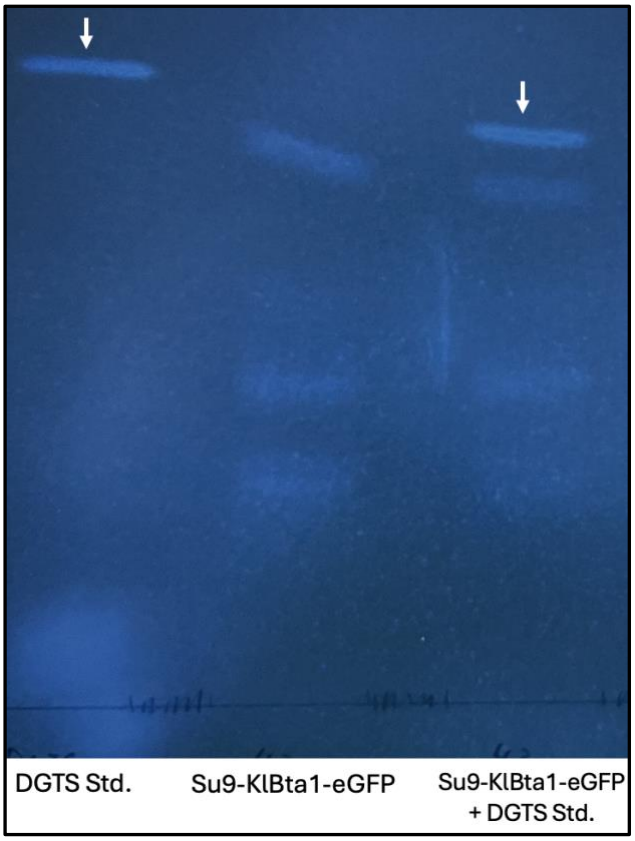

Figure 6. One-dimensional TLC plate with primuline-resolved lipid bands derived from spotting 5ug of the N,N,N-trimethyl(d9)-DGTS standard (first lane), whole-cell lipid extracts derived from Su9-*Kl*Bta1-eGFP-expressing cells (second lane), and whole-cell lipid extracts derived from Su9-*Kl*Bta1-eGFP-expressing cells spiked with 5ug of a commercially available d9DGTS standard (third lane) visualized under 365 nm UV light. Bands corresponding to the region of the d9DGTS standard are marked with a white arrow. *The slanting between lanes is caused by an uneven solvent front.

In addition, to increase and thereby resolve DGHS and DGTS signals I restricted my analysis to successfully transfected cells, by performing fluorescence-activated cell sorting (FACS) gating for GFP-positive (Bta1-expressing) cells prior to lipid extraction and SIM LC-MS analysis. Here, the aim was to increase the relative abundance of DGTS and DGHS amongst endogenous isobars and thereby improve signal-to-background. I successfully sorted a population of fluorescent cells that

comprised ~8% of the total population. Despite this enrichment, signals for DGTS and DGHS could still not be confidently assigned by SIM LC-MS (data not shown).

Assessment of the activity of stably expressed Bta1 targeted to the mitochondrial matrix in HeLa cells by SIM LC–MS.

Because, as noted above, only a fraction (~8 %) of the cell population expressed Su9-*KI*Bta1-eGFP, the possibility that suboptimal transfection and thus, expression across the population contributed to the absence of DGHS and DGTS signal in bulk lipid extracts was considered. To ensure expression across the entire population of cells, and hence increase DGTS and DGHS abundance, I generated a doxycycline-inducible cell line expressing Su9-*KI*Bta1-eGFP. This was accomplished by co-transfecting tetracycline-regulated expression (TREx) HeLa cells with the Su9-*KI*Bta1-eGFP containing FRT/TO plasmid and pOG44, a Flp-recombinase-expressing plasmid, to mediate stable genomic integration of this construct FLP/FRT recombination (Fig 7A). Following hygromycin selection, two clonal populations were expanded, maintained, and verified for expression by confocal microscopy following treatment with doxycycline (0.5 µg/mL, 24 h) (Fig. 7B). Despite successful induction and uniform expression of Su9-*KI*Bta1-eGFP, subsequent lipidomic analyses using SIM LC–MS did not allow for confident detection of DGTS or DGHS relative to non-induced control samples (Fig. 8).

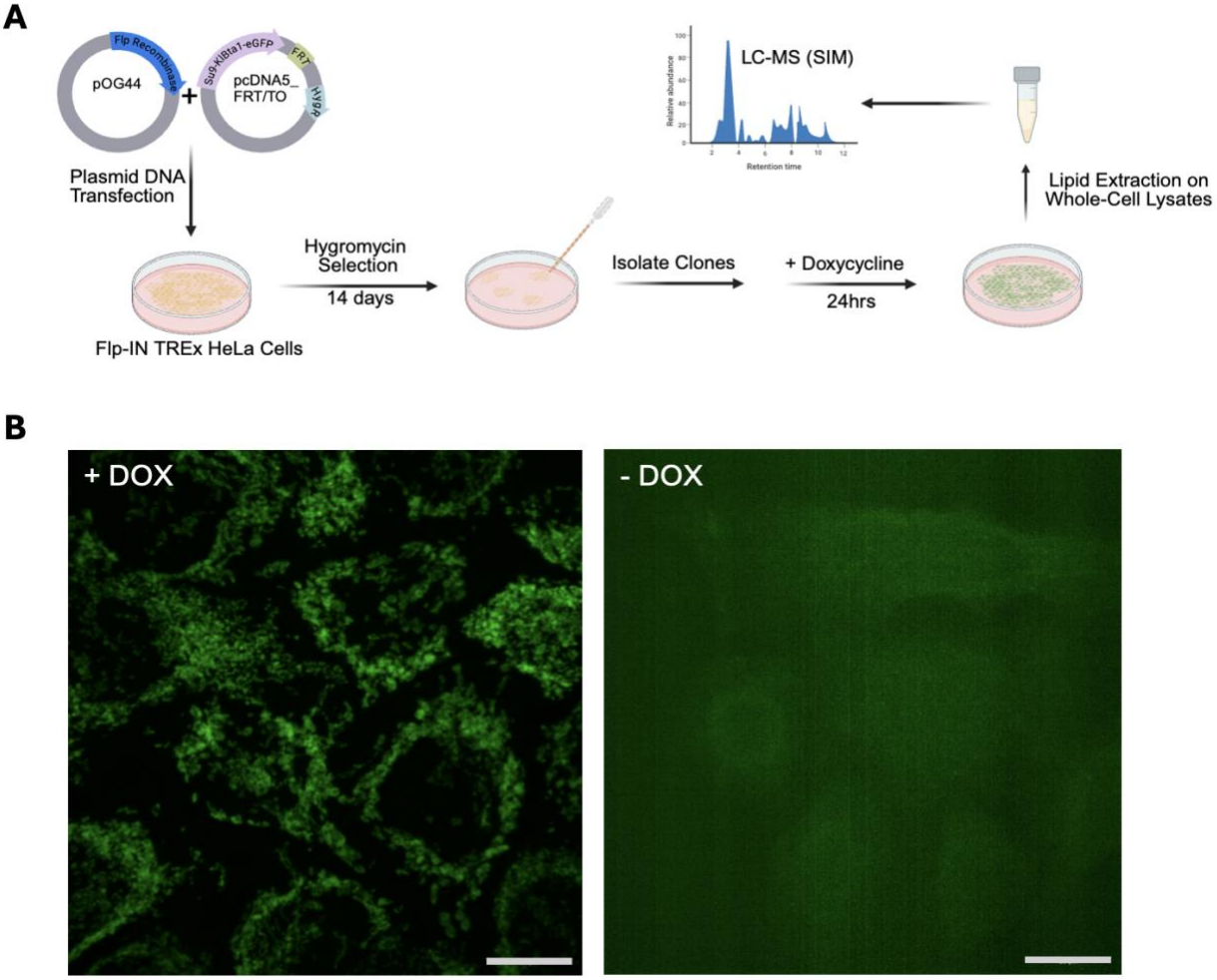

Figure 7. Generation of a cell line stably expressing mitochondrially targeted Bta1. **(A)** Schematic of stable cell-line generation using the Flp-In™ T-REx™ system. Following hygromycin selection, two monoclonal cell populations were isolated, expanded, and maintained. Expression was induced by addition of doxycycline (0.5 µg/mL) for 24 h prior to cell harvesting, lipid extraction, and LC–MS analysis. **(B)** Representative confocal images of a single monoclonal population expressing Su9-*Kl*Bta1-eGFP, showing apparent mitochondrial localisation. Scale bar = 10 µm.

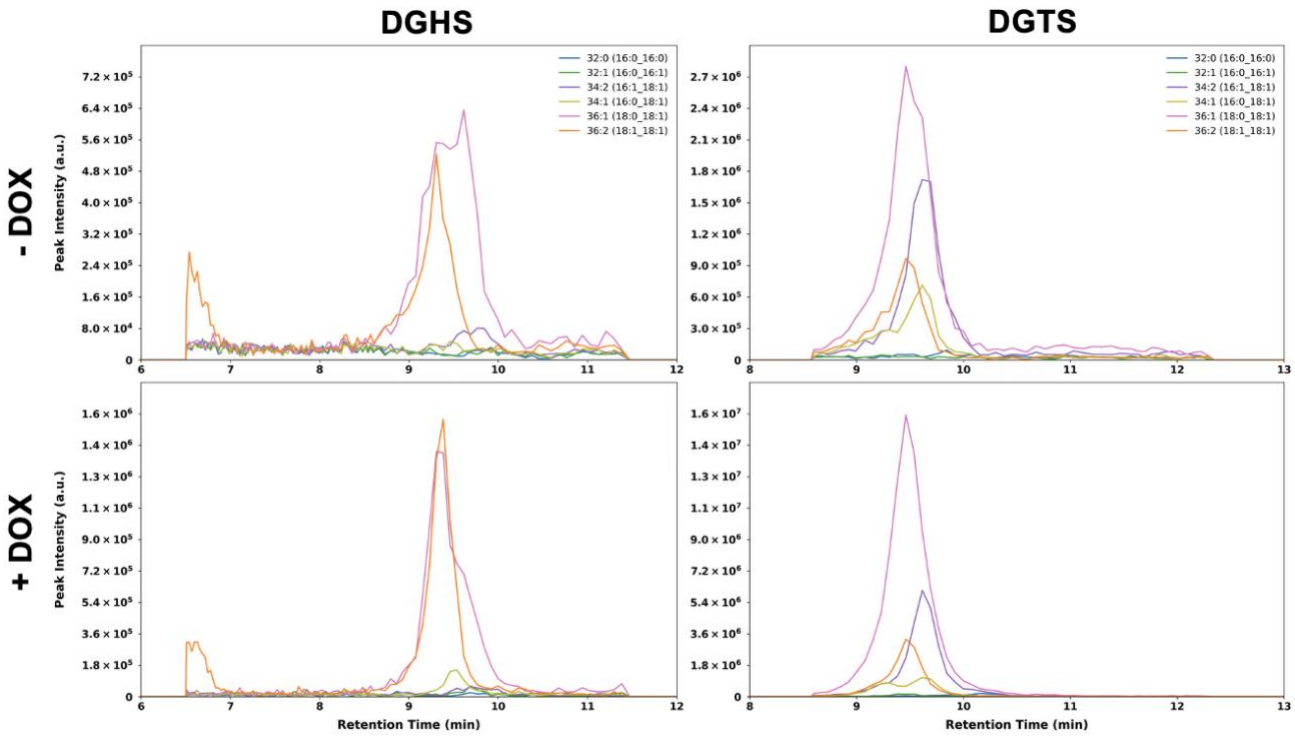

Figure 8. Detection of $[DGHS+H]^+$ and $[DGTS+H]^+$ in Su9-*K*/Bta1-eGFP-expressing HeLa cell line by SIM HPLC-MS. Shown are representative overlays of the EIC for DGHS (left) and DGTS (right) in HeLa cells to express a mitochondrially-targeted Bta1 upon induction with doxycycline (DOX). Peaks corresponding to DGHS and DGTS species were detected in non-induced (-DOX) (upper panels) and induced (+DOX) (lower panels) conditions. The different molecular species are indicated in different colors. Chromatograms were generated with a mass extraction window of ±0.5 m/z, reflecting the unit-mass resolution (FWHM ~0.7 Da) of the single quadrupole, which discriminates ions only at the nominal-mass level.

Determining the fragmentation patterns for DGTS and DGHS by ESI^+ and ESI^- Direct Infusion MS/MS

To access a mass spectrometer of sufficient sensitivity to detect the elusive DGTS and DGHS in HeLa cells, I initiated and established a collaboration with postdoctoral fellow, Carla Kirschbaum, and postgraduate student, Jack Bennett, from Dame Prof. Dr. Carol Robinson's lab. As such, I was afforded the opportunity to run lipidomics on the Orbitrap Eclipse, a high-resolution mass spectrometer which is capable of discriminating lipid precursors with < 0.001 m/z differences and performing tandem mass spectrometry (MS/MS). Crucially, tandem mass spectrometry allows for isobaric lipid signals to be resolved. This is because the resulting MS/MS or fragmentation spectra inform on lipid structure, rather than precursor mass alone. Following the identification of diagnostic fragment ions which uniquely report on a given lipid class, these fragments can be incorporated into a reference spectral library. This reference library is then matched to sample-derived MS/MS spectra *post-hoc* which enables unambiguous assignment of corresponding MS^1 signals, and subsequent quantification.

Accordingly, before running lipidomics on bulk lipid extracts derived from Bta1-expressing cells to assess the enzyme's functionality in HeLa cells, I first determined the fragmentation patterns for DGTS and DGHS by running direct infusion or shotgun MS/MS, wherein lipid standards for either lipid were directly injected into the ion source of the mass spectrometer. Ionization was performed in positive mode for the same reasons as mentioned above. The chemical structures for each lipid

precursor are drawn out in Figure 9, where the orientation of each fragmentation bracket indicates which side of the molecule retains the charge and is therefore detected, while the complementary portions are lost as neutral species. As shown in Figure 9, DGTS fragments to yield fragments which correspond to the headgroup alone (labelled with a blue spot), or together with the glycerol backbone (labelled with two magenta dots) as well as acyl-chain-containing fragments (labelled with a single magenta or green spot) that are useful for reporting on the acyl-chain composition. The headgroup-containing fragments at 236.15 m/z is diagnostic of DGTS, i.e. no other lipid class will show this fragment, unlike for instance the peak at 162.11 m/z which is also characteristic of PC or SM.

To our surprise, in the gas-phase, protonated DGHS undergoes a nucleophilic addition reaction for which a putative mechanism was derived (Supplementary Figure 1). This putative reaction yields two rearranged products, one of which is not neutral and therefore not detected, while the other which gives rise to an additional fragment at 340.28 m/z, which is the most abundant fragment ion observed. This fragment (yellow star, Fig. 9B) is diagnostic of DGHS, and therefore worth including in the DGHS reference library. However, because this fragment retains an intact acyl-chain, it is inherently acyl-chain-specific. Entries within reference libraries on LipiDex can be class-specific or acyl-specific (Hutchins et al., 2018). In the case of the former, fragments can be resolved by their molecular formula or their exact mass. Acyl-specific fragments, otherwise known as alkyl neutral losses, are typically defined by the mass difference between the full acyl-chain and the fragment

consistent with the loss of water (magenta spot) or hydrogen (green spot). This allows for any acyl-chain to be calculated parametrically. The star-denoted fragment, however, fits into neither of these categories as it is both class and acyl-chain specific. This fragment was therefore not included in the DGHS spectral library, with the additional assumption that the remaining fragments would be sufficient for positive spectral annotation.

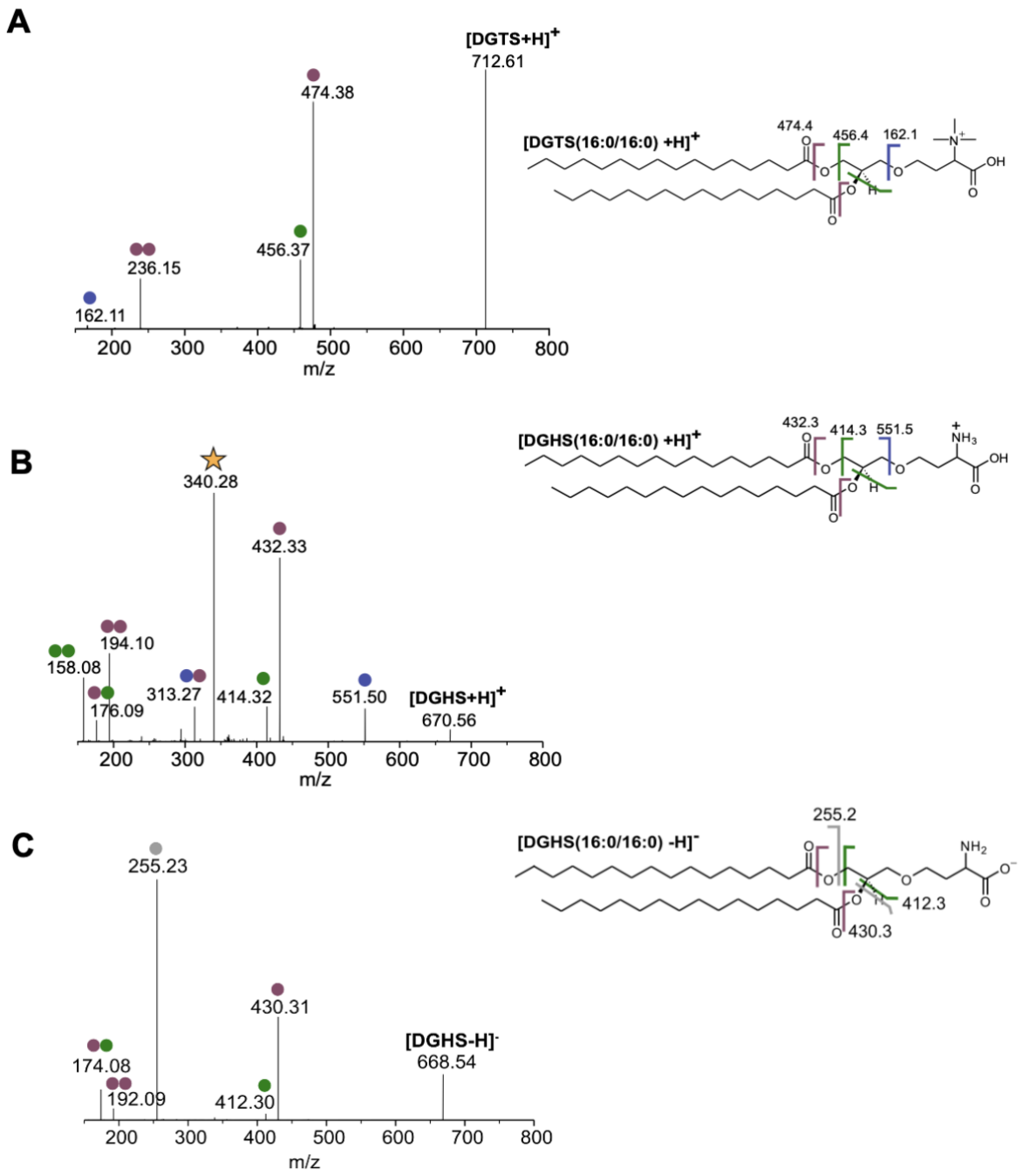

Figure 9. Representative LC-MS/MS spectra for 32:0 [DGTS+H]$^+$, 32:0 [DGHS+H]$^+$, and 32:0 [DGHS-H]- . Spectra for the precursor ions (**A**) 712.61 m/z corresponding to 32:0 [DGTS+H]$^+$, (**B**) 670.56 m/z corresponding to 32:0 [DGHS+H]$^+$, and (**C**) 668.54 m/z corresponding to 32:0 [DGHS - H]$^-$. The y-axis indicates ion abundance relative to the most abundant peak. The m/z values are listed to 2 decimal places (dp) for visibility, but were acquired at 4 dp, with the Orbitrap Eclipse (resolving power 120,000 FWHM at m/z 200) supporting precision to the third decimal place (< 3 ppm mass accuracy). Chemical structures indicate the observed bond cleavages, with cleavage brackets denoting fragmentation sites and bracket orientation indicating the charged portion of the molecule

that is detected. Colored markers denote fragment classes as defined in the main text: headgroup fragments (blue), headgroup with glycerol backbone (magenta), acyl-chain–containing (green), acyl-chain anions observed only in negative-ion mode (grey), and a fragment derived from rearrangement reaction of $[DGHS+H]^+$ (yellow star) (see Supplementary Fig.1).

Confirmation of the activity Bta1 targeted to the mitochondrial matrix when transiently or stably expressed in HeLa cells by RSLC-MS/MS

To assess the activity of mitochondrially targeted Bta1 expressed in HeLa cells I ran lipidomics using data-dependent acquisition (DDA) LC-MS/MS, in ESI^+ mode. DDA was selected for acquisition because it allows for broad lipid discovery and generates high-quality MS/MS spectra suitable for annotation. In DDA LC-MS/MS, precursor selection for MS/MS is driven by an MS^1 intensity threshold, such that MS/MS sampling is biased towards abundant lipids. This became a limitation as the project progressed and is addressed in Chapter 2. Nonetheless, to my pleasant surprise, multiple DGHS and DGTS species were detected in samples derived from cells transiently expressing Su9-*Kl*Bta1-eGFP or Su9-*Cr*Bta1-eGFP by running lipidomics using DDA LC-MS/MS. Notably, the detection of DGHS suggests that DGHS can dissociate from the Bta1 after its synthesis, and therefore that catalysis by BtaA and BtaB domains in the full-length enzyme are not obligately sequential. This observation is consistent with the ancestral architecture of Bta1 in prokaryotes, where DGHS and DGTS synthesis are performed by two distinct soluble enzymes. The inclusion of EICs from a negative control are not necessary here, as the specificity afforded by MS/MS is sufficient to confirm lipid identity

The extracted ion chromatograms (EICs) shown in Figures 10 represent those of 34:1 (16:0_18:1) DGTS and DGHS, the most abundant molecular species observed for both lipids, in both samples. The blue integrated area corresponds to the MS^1 feature detected following processing performed on MS-DIAL (version 4) software, which detects features based on MS^1 derived precursor mass and MS/MS spectral similarity to the reference libraries (see Methods). Images from the MS-DIAL user interface are shown to illustrate the EICs for these features, as unlike the discrete, scan-by-scan raw MS^1 EICs, these have been smoothened, and additionally clearly show the peak boundaries. The EICs for 34:1 DGHS show additional un-highlighted flanking peaks, indicating the presence of co-eluting, isobaric lipid species within the ± 0.01 *m/z* extraction window. This demonstrates that, even when using high-resolution mass spectrometry, MS-derived accurate masses alone are insufficient to uniquely assign DGHS under these experimental conditions. Tandem mass spectrometry is therefore required to distinguish true DGHS signals from the endogenous mammalian lipid background. This also helps illustrate why SIM LC-MS was insufficient.

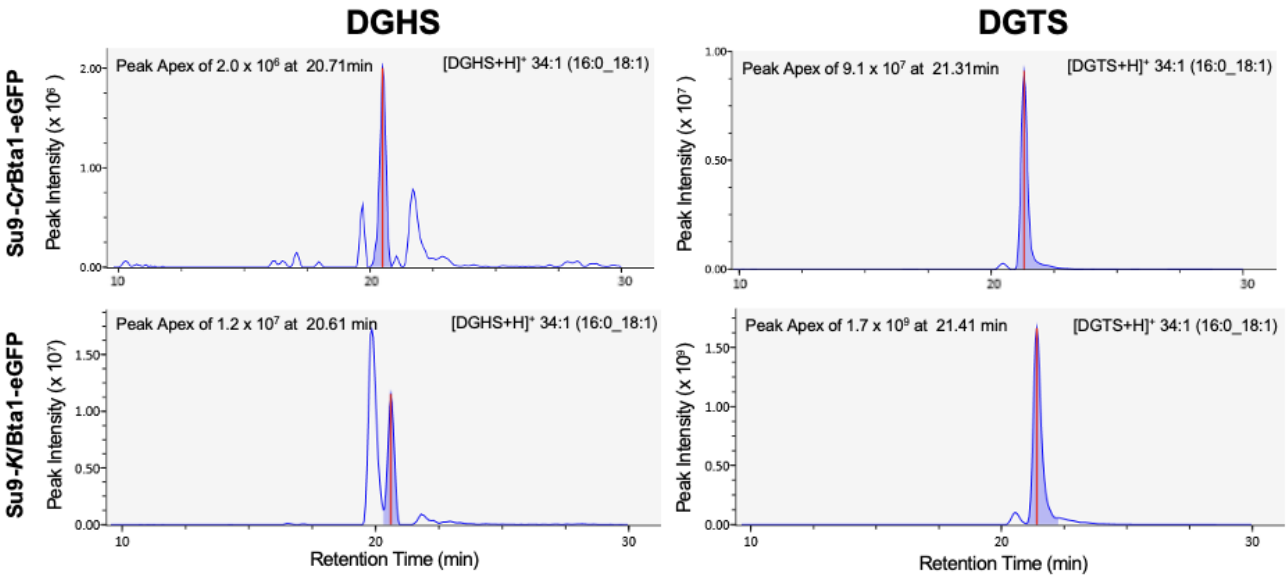

Figure 10. Extracted ion chromatograms for 34:1 (16:0_18:1) [DGHS+H]⁺ (left) and 34:1 (16:0_18:1) [DGTS+H]⁺ (right) observed in Su9-*Cr*Bta1-eGFP-expressing HeLa cells (top) and Su9-*Kl*Bta1-eGFP-expressing HeLa cells (bottom). The blue highlighted area corresponds to the signal of the annotated lipid after MS/MS spectral matching and peak detection performed on MS-DIAL[4] software.

Profiling DGHS and DGTS abundances relative to endogenous lipids

To roughly quantify the semi-absolute amount of DGTS and DGHS within the HeLa cell lipidome, I profiled a subset of endogenous lipids alongside DGTS and DGHS in cells which transiently expressed Su9-*Kl*Bta1-eGFP (Fig. 11A). To do so, lipid extracts were analysed by DDA LC-MS/MS using both positive- and negative-mode ESI to maximize coverage across lipid classes: positive-mode ESI was used to profile PC, PE, DAG, DGTS, and DGHS, while negative-mode ESI was used to profile PI and phosphatidylglycerol (PG). Intuitively, it would have been better to profile the absolute amount of DGTS and DGHS in bulk lipid extracts from cells which stably express Bta1, as this would reflect their true per-cell abundance. To correct for this systematic underestimation, I calculated the percentage of cells which were

positively transfected by fluorescence microscopy prior to RSLC-MS/MS (Fig. 11B). Approximately 45% of cells were GFP-positive (n = 3096 cells). As DGTS amounted to ~ 1% of the total lipid content within the total cell population, I conclude that DGTS likely represents closer to ~ 2% and DGHS, ~ 1% of the total lipid content among transfected cells. As expected, PC and PE represent the most abundant species, while PI, PG, and SM represent minor species. In retrospect, it would have been preferable to measure the amounts of these same lipids in un-transfected cells, to determine if any native lipids change significantly in abundance upon Bta1 expression.

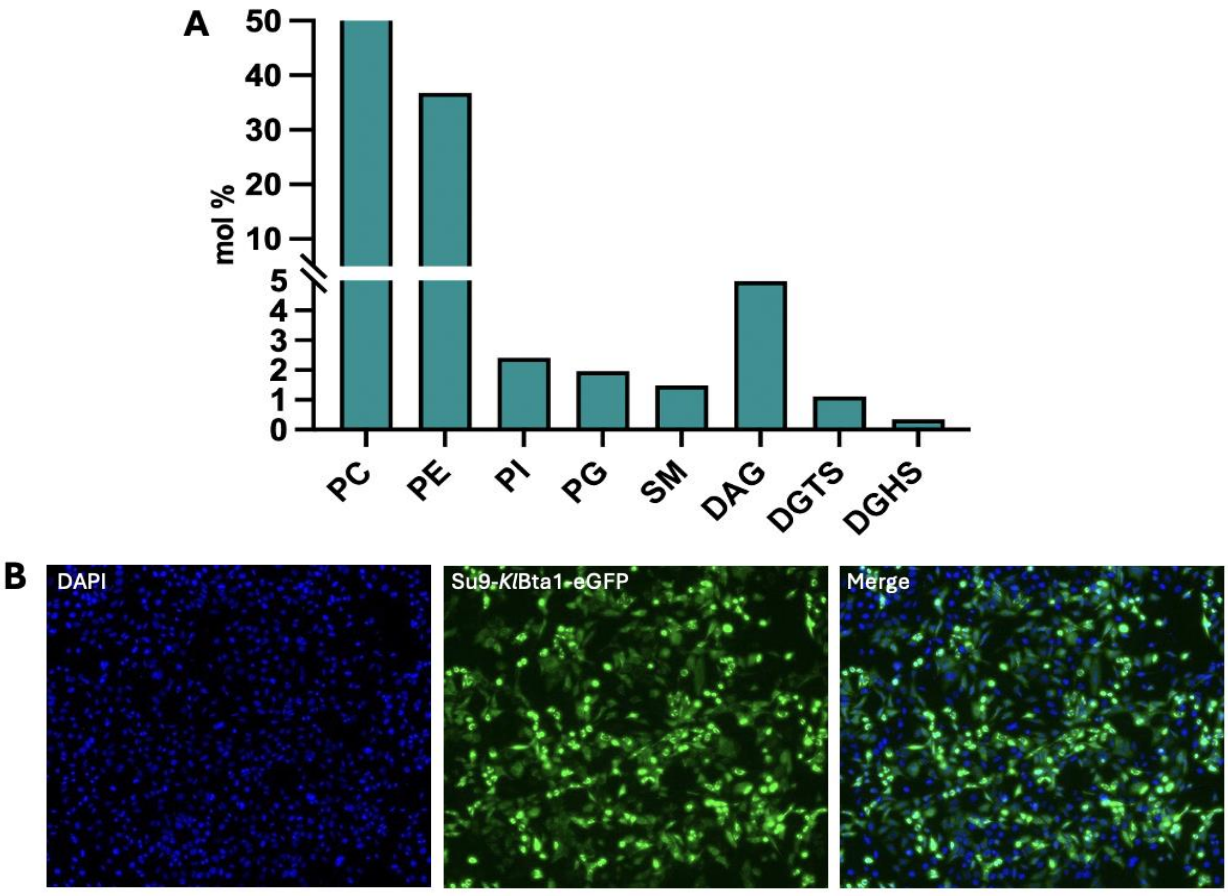

Figure 11. Profiling endogenous lipids, PC, PE, PI, PG, SM, DAG, DGTS, and DGHS in HeLa cells transiently expressing Su9-*Kl*Bta1-eGFP. (**A**) Relative molar percentage for each lipid where for endogenous lipids, raw peak areas were normalized to class-matched

internal standards found in SPLASH Lipidomix, and for DGTS and DGHS, to commercially available or custom-synthesized standards. (**B**) Representative fluorescent image of HeLa cells 24 hours after transfection with Su9-*Kl*Bta1-eGFP with nuclei visualized using a DAPI counterstain, acquired on the Echo Revolve microscope at 10x magnification.

In addition, I profiled the relative abundance of individual DAG and DGTS molecular species to assess whether DGHS and DGTS composition reflects the bulk cellular DAG pool (Fig. 12). This analysis was performed in cells expressing either Su9-*Kl*Bta1-eGFP or Su9-*Cr*Bta1-eGFP to evaluate potential species-dependent differences in substrate utilization. Only two DGHS species were detected (32:1 and 34:1), where the MS^1 signals for other DGHS species likely lay below the effective detection limit. This result is consistent with 32:1 and 34:1 DGTS being the most abundant molecular species, accounting for over 50 % of total DGTS in Su9-*Cr*BTA1-eGFP-expressing cells and over 70 % in Su9-*Kl*Bta1-eGFP-expressing cells. Overall, the molecular composition distribution of DGTS broadly parallels that of the bulk cellular DAG pool. However, this analysis relies on whole-cell DAG measurements, whereas DGTS synthesis is localised to mitochondria. It is therefore potentially naïve, though still informative, to equate bulk DAG composition with the mitochondrial DAG pool accessed by Bta1. More generally, DGTS displays a broad molecular diversity encompassing both monounsaturated and polyunsaturated species. Interpretation of enrichment or depletion of specific DGTS species is further complicated by a limited understanding of *de novo* mitochondrial DAG synthesis and/or import.

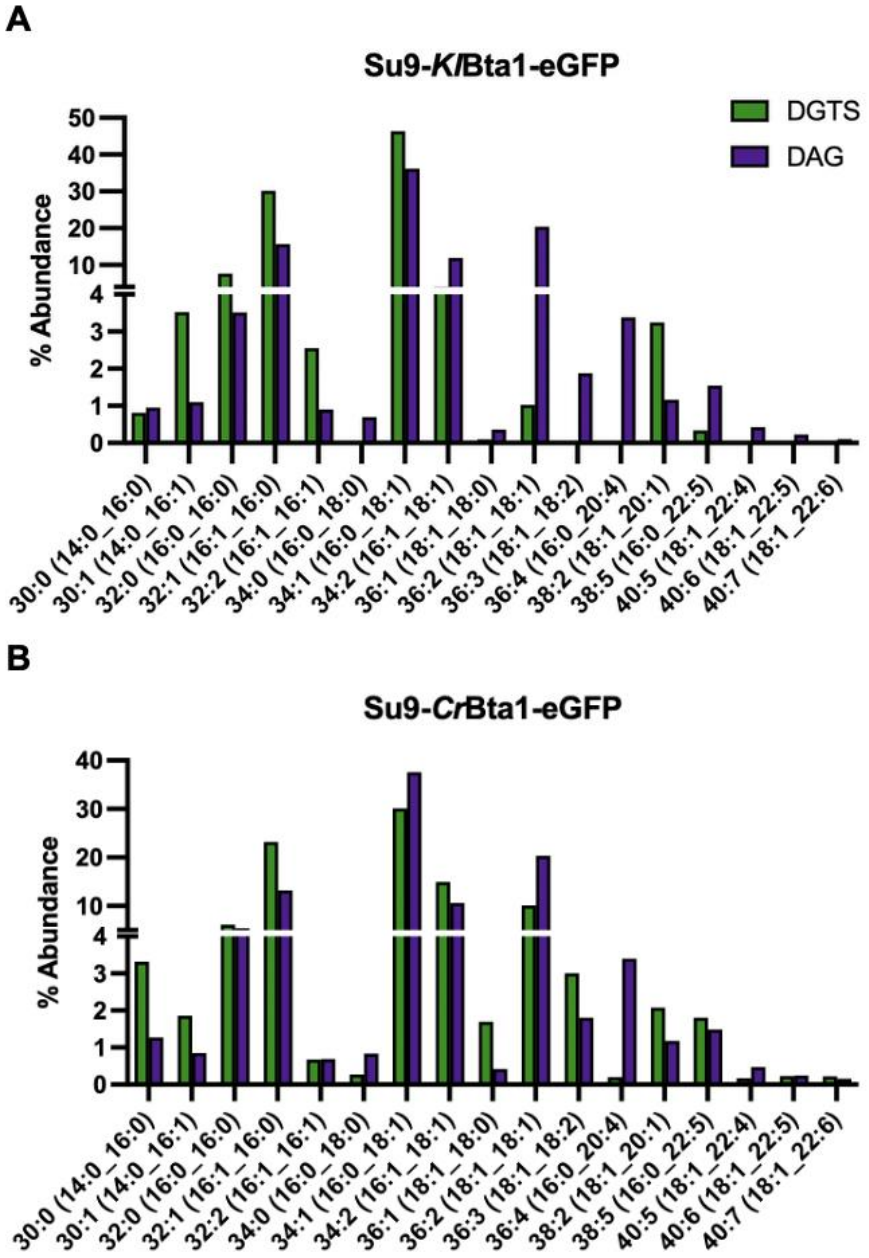

Figure 12. Profiling the molecular composition of bulk cellular DAG and DGTS in HeLa cells expressing Su9-*Kl*BTA1-eGFP Su9-*Cr*BTA1-eGFP. (**A**) Relative abundance of DGTS (green) and DAG (purple) species in Su9-*Kl*BTA1-eGFP and (**B**) Su9-*Cr*BTA1-eGFP-expressing cells, exhaustive of all detected molecular species for DGTS. Percentage abundances were calculated by dividing individual peak areas by the sum of all peak areas. Molecular species are ordered by increasing acyl-chain length from left to right.

Kinetic analysis of DGHS and DGTS synthesis by Bta1

To assess the kinetics of DGHS and DGTS synthesis by Bta1, cells expressing Su9-*Kl*Bta1-eGFP were subjected to a pulse-labelling experiment using deuterated methionine (dMet). Cells were initially cultured in standard growth medium containing unlabelled methionine. At time zero, the culture medium was completely replaced with methionine-free medium supplemented with dMet at the same concentration as unlabelled methionine in the original medium. Cells from independent experiments were then harvested 0, 30, 60, 120, or 240 min after the media change. In pulse-labelling experiments done in yeast strains co-expressing BtaA and BtaB, labelled DGHS and DGTS first appear 1-2 hours following pulse initiation. The harvesting time points were selected to linearly bracket this window, allowing sufficient time for label incorporation.

Metabolic labelling with deuterated methionine revealed distinct kinetic behaviours for DGTS and DGHS (Fig. 13). Labelled DGTS, which is 14Da heavier than unlabelled DGTS (d14DGTS), was detectable within approximately one hour of labelling and increased steadily over the time course, consistent with rapid labelling of the SAM pool, and efficient Bta1 activity. Labelled DGHS (d5DGHS) becomes detectable as early as 30 minutes following labelling, and hardly increases with time, consistent with it being a short-lived intermediate that is rapidly converted. At the onset of labelling unlabelled DGTS is expected to be at steady state, therefore as labelled DGTS species are synthesized, the rate of unlabelled DGTS synthesis is expected to decline and eventually reach zero. Instead, these data show a slight

increase in unlabelled DGTS over the pulse, suggesting that the rate of unlabelled DGTS increases during pulsing. This increase is less than 50% and could be due to noise, as these data represent single experiments; the inclusion of biological and technical replicates would be expected to smoothen these random fluctuations.

In lipidomics it is good practice if not necessary, to correct for technical variability between runs, including sample-dependent matrix effects that alter ionization efficiency, as well as variability in extraction sample injection or instrument response. This is typically done by normalizing peak areas to class-matched internal standards (IS). In this experiment however, a DGTS species isobaric to our IS was predicted to be formed *de novo* during pulsing, precluding the use of the IS. I therefore used a DESeq-2-style median-of-ratios normalization (MRN) approach (Anders and Huber 2010) to derive per-sample size factors and apply them to these data to rudimentarily correction for any variability (see Methods, pg. 88). These size factors were derived using all detected PC and triacylglycerol (TAG) species as a reference set. PC and TAG were chosen as a reference set because they are abundant and generally well detected in ESI^+ mode, where their overall signal is suitable for the correction of sample-to-sample scaling differences. The size factors derived for MRN, as well as boxplots to demonstrate the effect of this normalization on global data distribution, are shown in Figure 13 (C-D).

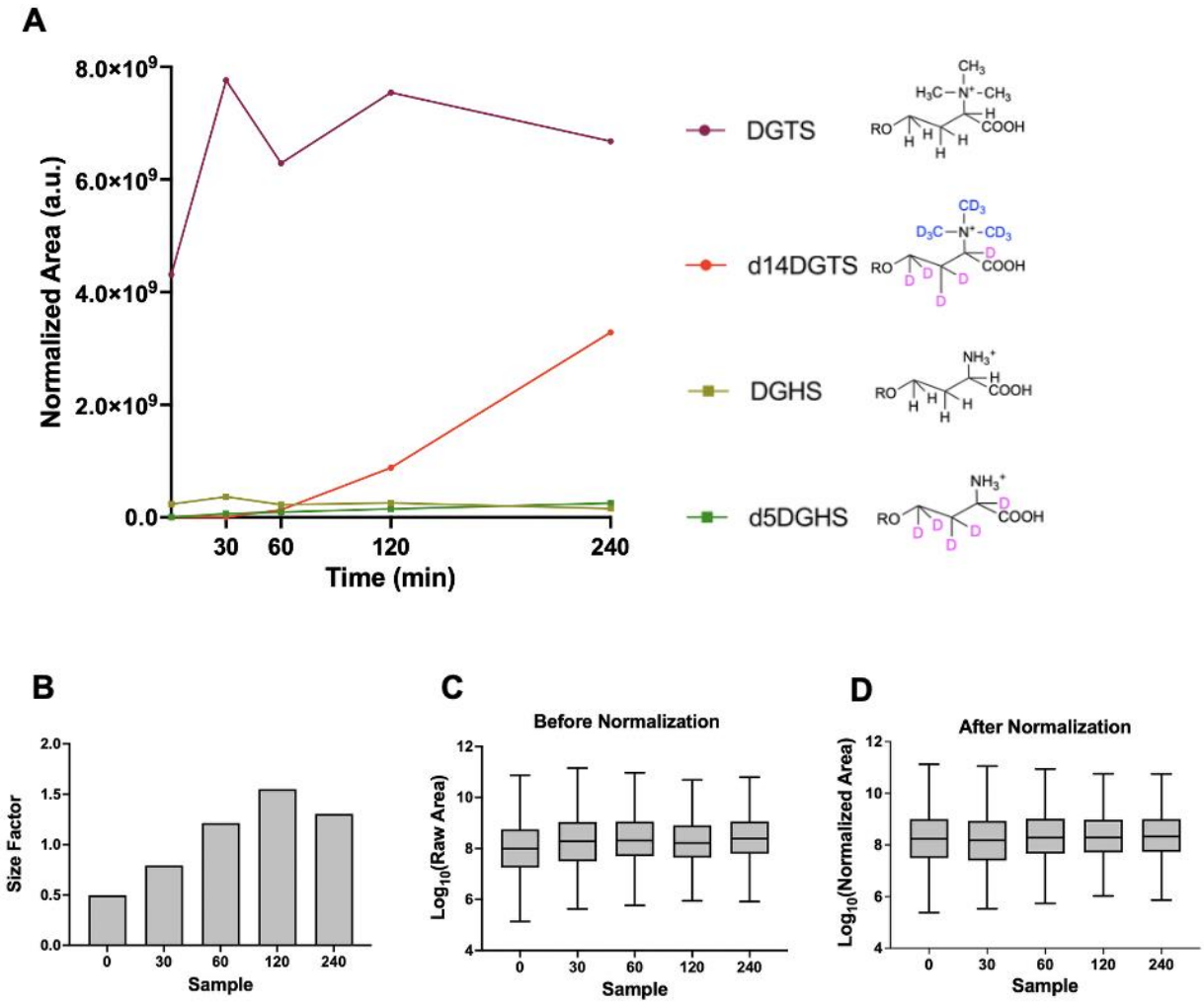

Figure 13. Monitoring the accumulation of DGHS, DGTS, d5DGHS and d14DGTS over 4 hours of pulsing with deuterated methionine. (A) The accumulation of DGHS (chartreuse), d5DGHS (green), DGTS (burgundy) and d14DGTS (red) where each point represents the normalized sum of peak areas for all molecular species observed at a given timepoint. (B) Size factors derived from median-of-ratios normalization. (B) Boxplot showing the log-transformed distribution of all raw peak areas corresponding to DGHS, DGTS, d5DGHS, d14DGTS, PC, and TAG species before normalization and (C) after normalization.

I next considered whether partially labelled DGTS (DGTS isotopologues) were also being synthesized during pulsing. Given the assumption that the initial SAM pool accessed by BtaB is isotopically mixed, and both labelled and unlabelled DGHS contribute as substrates, the synthesis of multiple isotopologues with different combinations of deuterated and undeuterated methyl groups, i.e. d9DGTS (three

deuterated methyl), d6DGTS (two deuterated methyl) and d3DGTS (one deuterated methyl), is expected. Note that d3DGTS was omitted from this analysis because its assignment failed two criteria: it could be detected at the zero-time point and fragment ions not corresponding to those of DGTS were present in its MS/MS spectra. All other DGTS isotopologues were confidently detected throughout pulsing and showcase notably distinct trends (Fig. 14). At 1 hour after pulse initiation, d6DGTS and d9DGTS were the dominant labelled DGTS species, suggesting that DGTS initially forms from the pre-existing unlabelled DGHS pool, which is gradually consumed over time (as shown above). After 1 hour, d8DGTS, d11DGTS, and d14DGTS increase, with d14DGTS exhibiting the most pronounced increase, consistent with the progressive labelling of the SAM pool during the pulse. In principle, the observed distributions could be quantitatively modelled using a binomial framework to estimate the fraction of deuterated SAM at each time point and confirm its dominance over un-deuterated species. However the trends observed are sufficient to demonstrate efficient metabolic labelling of DGTS, which is central to the utility of this method in tracking the movement of newly synthesized lipids.

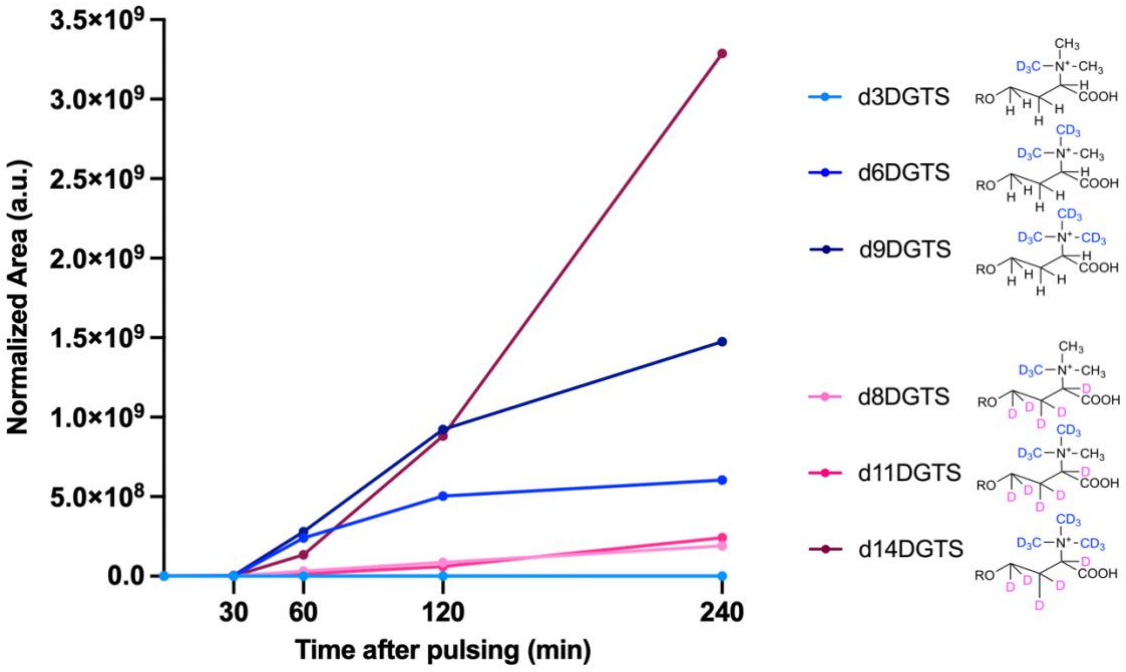

Figure 14. The accumulation of DGTS isotopologues across 4 hours of pulsing with deuterated methionine. Each point represents the summed peak area for all molecular species observed at a given time point, for a given isotopologue. Species in blue are formed from unlabelled DGHS: d3 DGTS (light blue), d6DGTS (midnight blue), d9DGTS (dark blue). Species in pink/red are formed from d5DGHS: d8DGTS (light pink), d11DGTS (fucia), d14DGTS (maroon). Peak areas were normalized using size factors shown in Fig. 13C. Chemical structures for the trimethylhomoserine headgroup of DGTS are shown on the right for visualization of DGHS-derived deuterium atoms (pink), and DGTS-specific deuterium atoms (blue).

Chapter 2. Towards using mBLT to monitor inter-organelle lipid transport: the generation and expression of BtaA and BtaB

Bicistronic expression and visualization of *Kl*Bta1ΔB targeted to the mitochondrial matrix and *Cr*Bta1ΔA targeted to the outer lysosomal membrane

In Chapter 1 I confirmed expression and enzymatic activity of full-length Bta1 from *C. reinhardtii* or *K. lactis* in HeLa cells. Here I assessed whether the enzyme could be separated into its constituent enzymatic domains, BtaA and BtaB, to eventually target each one to distinct organelles and monitor inter-organelle lipid transport.

During the initial development of the BLT method in yeast, BtaA and BtaB from bacteria (*Rhodobacter sphaeroides*) were tested first, circumventing the need to engineer domain separations because they are encoded as two distinct polypeptides, unlike the bifunctional Bta1 found in *C. reinhardtii* and *K. lactis*. In those yeast experiments, fluorescently tagged *Rs*BtaA and *Rs*BtaB were targeted to different organelles using appropriate targeting sequences; however, robust co-localisation was observed regardless of targeting, suggesting that cytosolic heterodimerization precluded independent post-translational organellar targeting. To limit this possibility, I sought to use Bta1 enzymes from different species (*C. reinhardtii* and *K. lactis*) made monofunctional by mutation.

Initially, however, I attempted to monofunctionalize *Kl*Bta1 and *Cr*Bta1, by removing the BtaA domain in one, and the BtaB domain in the other, thereby generating *Kl*Bta1ΔB and *Cr*Bta1ΔA. For either species, I selected a site of truncation within the

inter-domain region which was predicted by AlphaFold2 to be flexible and lack well-defined secondary structure (Fig. 15) (Jumper et al., 2021). The overall fold of the putative BtaA and BtaB domains in the full-length proteins appear to be preserved well in the predicted structures for *Kl*Bta1ΔB and *Cr*Bta1ΔA.

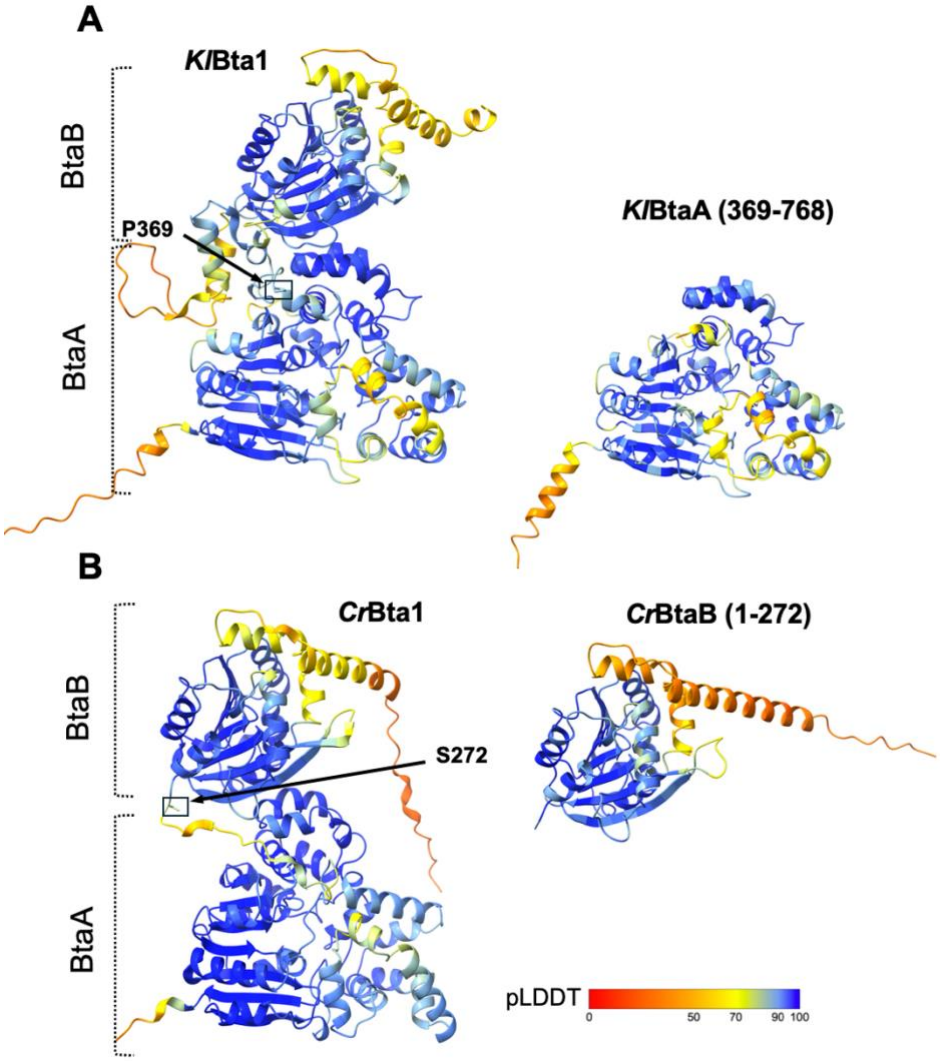

Figure 15. AlphaFold2-predicted structures of *Cr*Bta1, *Kl*Bta1, *Cr*Bta1ΔA, and *Kl*Bta1 ΔB. (A) Predicted structures for full-length *Kl*Bta1 (left) and *Kl*Bta1ΔB (right), generated by truncation at P369 as indicated **(B)** Full-length *Cr*Bta1 (left) and *Cr*Bta1ΔA (right), generated by truncation at S272 as indicated. Structures are shown in cartoon representation and coloured by AlphaFold2 per-residue confidence (pLDDT), with dark blue indicating very high confidence and yellow indicating lower confidence.

The resulting truncated domains were incorporated into a single bicistronic expression construct using the self-cleaving P2A peptide, ideally enabling near-stoichiometric expression of both proteins (Kim et al. 2011). As a preliminary exploratory step toward downstream project aims, *Kl*Bta1ΔB was targeted to the mitochondrial matrix, by N'terminal fusion to the Su9 presequence, while *Cr*Bta1ΔA was targeted to the lysosomal membrane by N'terminal fusion to the lysosome-associated membrane protein 1 (LAMP1) (Fig. 16A). Given that LAMP1 is a Type-1 transmembrane protein, this fusion was predicted to position *Cr*Bta1ΔA on the cytosolic face of the lysosomal membrane, where SAM is abundant. To confirm these proteins' subcellular localisation *Kl*Bta1ΔB was C'terminally fused to mCh and *Cr*Bta1ΔA to GFP (Fig. 16A). As shown in Figure 16B, bicistronically expressed Su9-*Kl*Bta1ΔA-mCh shows characteristic mitochondrial localisation, although as observed with the full-length enzyme, mitochondria appear stressed. LAMP1-*Cr*Bta1ΔB-GFP appears as punctate signals characteristic of lysosomal localisation (Fig. 16B). To confirm these visual impressions, independent labelling of these target organelles should have also been conducted. For example, by immunolabelling with a mitochondrial marker (TOM20) and counterstaining cells with a fixable pH-dependent lysosomal dye such as LysoTracker to assess the extent to which LAMP1-*Cr*Bta1ΔB-GFP localizes to *bona fide* lysosomes. The latter confirmation is important given that at steady-state, LAMP1 localizes to lysosomes as well as to late endosomal and trans-golgi-associated compartments (Baba et al. 2020).

A

B

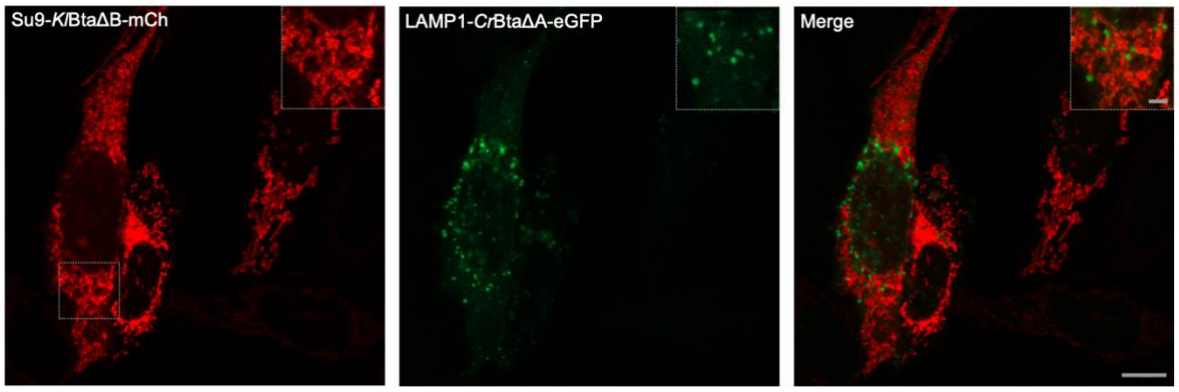

Figure 16. Construct design and visualization of Su9-*Kl*Bta1ΔA-mCh and LAMP1-*Cr*Bta1ΔA-GFP. (A) Schematic representing the open reading frame designed for bicistronic expression of Su9-*Kl*Bta1ΔA-mCh and LAMP1-*Cr*Bta1ΔA-GFP **(B)** Representative multichannel image of HeLa cells bicistronically expressing Su9-*Kl*Bta1ΔA-mCh (left) with apparent mitochondrial localisation and LAMP1-*Cr*Bta1ΔA-GFP (middle) with apparent lysosomal localisation. Scale bars = 10μm.

Upon closer inspection of Figure 16B, there appears to be an apparent absence of GFP signal in two of three mCh-positive cells within the field of view. This raised the possibility that P2A-mediated ribosomal skipping, or 'cleavage' was inefficient. To investigate this, protein expression was analysed by western blotting, using anti-GFP and anti-RFP antibodies. Probing for RFP revealed a band at ~85 kDa corresponding to Su9-KlBta1ΔA-mCh, faint intermediate bands at ~70 and ~55 kDa, and two strong bands at ~30 and ~25 kDa corresponding to mCh-P2A and free mCh (Fig. 17). This pattern is consistent with progressive degradation of the upstream product by matrix-resident proteases following Su9-mediated import, with the

protease-resistant mCh accumulating as a stable end-product (Fig. 17) (Quirós et al., 2015; Shaner et al., 2004). In contrast, probing for GFP revealed a smeary band at ~ 190 kDa, and a faint band at 25 kDa (Fig. 17). LAMP1 is a type I membrane protein with a heavily glycosylated N'terminal luminal domain, which results in a ~ 60-70 kDa upward shift in migration on blots (Carlsson et al., 1988). Un-glycosylated LAMP1-*Cr*Bta1ΔB-GFP is expected to migrate at ~ 120 kDa (orange arrow, Fig. 17). The absence of this band and the presence of a band at ~ 190 kDa suggests that N'-terminal glycosylation, which produces a characteristic smeared band on SDS-PAGE, and thus ribosomal skipping is occurring (Fig. 17). Notably, the weight of the uncleaved product, Su9-*Kl*Bta1ΔA-mCh-P2A-LAMP1-*Cr*Bta1ΔA-GFP, is approximately 180 kDa, thus could sit very close to cleaved product. However, the absence of a corresponding band at this weight when blotting for RFP suggests that ribosomal read-through is not occurring. Therefore, the apparent absence of GFP signal in some mCh-positive cells (Fig. 16B) is not likely caused ribosomal read-through, but rather ribosomal fall-off; a distinct, well-documented inefficiency of 2A peptides in which the ribosome dissociates from the mRNA following release of the upstream protein, failing to translate the second cistron (Kim et al., 2011). This results in non-stoichiometric expression of both cistrons. Inspection of the amino acid sequence of this construct also revealed the absence of the N-terminal glycine residue within the Gly-Ser-Gly (GSG) linker immediately preceding the 2A sequence. Though not strictly required, inclusion of this linker is known to enhance ribosomal skipping efficiency (Wang et al. 2015). It is possible that ribosomal fall-off was

increased by this absence of this residue, or potentially the influence of neighbouring amino acids flanking the P2A sequence.

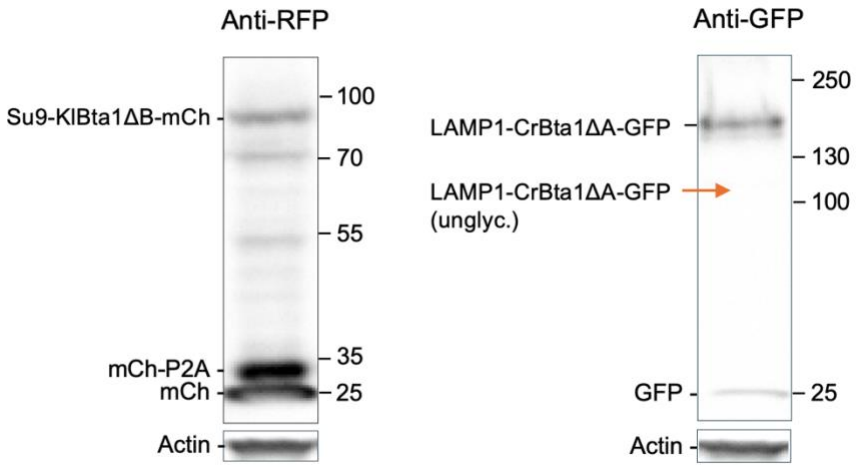

Figure 17. Western blot analysis of protein lysates from HeLa cells expressing Su9-KlBta1ΔB-mCh-P2A-LAMP1-CrBta1ΔA-GFP (**left**) Probing with an anti-RFP antibody revealed a correctly sized band for Su9-KlBta1ΔB-mCh as well as a bands with sizes corresponding to mCh, and mCh appended to the P2A sequence, as well as other unknown products (**right**) Probing with an anti-GFP antibody revealed a band corresponding to the size of LAMP1-CrBta1ΔA-GFP (with LAMP1 glycosylated). The expected size of LAMP1-CrBta1ΔA-GFP where LAMP1 is not glycosylated is marked with an orange arrow. β-actin was used as a loading control for both blots.

Bicistronic expression of KlBta1ΔB and *Cr*Bta1ΔA co-targeted to the cytosolic face of the ER

To more simply approach the functionality of *Kl*Bta1ΔB and *Cr*Bta1ΔA, the C-terminally fluorescently tagged enzymes were co-targeted to the cytosolic side of the ER-membrane using the C-terminal tail-anchor of ubiquitin-conjugating enzyme 6 (UBC6TA), a well-validated ER-targeting module that is conserved from yeast to humans (Fig. 18A) (Kornmann et al. 2009). In retrospect, targeting both enzymes to the same compartment should have been explored first, as it might be more forgiving. Additionally, the N-terminal glycine residue of the GSG linker in the P2A

sequence was added to restore efficient ribosomal skipping if its absence was in fact the cause. As shown in Figure 18, co-expression of *Kl*Bta1ΔB-mCh-UBC6TA and *Cr*Bta1ΔA-GFP-UBC6TA was consistent with localisation to the ER membrane, characterized by a continuous, tubular network. To assess DGHS and DGTS synthesis, I performed LC-MS/MS on lipid extracts from cells expressing ER-targeted *Kl*Bta1ΔB and *Cr*Bta1ΔA. Unfortunately, neither DGHS nor DGTS were detectable. The expression of *Cr*Bta1ΔA and *Kl*Bta1ΔB was not further investigated.

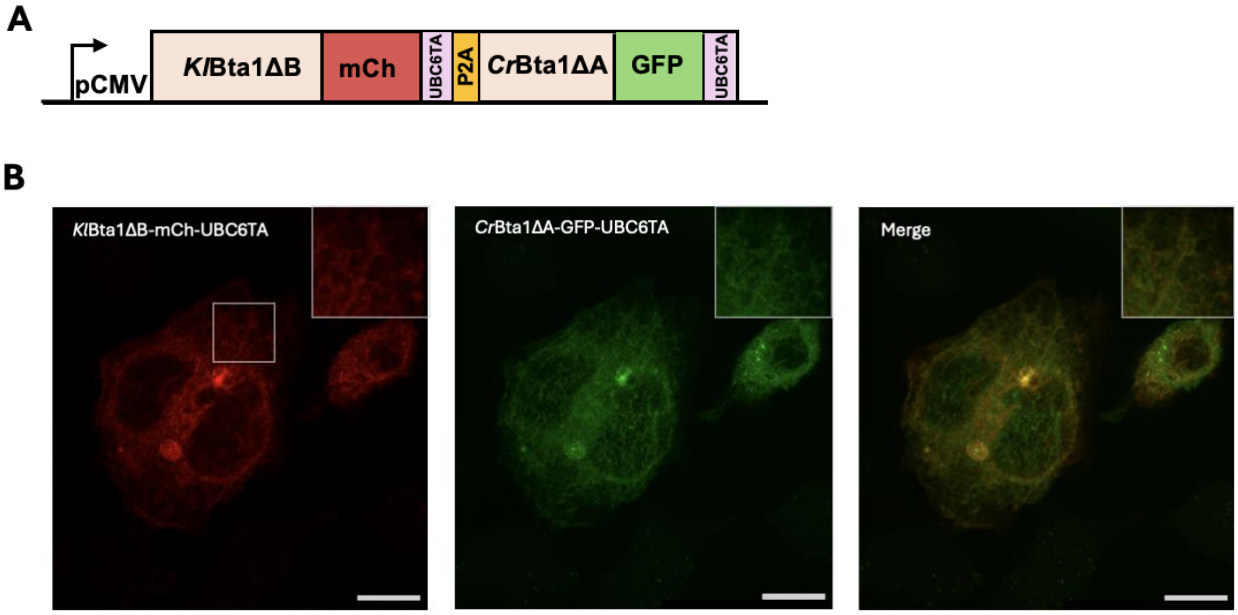

Figure 18. Construct design and visualization of *Kl*Bta1ΔB-mCh-UBC6TA *Cr*Bta1ΔA-GFP-UBC6TA (A) Schematic representing the open reading frame designed for bicistronic expression of *Kl*Bta1ΔB-mCh-UBC6TA and *CrBta1ΔA-GFP-UBC6TA* **(B)** Representative multichannel image of HeLa cells bicistronically expressing *Kl*Bta1ΔB-mCh-UBC6TA (left), *Cr*Bta1ΔA-GFP-UBC6TA (middle), and a composite (right). Scale bars = 10μm

Co-expression of *Kl*BtaA and *Kl*BtaB generated by mutagenesis of *Kl*Bta1, co-targeted to the cytosolic face of the ER

In a second attempt to separate BtaA from BtaB activity, guided by the results recently obtained from BLT in yeast (*Lin, Laurent* et.al, in prep.) single amino acid substitution mutagenesis was performed on residues shown in published work performed on *Cr*Bta1, to be important for SAM-binding activity (Riekhof et al. 2005). This mutagenesis effectively disables one of the two domains, rendering the full-length protein monofunctional. Analogous residues were identified in *Kl*Bta1 by multiple-sequence alignment of the two sequences. In the following experiments, I use *Kl*Bta1 (I110A–D111A), hereafter referred to as *Kl*BtaA, and *Kl*Bta1 (V396A–D397A), hereafter referred to as *Kl*BtaB (Fig. 19A, Supplementary Fig. 2). *Kl*BtaA and *Kl*BtaB were evaluated prior to their *C. reinhardtii* counterparts due to the order in which the constructs were cloned, with the broader aim of testing all combinations at a later stage.

ER-targeted *Kl*BtaA-mCh-UBC6TA and *Kl*BtaB-GFP-UBC6TA were subcloned from yeast expression vectors, generated during development of BLT in yeast, into mammalian expression vectors (Fig. 19A). This approach was taken as a way to save time and avoid having to re-engineer these mutations. However, alongside this approach comes the limitation that the resulting constructs retained yeast-optimised codon usage, which is certainly suboptimal for mammalian expression. These constructs were not incorporated into a P2A-containing vector, to allow for independent evaluation of each protein's functionality prior to bicistronic expression,

an aspect that had not been considered in the experiments described above. Co-expression of *Kl*BtaA-mCh-UBC6TA and *Kl*BtaB-GFP-UBC6TA was consistent with co-localisation to the ER membrane, which was independently assessed by expression of GFP-UBC6TA as a positive control (Fig. 19B-C).

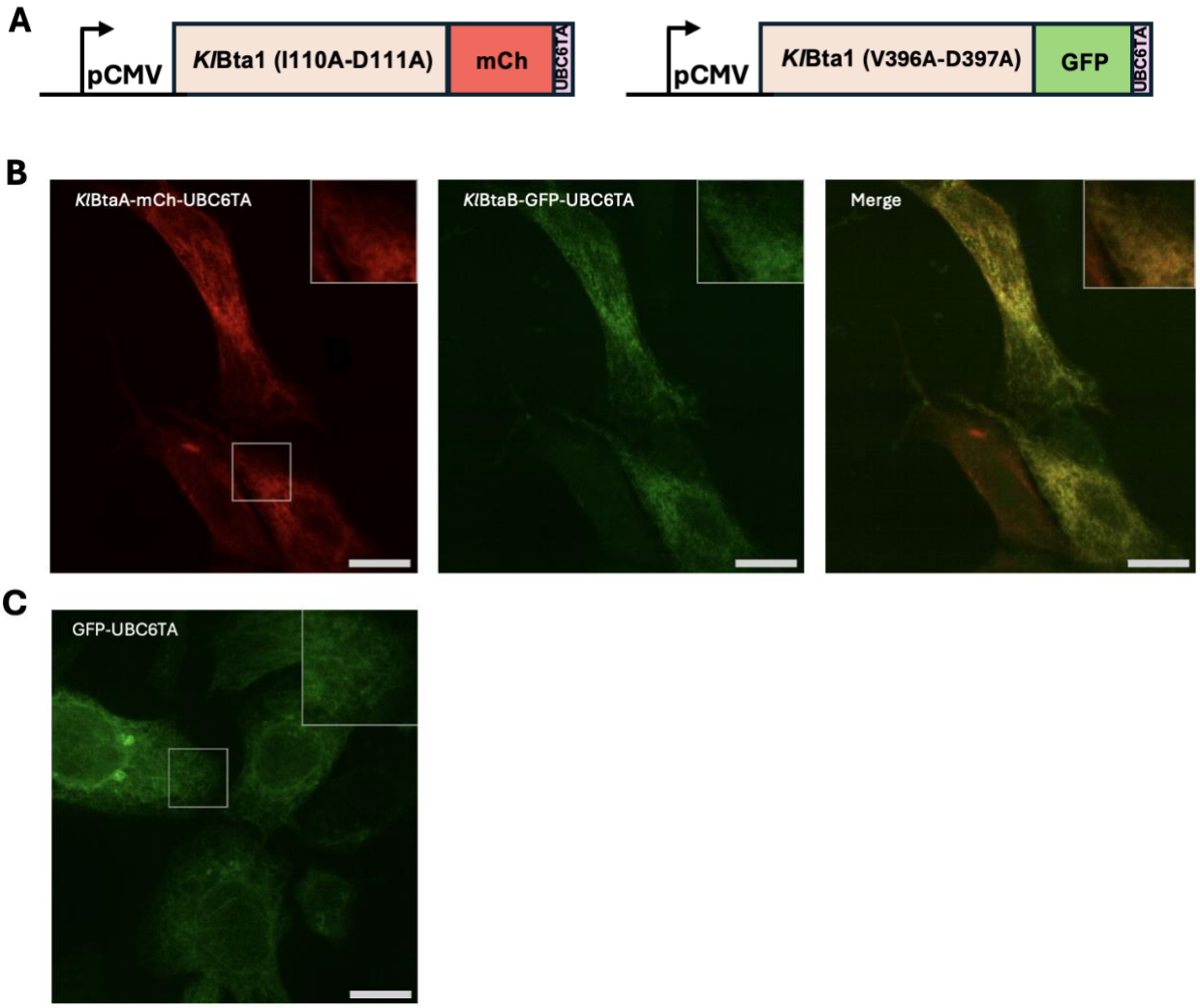

Figure 19. Construct design and visualization of *Kl*Bta1(I110A-D11A)-mCh-UBC6TA (KlBtaA-mCh-UBC6TA) and *Kl*Bta1(V396A-D397A)-GFP-UBC6TA (KlBtaA-mCh-UBC6TA) in HeLa cells (A) Schematic representing the open reading frames of *Kl*BtaA-mCh-UBC6TA (left) and *Kl*BtaB-*GFP-UBC6TA* (right) **(B)** Representative multi-channel image of HeLa cells co-transfected with *Kl*BtaA-mCh-UBC6TA and *Kl*BtaB-GFP-UBC6TA. Scale bar = 10µm. **(C)** Representative image of GFP-UBC6TA, used as a positive control to assess ER-localisation. Scale bar = 10µm.

To assess enzymatic activity at the ER, DDA LC-MS/MS was performed on lipid extracts from cells expressing *K*lBtaA-mCh-UBC6TA alone, *K*lBtaB-GFP-UBC6TA alone, or both enzymes. In cells expressing KlBtaA alone, 34:1 DGHS was detected (Fig. 20A). By contrast, neither DGHS nor DGTS was detected in cells expressing KlBtaB alone. When both enzymes were expressed, 34:1 DGTS was detected (Fig. 20B), whereas DGHS was no longer detectable. Biologically, DGHS is expected to be a short-lived intermediate, especially when both enzymes are co-localised, therefore rapid conversion to DGTS and thus low steady-state DGHS might explain the lack of DGHS signal in doubly transfected cells. Note that due to the nature of data-dependent acquisition (DDA), no EICs can be generated for undetected species. The EICs shown correspond to the only DGHS/DGTS species observed, consistent with 34:1 representing the most abundant cellular DAG species and with other species most likely falling below the effective detection threshold (1×10^5). Notably, the peak intensity for 34:1 DGTS in cells co-expressing *K*lBtaA-mCh-UBC6TA and *K*lBtaB-GFP-UBC6TA is reduced by roughly 1,000-fold, relative to cells expressing the full-length enzyme, Su9-*K*lBta1-eGFP. This reduction in intensity is larger than can be accounted for by low co-transfection efficiency alone: a co-transfection efficiency of ~5% here, compared to ~ 45% for Su9-*K*lBta1-eGFP alone, should only result in a tenfold decrease in signal. This suggests that other biological factors, such as suboptimal enzyme activity are contributing to low lipid abundance.

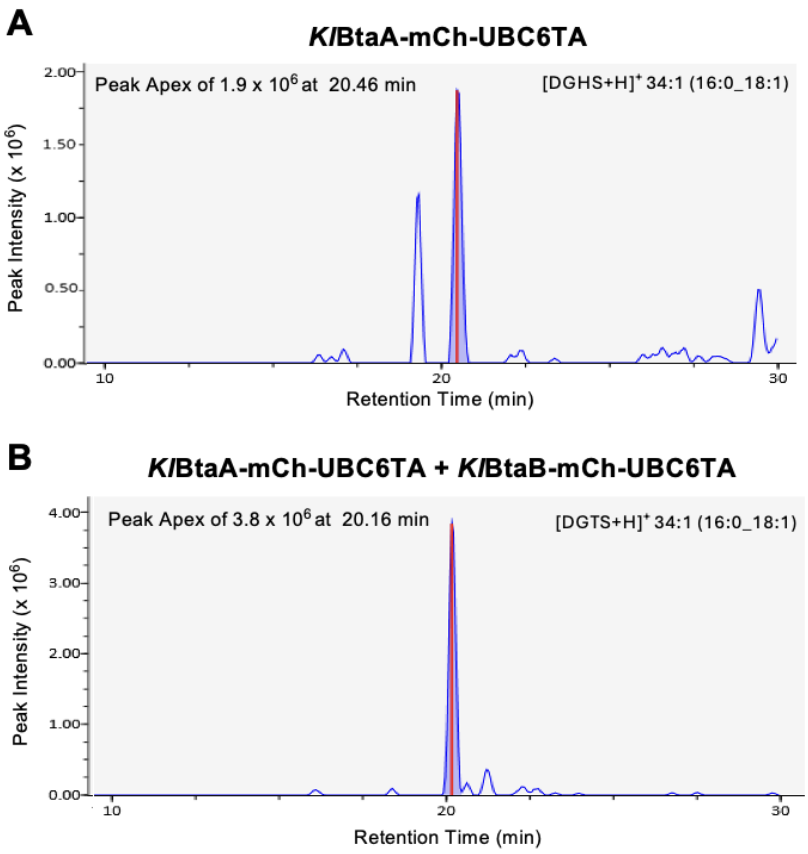

Figure 20. Extracted ion chromatograms for DGHS and DGTS from HeLa cells expressing *Kl*BtaA-mCh-UBC6TA alone or *Kl*BtaA-mCh-UBC6TA and *Kl*BtaB-GFP-UBC6TA. (A) Processed extracted ion chromatogram for 34:1 (16:0_18:1) $[DGHS+H]^+$ observed in samples derived from HeLa cells expressing *Kl*BtaA-mCh-UBC6TA alone and (**B**) Processed extracted ion chromatogram for 34:1 (16:0_18:1) $[DGTS+H]^+$ (right) observed in samples derived from HeLa cells expressing *Kl*BtaA-mCh-UBC6TA and *Kl*BtaB-GFP-UBC6TA.

Co-expression of *Kl*BtaA targeted to the mitochondrial matrix, and *Kl*BtaB targeted to the outer lysosomal membrane

Having confirmed the functionality of *Kl*BtaA and *Kl*BtaB, I next generated Su9-*Kl*BtaA-mCh and LAMP1-*Kl*BtaB-eGFP to approach studying directional lipid transport from the mitochondrion to the lysosome during mitophagy (Fig. 21A). I first co-expressed Su9-*Kl*BtaA-mCh and LAMP1-*Kl*BtaB-eGFP to assess if lipid transport could be observed from the mitochondria to the lysosome under basal conditions. DGHS was not detectable in samples derived from cells expressing Su9-*Kl*BtaA-mCh alone, or in combination with LAMP1-*Kl*BtaB-eGFP. However, two distinct species of DGTS were detected in samples co-expressing Su9-*Kl*BtaA-mCh and LAMP1-*Kl*BtaB-eGFP: 32:1 (16:0_16:1) DGTS (Fig. 21B) and 34:1 (16:0_18:1) DGTS (Fig. 21C). This result is incongruous, as robust detection of multiple DGTS species necessarily implies the prior synthesis of DGHS by BtaA. The absence of detectable DGHS in this experiment, as well as the experiment above, therefore, reflects a technical limitation rather than a true lack of synthesis. This limitation is particularly problematic in the context of mBLT, where the extent of lipid transport is quantified as the ratio of newly synthesized DGTS to the sum of newly synthesized DGTS and DGHS; reliable detection of both lipid species is therefore required for the utility of this method.

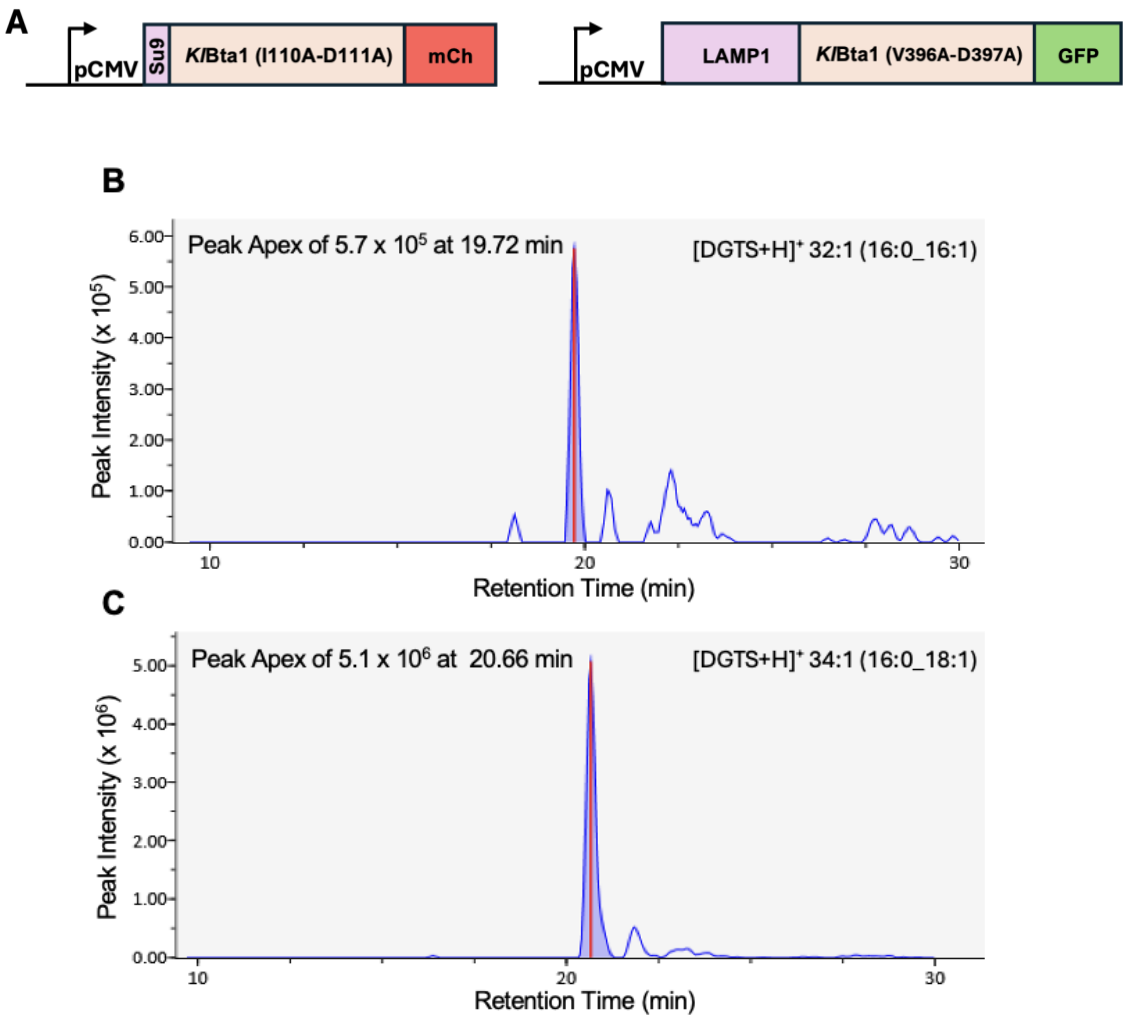

Figure 21. Construct design and detection of DGHS and DGTS synthesis in HeLa cells co-expressing Su9-*Kl*BtaA-mCh and LAMP1-*Kl*BtaB-eGFP. (A) Schematic representing the open reading frames of Su9-*Kl*BtaA-mCh (left) and LAMP1-*Kl*BtaB-eGFP (right) **(B)** Processed extracted ion chromatogram for 32:1 (16:0_16:1) $[DGTS+H]^+$ and **(C)** 32:1 (16:0_16:1) $[DGTS+H]^+$ detected in samples derived from HeLa cells co-expressing Su9-*Kl*BtaA-mCh and LAMP1-*Kl*BtaB-eGFP.

To address the persistent issues with detection outlined above, I explored potential modifications to the acquisition parameters used for untargeted DDA LC-MS/MS which could increase the detectability of DGHS and DGTS. In line with this, I considered two non-mutually exclusive strategies to improve detectability: naturally

increasing the lipids' abundance by expanding the proportion of cells expressing both enzymes and increasing analytical sensitivity at the level of the acquisition parameters used in LC-MS/MS. Given the extended timeline required to generate stable cell lines, I pursued the latter approach.

To increase sensitivity for DGHS and DGTS detection, MS^1 acquisition parameters were deliberately adjusted in three ways. First, the effective MS^1 intensity threshold for MS/MS precursor selection was lowered from 1×10^5 , as used in previous untargeted DDA experiments, to 2.5×10^4. This modification was intended to allow for fragmentation of lower-abundance precursors. Secondly, I generated an inclusion list to guide the selection of precursors corresponding to DGTS and DGHS species for MS/MS. The inclusion list contained the exact *m/z* (to 3dp) for all DGHS and DGTS species previously observed in experiments expressing full-length Bta1, as well as their fully labelled counterparts (d5DGHS and d14DGTS) which will be synthesized during pulsing. Additionally, the retention time window for precursor selection was confined to between 17 and 25 minutes, corresponding to the expected chromatographic elution range of DGHS and DGTS species, limiting fragmentation of precursors outside this region. Collectively, these changes were implemented to improve MS/MS sampling of DGHS and DGTS species.

Studying lipid transport during mitophagy as a proof-of-concept for mBLT

To obtain a modest proof-of-concept for mBLT, I explored lipid transport from the mitochondria to the lysosome during PTEN-induced kinase 1 (PINK1)/Parkin-dependent mitophagy, induced by treating HeLa cells with an uncoupler of oxidative phosphorylation, carbonyl cyanide m-chlorophenyl hydrazine (CCCP) (Narendra et al. 2008). CCCP is a protonophore which increases the conductance of protons across the inner mitochondrial membrane (IMM), causing mitochondrial depolarization (Kasianowicz et al. 1984). Loss of the mitochondrial membrane potential blocks the import of PINK1, causing its accumulation on the OMM and subsequent recruitment of the E3 ubiquitin ligase, Parkin (Greene et al. 2012). Parkin then ubiquitinates key OMM proteins, some of which are targetted for proteasomal degradation, others which recruit autophagic machinery to target the bulk of mitochondria for degradation by autophagy (Yoshii et al. 2011).

A further motivation for this experiment stems from the limited understanding of the fate of mitochondrial lipids during mitophagy: specifically, whether these lipids are completely degraded within the lysosomal lumen or whether they can be salvaged and redistributed to other cellular compartments, including cytoplasmic lipid pools. I approached this biological question using mBLT by testing whether newly synthesised DGHS generated by mitochondrially localised BtaA becomes increasingly accessible to lysosomal BtaB enzymatic activity during mitophagy; such would be implied by an increase in DGTS production, or an increased effective lipid

transport rate, relative to a negative control where mitophagy is not induced (Fig. 22).

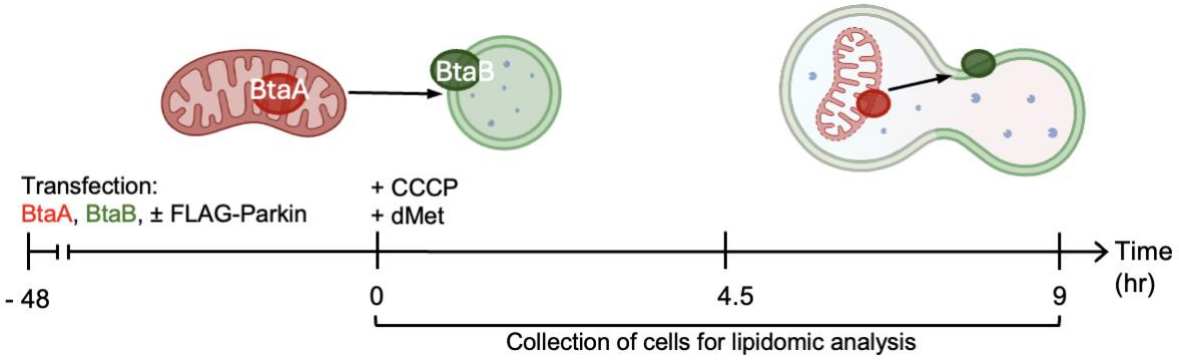

Figure 22. Graphic to visualize experimental conditions CCCP-induced mitophagy mBLT experiment.

The question of whether mitochondrial lipids are salvaged during mitophagy was approached through a deliberately crude, first-pass metabolic labelling experiment in CCCP-treated HeLa cells. Additionally, HeLa cells express little to no endogenous Parkin, an E3-ubiquitin ligase required for the ubiquitination of outer mitochondrial membrane proteins which recruits autophagic machinery (Denison et al. 2003). As such, an N-terminally FLAG-tagged Parkin construct was generated for transfection together with Su9-*K*/BtaA-mCh and LAMP1-*K*/BtaB-eGFP. Accordingly, 48 hours after transfecting cells with Su9-*K*/BtaA-mCh, LAMP1-*K*/BtaB-eGFP, and FLAG-Parkin or only Su9-*K*/BtaA-mCh and LAMP1-*K*/BtaB-eGFP, as a negative control, media were changed to media lacking L-methionine, supplemented with dMet, and CCCP to a final concentration of 10μM. Published flow cytometry data of HeLa cells expressing the pH-sensitive fluorescent reporter, mt-Keima, show that significant mitophagic clearance occurs after just 6 hours of treatment with 10μM CCCP (Um et al. 2018). Therefore, the time points chosen for cell harvesting during this

experiment were chosen to flank this 6-hour mark where at 4.5 hours post-treatment, we expect few (if any) mitochondria to be engulfed, and at 9 hours, a significant amount. To approach the extent of mitophagy I assessed the co-localisation of FLAG–tagged Parkin, Su9-*Kl*BtaA-mCh, and LAMP1-*Kl*BtaB-eGFP across the duration of CCCP-treatment (Fig. 23).

Visual inspection of Figure 23A shows co-localisation of Su9-*Kl*BtaA-mCh with FLAG-Parkin after 4.5 hours of CCCP treatment, with more extensive and concentrated co-localisation observed at 9 hours, consistent with progression of mitophagy. Notably across all timepoints, some signal corresponding to LAMP1-*Kl*BtaB-eGFP appeared at least partially localised to the ER, or potentially the plasma membrane. Given that this ER-signal was specific to LAMP1-*Kl*BtaB-eGFP which is localized to the cytosolic face of the lysosome, it is possible that contact sites formed between these two organelles during mitophagy. Why this would occur is not clear. More generally, it is possible that overexpression of three proteins in this experiment overwhelmed protein synthesis machinery at the ER, potentially preventing post-translational modifications required for effective targeting mediated by LAMP1. Alternatively, given that LAMP1-*Kl*BtaB-eGFP is synthesized at the ER, this signal may simply reflect newly synthesized protein, in which case its turnover is slow. Nonetheless, this observation inherently weakens possible conclusions drawn on lipid-transport between the mitochondrion and the lysosome. No significant changes in morphology or localisation of mitochondria or LAMP1-positive objects

were observed in the negative control, consistent with CCCP-induced mitophagy requiring Parkin (Fig. 23B).

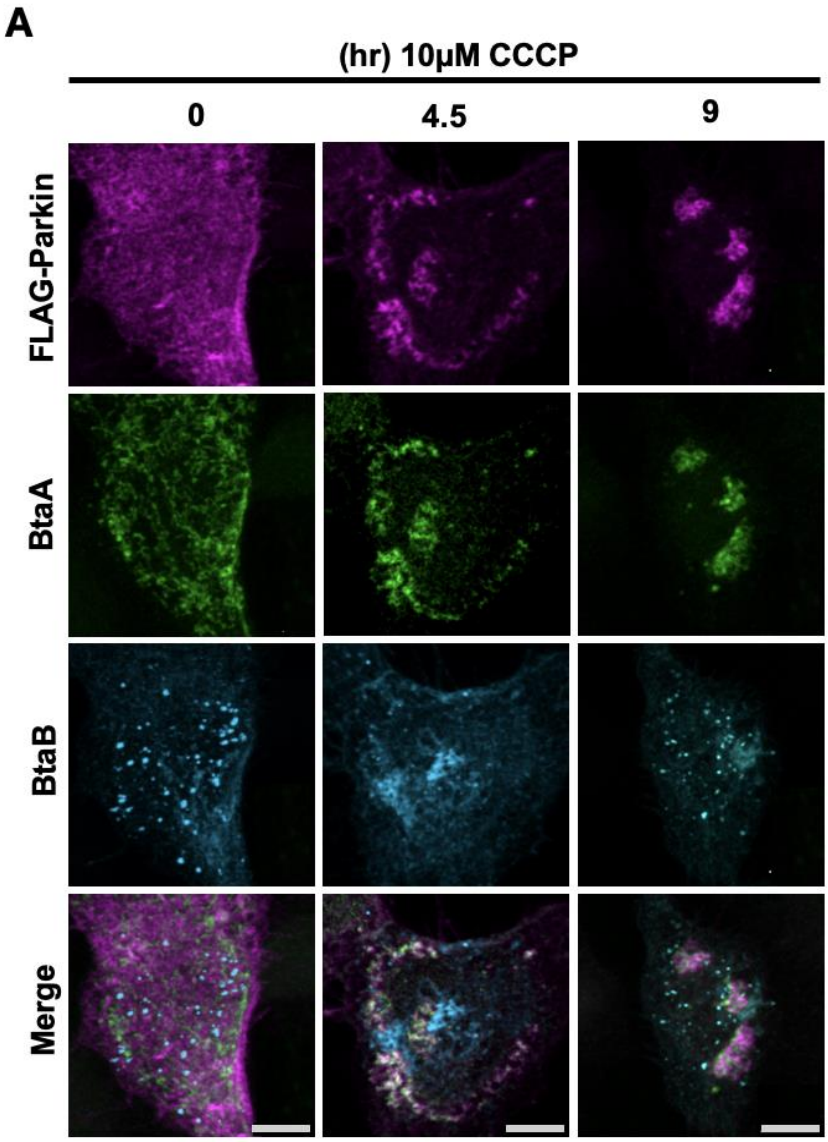

(figure legend is shown on the next page)

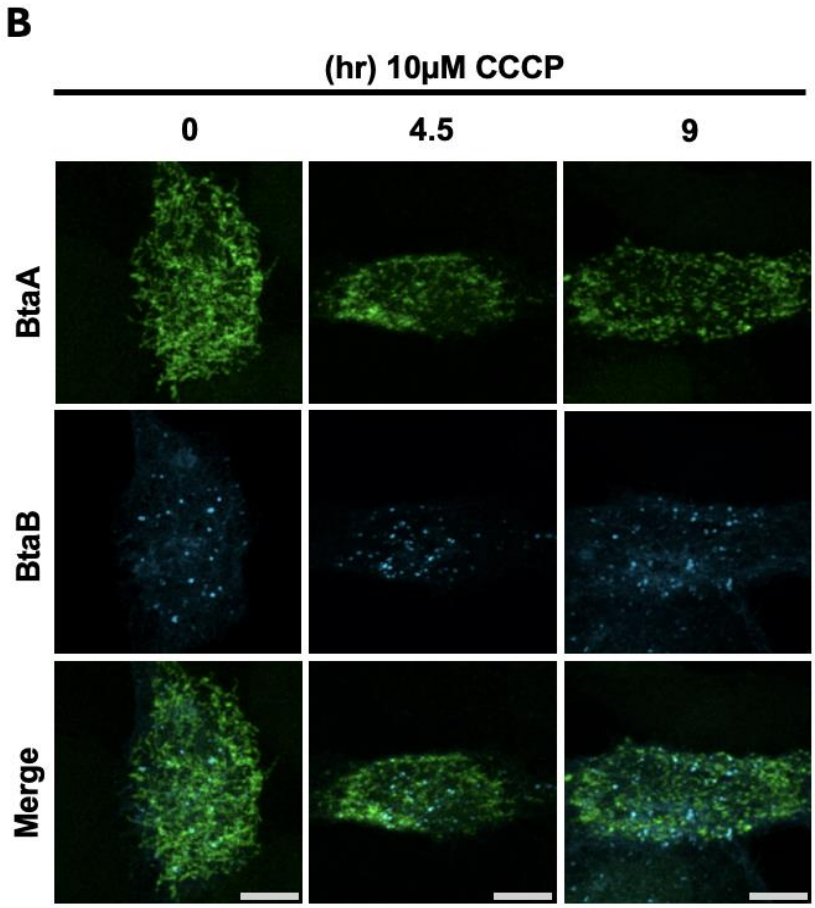

Figure 23. Visualization of triply-transfected HeLa cells expressing Su9-*K*/BtaA-mCh, LAMP1-*K*/BtaB-eGFP and FLAG-Parkin (**A**) Max intensity projections of Z-stack images of HeLa cells expressing FLAG-Parkin visualized using AlexaFluor 647 (first row), Su9-*K*/BtaA-mCh (second row), LAMP1-*K*/BtaB-eGFP (third row), and their composite (last row) after 0, 4.5 hours, and 9 hours of treatment with 10μM CCCP. Scale bars = 5 μm. (**B**) Max intensity projections of Z-stack images of HeLa cells expressing Su9-*K*/BtaA-mCh (first row), LAMP1-*K*/BtaB-eGFP (second row), and their composite (last row) after 0, 4.5 hours, and 9 hours of treatment with 10μM. CCCP. Scale bars = 5 μm.

Unfortunately, neither labelled DGHS and DGTS, nor unlabelled, were detected in lipid extracts derived from these samples, using either the original untargeted DDA LC-MS/MS method, or the inclusion-list-guided method. The absence of any detectable signal in samples run using the original untargeted method is consistent with DGHS and DGTS signal intensities falling below the effective detection limit, a recurring issue throughout this project. Additionally, the MS/MS spectra acquired

using the inclusion-list-guided method were highly complex and chimeric, where numerous fragments were present that were not characteristic of DGHS or DGTS. It is thus plausible that lowering the MS^1 intensity threshold increased sensitivity at the expense of the selectivity afforded by the inclusion list, thus permitting co-fragmentation of lipid species which co-elute within the defined isolation window. Consequently, although precursor selection should have been biased towards DGHS and DGTS, the resulting MS/MS spectra lacked sufficient specificity to support confident identification and subsequent quantification of lipid transport rates. Therefore, this exploratory mBLT flux experiment was inconclusive.

Discussion

Studying inter-organelle lipid transport *in vivo* has remained a major technical challenge, despite a growing appreciation for how lipids and membranes influence

cellular physiology. This difficulty arises from the immense diversity in lipid composition across membranes, and their maintenance by a web of highly redundant pathways. To approach these limitations, the Kornmann lab is developing a BLT which serves as bioorthogonal platform to study organelle-specific lipid transport *in vivo*. As a natural next step following its development in yeast, the aim of this project was to adapt BLT for use in mammalian cells, using HeLa cells, and to explore lipid transport during mitophagy as a proof-of-concept.

To establish the feasibility of adapting mBLT to mammalian cells, I first validated the functionality of Bta1 when heterologusly expressed in HeLa cells by demonstrating that its lipid products, DGHS and DGTS, could be confidently detected by mass spectrometry. Initially, I attempted to do so using SIM LC-MS which despite being sufficient for identification in yeast, proved unsuccessful even when additional enrichment strategies were employed. These enrichment approaches were ineffective because resolution, not lipid abundance, limited detection. More specifically, chromatographic separation and mass alone did not provide sufficient discriminatory power to distinguish DGHS and DGTS signals from the highly complex lipid background of mammalian cells, where isobaric interference was inevitable. Tandem mass spectrometry was therefore crucial for enabling confident identification by providing an additional layer of structural information to use for signal discrimination.

Despite solving the above issue of analytical sensitivity, low DGTS and DGHS abundances afforded by co-expression of *Kl*BtaA and *Kl*BtaB, ultimately hindered the progression of the project towards obtaining a proof-of-concept for mBLT. Namely, when *Kl*BtaA and *Kl*BtaB were co-expressed, DGTS was detected, while DGHS was not. Given that DGTS synthesis requires DGHS, this result likely indicates that DGHS fails to accumulate to a steady-state level which is detectable by DDA LC-MS/MS when enzymes are co-expressed. There are multiple possible explanations for this. Firstly, it could be that the overall activity of *Kl*BtaA (and *Kl*BtaB) are lower than that of Bta1, which is in line with the observation that the signal for 34:1 DGTS decreased by ~1000-fold compared to when the full-length enzyme was expressed alone; a decrease which could not be accounted for by differences in transfection efficiency alone. Additionally, the SAM-binding mutations in these enzymes may have imposed additional penalties that reduce the stability or activity of the remaining functional domain. The use of yeast codon-optimized sequences for *Kl*BtaA and *Kl*BtaB likely also compromised enzyme stability and/or function due to a disruption in co-translational folding (Yu et al. 2015; Walsh et al. 2020). Although protocols were optimized according to standard lab procedure, co-transfection efficiencies for *Kl*BtaA and *Kl*BtaB reached at best ~10%. If DGHS and DGTS abundance scales proportionally with the number of cells co-expressing *Kl*BtaA and *Kl*BtaB, in a stable cell line where enzymes are bicistronically expressed, I would expect around a tenfold increase in abundance. For DGHS, a tenfold increase in abundance might be sufficient to raise its intensity above the MS^1 threshold set for DDA LC-MS/MS.

However, due to a shortage of time within the project timeframe, I did not generate new constructs or cell lines to approach solutions for low lipid abundance. Instead, I addressed this issue by increasing the sensitivity of detection by modifying the original DDA LC-MS/MS method. Such modifications included reducing the MS^1 intensity threshold, adding a precursor *m/z* inclusion list, and narrowing the retention-time window for detection. Implementing all three modifications simultaneously may have been overly ambitious. Prioritizing the use of an inclusion list alone may have been a more effective initial strategy, given that the intensity threshold serves as the primary filter governing precursor selection in untargetted DDA LC-MS/MS. Here, a four-fold relaxation of the MS^1 intensity might have been overly aggressive, where a more conservative adjustment may have better balanced sensitivity with selectivity.

While untargeted DDA LC-MS/MS is advantageous for broad lipid profiling, the BLT method itself relies solely on the accurate and reproducible quantification of DGTS and DGHS. Future efforts to optimize mBLT should therefore strongly consider using targeted acquisition modes such as Parallel Reaction Monitoring (PRM), which can be implemented on the Orbitrap Eclipse, or Selected Reaction Monitoring (SRM), which requires a triple-quadrupole instrument. Although the incorporation of an inclusion list in untargeted DDA, as done here, can bias precursor selection towards lipid species of interest, precursor isolation ultimately remains governed by MS^1 intensity ranking and competitive sampling. By contrast, PRM and SRM approaches enforce MS/MS acquisition for predefined precursors within scheduled retention-

time windows, enabling robust, fragment-ion-based quantification even at very low precursor abundances (Rakusanova and Cajka, 2024). Targeted acquisition approaches may circumvent the need to resolve issues of low lipid abundance by biological optimizations; ideally, however these two should be pursued in parallel to maximize the robustness of identification and quantification.

While the issues described above prevented an exploration on lipid transport during CCCP-induced mitophagy to use as a proof-of-concept for mBLT, I am optimistic that this experiment will be feasible once the mentioned optimization strategies are implemented. In this experiment, the expectation was for lipid transport to be greater at later timepoints, coincident with the spatial convergence between the mitochondria (within the autophagosome) and the lysosome, where such a result would additionally imply that lipids were being recycled at the autophagolysosome. This aside, a caveat in the experimental design of the mitophagy mBLT flux experiment pertains to the effect of CCCP treatment on faithful organellar targeting: CCCP functions by dissipating of the IMM membrane potential which must be in-tact to allow for presequence-dependent protein import (Martin et al. 1991). Therefore, assuming that protein-synthesis is not stalled upon CCCP treatment, newly synthesized Su9-*K*/BtaA-mCh would largely remain cytosolic and if folded, could therefore contribute to spurious DGTS synthesis carried out by LAMP1-*K*/BtaB-eGFP. Employing a Tet-Off expression system in the future would reduce the advent of cytosolic accumulation, where Su9-*K*/BtaA-mCh (and LAMP1-*K*/BtaB-eGFP) are first allowed to accumulate, followed by the addition of doxycycline to halt further

transcription. The addition of doxycycline with a sufficiently long chase period would then give time for newly synthesized proteins to reach their target compartments sufficiently in advance of CCCP treatment.

The complexity of mammalian lipidomic data also introduced challenges at the level of data processing. This complexity complicated efforts to maintain quantitative completeness across timepoints during the pulse-labelling experiment, where low-abundance species were not consistently detected. To aid with peak detection, feature alignment was performed across samples. Feature alignment requires gap-filling, whereby raw data are re-inspected at reference *m/z* and retention times to integrate peaks that were not initially annotated as features. For the pulse-labelling experiment, the latest timepoint was used to generate the reference feature list, under the assumption that labelled DGTS and DGHS species would be most abundant at this stage. In theory, feature alignment improves quantitative completeness. However, it can also introduce artefacts, particularly when near-isobaric species are present. Additionally, these effects are expected to disproportionately affect low-abundance lipids, such as d3DGTS, which was intentionally excluded from the analyses discussed in Chapter 1. In the same experiment, unlabelled DGTS, representing the summed signal of all unlabelled molecular species, was observed to slightly increase over time, when we expected to observe a steady level. It is possible that this trend was driven in part by the quantification of a subset of low-abundance DGTS species which were misannotated under the alignment and gap-filling framework described above.

Together, these observations raise an important conceptual question for the calculation of lipid transport rates in mBLT: should quantification incorporate all detected DGTS molecular species, as done in the past and in this study, or should it be restricted to the most abundant and confidently annotated ones, and to what extent is statistical power or biological information lost in doing so.

Though not done in this study, an assessment of native organelle homeostasis upon enzyme expression is required to confirm utility of mBLT will ultimately require, so as limit any secondary effects on the physiological context under investigation. It was noted that mitochondria in Bta1-expressing cells, as well as BtaA expressing cells though potentially to a lesser extent, appeared morphologically distinct to the control. Upon closer inspection, the affected mitoch[...]ondria do not appear uniformly fragmented as would be expected for mitochondria undergoing fission, a homeostatic process (Smirnova et al., 2001). In response to osmotic, oxidative, or bioenergetic stress, mitochondria adopt a blob- or donut-like morphology by matrix swelling and aberrant end-to-end fusion (Liu and Hajnóczky 2011; Ahmad T. et al. 2013; Long et al. 2015). Such morphologies more closely resemble the phenotype observed in Bta1-expressing cells. One plausible explanation is that the assumed incorporation of matrix-synthesised DGHS and DGTS into the inner mitochondrial membrane (IMM) perturbs local lipid packing. The IMM is uniquely enriched in cardiolipin (CL), whose small anionic headgroup relative to its four acyl chains confers a conical molecular shape that templates regions of negative membrane curvature (Cullis and de Kruijff, 1979; Ikon and Ryan, 2017). This curvature is

required the lateral organisation of respiratory complexes which maintain the proton-motive force and in turn regulate matrix volume (Pfeiffer et al., 2003; Houtkooper and Vaz, 2008). DGTS and DGHS, by contrast, adopt an approximately cylindrical shape which would form flat, planar membranes thus disrupting local curvature (Bolik et al., 2023). Another plausible explanation for the observed phenotype is that overexpression of mitochondrial Bta1 results in the saturation of the multi-subunit translocase of the outer membrane (TOM) complex leading to an accumulation of unfolded and/or misfolded proteins, and a disruption of mitochondrial proteostasis (Wang and Chen 2015; Wrobel et al. 2015). The plausibility of this is low, when considering that overexpression of Su9-eGFP, albeit a much smaller protein, was not associated with stressed mitochondria. Nonetheless, over-expression of a catalytically dead Bta1 mutant, where both BtaA and BtaB domains are mutated, would allow for the discrimination between whether this phenotype is caused the enzyme's lipid-synthesizing activity or non-specific effects relating to protein overexpression.

Given that betaine lipids are not produced in mammalian cells, the biological consequences of their ectopic synthesis cannot be inferred from the yeast and algal contexts in which BLT was originally developed. Betaine lipid-synthesizing organisms grow at substantially lower temperatures than mammalian cells (20–30°C for algae and yeast versus 37 °C for HeLa cells) (Harris, 2001; Sherman, 2002). In turn, the acyl-chain length and unsaturation profile of their lipidome is tuned through homeoviscous adaptation to maintain optimal fluidity at those temperatures (Ernst et

al., 2016). In mammalian cells, betaine lipids may therefore introduce a fluidity mismatch, where bilayer asymmetry maintained by flippases and scramblases which recognise native phospholipid headgroups (Coleman et al., 2013), may also be perturbed by introduction of a non-native zwitterionic species which are not known substrates. In addition, betaine lipid synthesis consumes DAG, which serves as a precursor for many phospholipid biosynthesis, including CL via the CDP-DAG pathway in the mitochondria (Schlame and Greenberg, 2017). Bta1 expression may therefore perturb global lipid turnover by consuming DAG. Future deployment of mBLT should therefore incorporate quantitative readouts of cellular stress; for example, a measurement of mitochondrial membrane potential, ROS production, ER-stress markers, and proliferation rate. Such readouts alongside the lipidomic readout of transport, will ensure that the measurement is reporting on physiological lipid trafficking rather than on a perturbed cellular state.

Conclusion

Together, the findings of this study establish the feasibility of adapting BLT to mammalian systems. Although robust quantification of inter-organelle lipid transport

could not be achieved under conditions where the activities of BtaA and BtaB were spatially separated, efforts to do so enabled the identification of key biological and technical constraints that now can be used to guide further method development. Addressing these limitations will require: i) optimization of enzymatic activity, potentially by computational identification of gain-of-function mutations or directed evolution ii) implementation of more robust expression strategies, including the generation of cell lines and inducible systems and iii) exploration of targeted MS/MS approaches to enable sensitive and selective lipid quantification. While addressing these limitations is necessary for the adaptation of BLT to mammalian systems, the outlined strategies will likely enhance the utility of BLT as a general platform to study lipid transport and potentially benefit BLT in yeast as well.

Materials and Methods

Construct Design

Su9-*Cr*Bta1 and Su9-*Kl*Bta1 were codon-optimized for mammalian expression and purchased for synthesis as plasmids using pcDNA.5 backbones from GenScript. Su9-*Cr*Bta1 was cloned into pEGFP-N3 (now discontinued on Addgene) by BamHI to generate Su9-*Cr*Bta1-eGFP. Su9 was amplified from Su9-*Cr*Bta1 and cloned into pEGFP-N3 using BamHI to generate Su9-eGFP. Su9-*Kl*Bta1 was cloned into pcDNA.5 FRT/TO C'terminal eGFP vector, a gift from James Holder, using HindII to generate Su9-*Kl*Bta1-eGFP. Su9-*Kl*Bta1ΔB-mCh-P2A-LAMP1-*Cr*Bta1ΔA-eGFP and *Kl*Bta1ΔB-mCh-UBC6TA-P2A-*Cr*Bta1ΔA-eGFP-UBC6TA were codon-optimized for mammalian expression and purchased for synthesis using pcDNA.5 backbones from GenScript. *Kl*BtaA-mCh-UBC6TA was subcloned from a yeast vector into a pcDNA5 FRT/TO vector, a gift from James Holder, to allow for mammalian expression. *Kl*BtaB was amplified from a yeast plasmid and subcloned into pcDNA.5 FRT/TO using AflII and XhoI. GFP-UBC6TA was amplified from another yeast plasmid and cloned in-frame with *Kl*BtaB (above) using NotI to generate *Kl*BtaB-GFP-UBC6TA, and into pcDNA5 FRT/TO alone to generate GFP-UBC6TA. Plasmids containing Su9-*Kl*BtaA-mCh and LAMP1-*Kl*BtaB-eGFP were generated by assembling inserts amplified from plasmids previously described, using In-Fusion Snap Assembly Kit (Takara Bio). Lastly, Parkin was amplified from YFP-Parkin (Addgene plasmid # 23955 from Richard Youle's lab) and cloned in-frame with the FLAG sequence in the pcDNA.5-FRT/TO N-terminal FLAG vector, a gift from Caleb Bately, a postgraduate student in the Barr lab.

Cell Culture and Transient Transfection

HeLa cells were grown in Dulbecco's Modified Eagle Medium (DMEM), supplemented with 10% foetal calf serum (FBS) and 1% penicillin-streptomycin at 37 °C and 5% CO2. In preparation for transfection, cells were seeded into 6-well plates, to reach a cell density of 1 x 10^6 by the time of transfection which was performed using polyethyleneimine MAX (Kyfora Bio) diluted in Opti-MEM media (Thermo Fisher Scientific).

Generation of a Su9-*Kl*Bta1-eGFP-expressing cell line

A stable Flp-In™ TREx™ host cell line was generated by James Holder, a PostDoc in Gergely Lab. A plate of cells was kindly gifted to the Kornmann lab and subsequently expanded before co-transfection with the Su9-*Kl*Bta1-eGFP-FRT-TO plasmid, and the Flp-recombinase-expressing plasmid, pOG44 (plasmid #209087 on Addgene) using the standard transfection protocol outlined above. Stable transfectants were selected using hygromycin at a concentration of 500 µg/ml, for approximately 12 days before selecting two clonal populations which were verified by fluorescence microscopy after inducing expression with doxycycline at a concentration of 0.5µg/mL.

Immunofluorescence and Fluorescence Microscopy

Cells were fixed in 4% paraformaldehyde for 10 min in the dark, at room temperature. For visualization of FLAG-tagged Parkin, immunofluorescence was performed. Coverslips were permeabilized using 2% Triton-X100 and blocked using 5% BSA solution for 45 minutes. Coverslips were then incubated with anti-FLAG mouse monoclonal primary antibody for 1 hour (F3165, Sigma Aldrich), followed by incubation with a goat anti-mouse secondary antibody conjugated to Alexa Fluor 647 (ab150115, Abcam). Coverslips were mounted onto glass slides using ProLong Glass Antifade Mountant (Thermo Fisher Scientific) and allowed to cure for at least 24 h at room temperature prior to imaging.

Images were acquired using a spinning-disk Ultraview confocal system (PerkinElmer) mounted on an IX81 Olympus inverted microscope, equipped with an EM-CCD camera (Hamamatsu Photonics) and a 40× oil-immersion objective (NA = 1.35), at room temperature (Figures 6, 17, and 18), or on an upright Zeiss LSM 980 confocal microscope using a 40× oil-immersion objective (NA = 1.35), at room temperature (Figures 2, 15, and 22). For Figures 22A and 22B, a gallium arsenide phosphide photomultiplier tube (GaAsP-PMT) area detector was used to enable Airyscan imaging and 3D-image processing using local ZEN software. Figure legends indicate where max-intensity projections were made from Z-stacks. No additional modifications were made to any images.

Calculation of Transfection Efficiency

Fixed samples were imaged on an Echo Revolve upright microscope using an Olympus 10× Apochromat objective. Fluorescence images were acquired using the following LED filter cubes: DAPI (to stain cell nuclei), FITC (for GFP-tagged proteins), TRITC (for mCherry-tagged proteins), and Cy5 (for FLAG-Parkin visualized with Alexa Fluor 647). Cell nuclei visualized by DAPI staining were quantified using the Analyze Particles function in Fiji (ImageJ), while GFP-, mCh-, or Alexa Fluor 647-positive cells were counted manually. From this, a percentage was calculated to estimate the transfection efficiency.

Bulk Lipid Extraction of Mammalian cells

Bulk lipids were extracted via the Folch method (Folch et al. 1957): cells pellets were lysed with 400uL of cold methanol and thoroughly vortexed before transferring to 15mL glass tubes (DWK73785-15, Sigma Aldrich), to which 800uL of chloroform was added. At this point samples were spiked with internal lipid standards. SPLASH™ LIPIDOMIX™ (Avanti Polar Lipids, Alabaster, AL, USA) was added to all samples, alongside commercially-available 1,2-dipalmitoyl-sn-glycero-3-O-4'-[N,N,N-trimethyl(d9)]-homoserine (DGTS-d9, Avanti Polar Lipids, Alabaster, AL, USA) dissolved in 1:1 acetonitrile:methanol, and/or custom-synthesized (S)-2-ammonio-4-((S)-2,3-bis((hexadecanoyl-'16,16,16-d3)oxy)propoxy)butanoate (DGHS-d6, Avanti Polar Lipids, Alabaster, AL, USA) dissolved in 0.01:0.99 chloroform:methanol, depending on the nature of the experiment. After phase separation with 300uL of 0.9% NaCl (w/v), and centrifugation at 3,000 rpm for 10 min at 4 °C, the organic

phase was collected and re-extracted using chloroform:methanol:H_2O (9.2:147:144 v:v:v). The organic phase was then dried under nitrogen gas by hand.

For lipid analysis using HPLC-MS, dried lipid extracts were dissolved in 400 µl of acetonitrile:methanol = 1:1. For lipid analysis using RSLC Orbitrap MS/MS, dried lipid extracts were weighed and dissolved in buffers A:B (80:20 vol:vol): acetonitrile:H2O (60:40, vol:vol) (buffer A) and isopropanol/acetonitrile (90:10, vol:vol) (buffer B) to reach a final concentration of 1 µg/uL. Resuspended lipid samples were then sonicated for at least 20 min and centrifuged at 10,000 rpm for 5 minutes to pellet any contaminants prior to analysis.

Pulse-Labelling

Cells were grown in Dulbecco's Modified Eagle Medium (DMEM), supplemented with 10% foetal calf serum (FBS) and 1% penicillin–streptomycin with incubation maintained at 37 °C and 5% CO2. 48 hours after transfection, cells were washed twice with 1X PBS before adding modified DMEM (21013024, Thermo Fisher Scientific) supplemented with 10% FBS, 1% penicillin-streptomycin, L-cystine (C7880, Sigma Aldrich) dissolved in sterile MiliQ water, to reach a final concentration of 100mM, GlutaMAX (35050061, Thermo Fisher Scientific), to reach a final concentration of 200mM, and L-methionine (2,3,3,4,4-d5; methyl-d3, Cambridge Isotope Laboratories, MA, USA), to reach final concentration of 100mM. For the mitophagy experiment, a 1mM stock solution of CCCP (ab141229, Abcam) was prepared in sterile dimethyl sulfoxide (DMSO) (D2650, Sigma Aldrich). Just after adding the pulsing media, CCCP was added directly to the dish and thoroughly

mixed to reach a final concentration of 10μM. Cells were harvested at the specified timepoints via trypsinization and counted using the TC20 Automated Cell Counter. Approximately 2 x 10^6 cells were harvested per sample and pelleted for storage at -80°C until lipid extraction.

One-dimensional Thin Layer Chromatography

TLC tanks were saturated with the solvent system, chloroform:acetic acid:water (65:25:4, by vol), for 30 minutes before immersing the lipid-spotted TLC plates. Lipids dissolved in chloroform:methanol 2:1 (v/v) were spotted onto silica gel TLC plates (99571, Sigma Aldrich) and run until the solvent front reached 1cm from the top of the plate. Plates were left to dry in the dark, before spraying with a 0.05% (w/v) primuline dissolved in 80:20 acetone:water. Bands were visualized using 365nm UV light.

Western Blotting

SDS-PAGE gels were prepared using 8% resolving gels overlaid with 5% stacking gels. Transfected cells were lysed directly in their culture dishes using 2x Laemmli sample buffer supplemented with 2-mercaptoethanol. Lysates were collected, vortexed vigorously, and heated at 95 °C for 5 min prior to loading. Samples were resolved by SDS-PAGE under denaturing conditions and transferred onto nitrocellulose membranes using a wet transfer system. Membranes were blocked with 5% milk or PBS-T for 1 hour and incubated with a monoclonal mouse anti-RFP (6G6, ChromoTek) or monoclonal mouse anti-GFP [9F9.F9] (Abcam, ab1218) primary antibody overnight. Membranes were then incubated with a polyclonal goat anti-mouse horseradish peroxidase (HRP)-conjugated secondary antibody (Abcam,

ab6789) for one hour. Protein bands were visualized using SuperSignal™ West Pico PLUS Chemiluminescent Substrate and imaged on an iBright imaging system (Thermo Fisher Scientific).

SIM HPLC-MS

Initial lipidomic analysis was conducted using the Advion AVANT high- performance liquid chromatography (HPLC) instrument coupled with the Advion expression® Compact Mass Spectrometer (CMS) system (Advion, Ithaca, NY, USA). Chromatography was performed on a MultoHigh® 100 Si Hilic column, 5 µm (250 mm x 3 mm) (CS Chromatographie Service GmbH, Langerwehe, Germany). The mobile phase consisted of 53 mM formic acid in acetonitrile (pH 4.2) as solvent A, and 60 mM ammonium formate and 53 mM formic acid in water (pH 3.6) as solvent B. The gradient profile was set as follows: 0-3.5 min: isocratic 10% B, 3.5-30 min: 10-30% B, 30-32 min: isocratic 30% B, 32-32.5 min: 30-10% B, 32.5-35 min: isocratic 10% B. The flow rate and injection volume were 0.5 ml/min and 50 µl, respectively. Identification of lipids was carried out by single quadruple mass spectroscopy (MS), where electrospray ionisation (ESI) was performed in positive mode, and identification conditions were as follows: capillary temperature 250°C; capillary voltage 180V; source voltage offset 20V; source voltage span 30V; source gas temperature 200°C; ESI voltage 3.5kV. Continuous data was acquired from 100-1200*m/z*, with 0.5 second per scan in centroid mode.

Extracted Ion Chromatograms Generation for HPLC-MS Data

Extracted ion chromatograms (EICs) for all selected DGTS and DGHS precursor *m/z* values were visualized using the Advion Mass Express software suite. Raw intensity

traces, which are continuous on single-quadrupole instruments, were exported over the predefined DGTS and DGHS retention-time windows and re-plotted as overlaid chromatograms using custom Python scripts executed in JupyterLab.

DDA RSLC-MS/MS

For subsequent lipidomic analysis, the Dionex UltiMate 3000 RSLC system was coupled to an Orbitrap Eclipse mass spectrometer (Thermo Fisher Scientific) operated in small molecule mode using data-dependent acquisition. Lipids were separated on a C18 column (Acclaim PepMap 100, C18, 75 µm × 15 cm, Thermo Fisher Scientific) maintained at 40°C, using a nano pump at a flow rate of 300 nL/min. Mobile phases consisted of buffers A and B supplemented with 10 mM ammonium formate and 0.1% (v:v) formic acid which were run at a gradient profile set as follows: 0-10 min (80% A), 10-11 min (35% A), 11-27 min (20% A), 27-40 min (1% A), 40-50 min (80% A). For all analyses, samples were first loaded onto a 5 uL sample loop using an autosampler and transferred to a 1 µL injection loop using the loading pump at a flow rate of 2 µL/min.

The ion source was operated with a capillary voltage of 1.9 kV/−2.1 kV and capillary temperature of 320°C, using positive or negative mode ESI accordingly. Full MS scans were acquired over a mass range of 200–2000 *m/z* at a resolution of 120,000, with an AGC target of 4×10^5 ions. MS/MS fragmentation was performed using a stepped normalized collision energy of 25, 30, and 35 (arbitrary units). MS/MS spectra were acquired at a resolution of 15,000 with an AGC target of 5×10^4 ions.

All spectra were acquired with a maximum injection time of 50 ms and a total cycle time for acquisition of approximately 1.5 seconds.

Generation of MS/MS Reference Libraries

MS/MS reference libraries for DGTS and DGHS species (labelled, unlabelled) and the d9DGTS and d6DGHS standard) were generated on LipidEx (version 3) (Hutchins et al. 2018) using the Library Generator module, by consulting the fragmentation spectra obtained via direct-infusion MS/MS using DGTS and DGHS lipid standards, 1,2-dipalmitoyl-sn-glycero-3-O-4'-[N,N,N-trimethyl(d9)]-homoserine (DGTS-d9, Avanti Polar Lipids, Alabaster, AL, USA), and (S)-2-ammonio-4-((S)-2,3-bis((hexadecanoyl-'16,16,16-d3)oxy)propoxy)butanoate (DGHS-d6, Avanti Polar Lipids, Alabaster, AL, USA), respectively. Libraries were subsequently exported from LipidEx as txt files and imported onto MS-DIAL (version 4) software for peak detection and downstream quantification. Libraries for the lipid species found in the internal standard, SPLASH^{TM} LIPIDOMIX, as well as all endogenous lipids found within the mammalian lipidome, were either readily available on MS-DIAL software, or exported from LIPID-MAPS (https://www.lipidmaps.org/).

RSLC-MS/MS Data Processing

Raw MS^1 and MS/MS files generated during acquisition using XCalibur software were analysed using MS-DIAL4-5 software (Tsugawa et al., 2015, 2020). Using MS-DIAL, chromatographic peaks were identified by two-dimensional peak spotting using retention time and accurate mass, followed by deconvolution of MS/MS spectra using the MS2Dec algorithm. This algorithm allows for MS/MS spectra which contain mixtures of fragments to be separated by assigning fragments to precursors

based on shared elution profiles over time. Lipid annotation was performed using a composite score incorporating MS^1-based precursor accurate masses together with MS/MS spectral similarity to the reference libraries. Gaussian error models were applied during similarity scoring to weight deviations in accurate mass, with a standard deviation of 0.5 used to enforce stringent matching and prioritize high-confidence annotations.

For the Su9-*K*/Bta1-eGFP pulse-labelling experiment, feature alignment was performed across all timepoints. Alignment generates a reference peak table from a selected reference sample, which in all cases was set to the final timepoint of the experiment, to maximise the detection of features corresponding to labelled species, assuming unlabelled species would remain sufficiently abundant. Following alignment, missing intensities are addressed using a gap-filling procedure, which re-inspects the raw data at these reference *m/z* and retention-time coordinates, and integrates a local maximum where present.

For all experiments, entries for the following parameters were exported in a txt file format, RT left(min), RT (min), RT right (min), Precursor m/z, Height, Area, S/N, Adduct, Reference RT, Reference m/z, Ontology, RT matched, m/z matched, MS/MS matched, Matched peaks count, S/N, MS^1 isotopes, MS/MS spectrum, with each row corresponding to a single lipid molecular species, e.g. d14DGTS 16:0_16:0. A custom python script was generated on JupyterLab to sort rows within tables based on “Ontology”, which specifies the lipid species of interest (e.g. DGTS,

d14DGTS), as well as on the entry for “MS/MS matched” being “TRUE”, selecting for entries for a given lipid, MS/MS spectral matching confirmed identity rather than MS^1 precursor mass alone. This allowed for lipids to be sorted into tables based on their class. Subsequent de-duplication for all lipid species was performed by selecting the entries with i) the highest “Matched peaks count” and ii) the highest S/N.

Median-of-Ratios Normalization for Su9-*Kl*Bta1-eGFP Pulse-Labelling Experiment

Given that d9DGTS is generated *de novo* during pulse-labelling, it is expected to change across the time-course samples (0h, 30min, 1hr, 2hr, 4hr) and therefore could not be used for normalization across samples. Therefore, to correct for between-sample differences in total signal and technical variability between runs, I computed per-sample size factors using a DESeq-2-style median-of-ratios (MRN) approach using all annotated PC and TAG lipid species detected in all samples, as a reference set. These were sorted using the procedure outlined above. MRN was implemented using a custom Python script run in Jupyter lab. The mathematical operations to obtain these per-sample size factors are explained below.

For each references species, i, and sample, j, let y_{ij}, denote the measured signal intensity. First, a per-species geometric mean, g_i of intensities across all samples was computed:

$$g_i = (y_{i1}y_{i2}y_{i3}y_{i4}y_{i5})^{1/5}$$

For each sample, j, ratios were computed for all reference species:

$$r_{ij} = \frac{y_{ij}}{g_i}$$

The sample-specific size factor, s_j, as shown in Fig.13B, was then defined as the median of these ratios across the reference species set, R:

$$s_j = median_{i \in R}(r_{ij})$$

Finally, normalized intensities for all DGHS, d5DGHS, d6DGTS, d8DGTS, d9DGTS, d11DGTS, and d14DGTS species were obtained by dividing raw intensities by the corresponding sample size factor:

$$y'_{ij} = \frac{y_{ij}}{s_j}$$

References

Abeliovich, A., & Gitler, A. D. (2016). Defects in trafficking bridge Parkinson's disease pathology and genetics. *Nature*, *539*(7628), 207–216.

Agrimi, G., Di Noia, M. A., Marobbio, C. M. T., Fiermonte, G., Lasorsa, F. M., & Palmieri, F. (2004). Identification of the human mitochondrial S-adenosylmethionine transporter: bacterial expression, reconstitution, functional characterization and tissue distribution. *The Biochemical Journal*, *379*(Pt 1), 183–190.

Ahmad, T., Aggarwal, K., Pattnaik, B., Mukherjee, S., Sethi, T., Tiwari, B. K., Kumar, M., Micheal, A., Mabalirajan, U., Ghosh, B., Sinha Roy, S., & Agrawal, A. (2013). Computational classification of mitochondrial shapes reflects stress and redox state. *Cell Death & Disease*, *4*(1), e461.

AhYoung, A. P., Lu, B., Cascio, D., & Egea, P. F. (2017). Crystal structure of Mdm12 and combinatorial reconstitution of Mdm12/Mmm1 ERMES complexes for structural studies. *Biochemical and Biophysical Research Communications*, *488*(1), 129–135.

Anders, S., & Huber, W. (2010). Differential expression analysis for sequence count data. *Genome Biology*, *11*(10), R106.

Baba, K., Kuwada, S., Nakao, A., Li, X., Okuda, N., Nishida, A., Mitsuda, S., Fukuoka, N., Kakeya, H., & Kataoka, T. (2020). Different localization of lysosomal-associated membrane protein 1 (LAMP1) in mammalian cultured cell lines. *Histochemistry and Cell Biology*, *153*(4), 199–213.

Birner, R., Bürgermeister, M., Schneiter, R., & Daum, G. (2001). Roles of phosphatidylethanolamine and of its several biosynthetic pathways in Saccharomyces cerevisiae. *Molecular Biology of the Cell*, *12*(4), 997–1007.

Bolik, S., Schlaich, A., Mukhina, T., Amato, A., Bastien, O., Schneck, E., Demé, B., & Jouhet, J. (2023). Lipid bilayer properties potentially contributed to the evolutionary disappearance of betaine lipids in seed plants. *BMC Biology*, *21*(1), 275.

Bonifacino, J. S., & Glick, B. S. (2004). The mechanisms of vesicle budding and fusion. *Cell*, *116*(2), 153–166.

Bonifacino, J. S., & Traub, L. M. (2003). Signals for sorting of transmembrane proteins to endosomes and lysosomes. *Annual Review of Biochemistry*, *72*(1), 395–447.

Bosch Grau, M., Gonzalez Curto, G., Rocha, C., Magiera, M. M., Marques Sousa, P., Giordano, T., Spassky, N., & Janke, C. (2013). Tubulin glycylases and glutamylases have distinct functions in stabilization and motility of ependymal cilia. *The Journal of Cell Biology*, *202*(3), 441–451.

Carlsson, S. R., Roth, J., Piller, F., & Fukuda, M. (1988). Isolation and characterization of human lysosomal membrane glycoproteins, h-lamp-1 and h-lamp-2. Major sialoglycoproteins carrying polylactosaminoglycan. *The Journal of Biological Chemistry*, *263*(35), 18911–18919.

Chan, E. Y. L., & McQuibban, G. A. (2012). Phosphatidylserine decarboxylase 1 (Psd1) promotes mitochondrial fusion by regulating the biophysical properties of the mitochondrial membrane and alternative topogenesis of mitochondrial genome maintenance protein 1 (Mgm1). *The Journal of Biological Chemistry*, *287*(48), 40131–40139.

Chang, C.-L., Hsieh, T.-S., Yang, T. T., Rothberg, K. G., Azizoglu, D. B., Volk, E., Liao, J.-C., & Liou, J. (2013). Feedback regulation of receptor-induced Ca2+ signaling mediated by E-Syt1 and Nir2 at endoplasmic reticulum-plasma membrane junctions. *Cell Reports*, *5*(3), 813–825.

Chen, S., Liu, Y., & Yu, H. (2025a). Uncovering the mechanisms of intracellular membrane trafficking by reconstituted membrane systems. *Membranes*, *15*(5), 154.

Chen, S., Liu, Y., & Yu, H. (2025b). Uncovering the mechanisms of intracellular membrane trafficking by reconstituted membrane systems. *Membranes*, *15*(5),

154.

Chung, J., Torta, F., Masai, K., Lucast, L., Czapla, H., Tanner, L. B., Narayanaswamy, P., Wenk, M. R., Nakatsu, F., & De Camilli, P. (2015a). INTRACELLULAR TRANSPORT. PI4P/phosphatidylserine countertransport at ORP5- and ORP8-mediated ER-plasma membrane contacts. *Science (New York, N.Y.)*, *349*(6246), 428–432.

Chung, J., Torta, F., Masai, K., Lucast, L., Czapla, H., Tanner, L. B., Narayanaswamy, P., Wenk, M. R., Nakatsu, F., & De Camilli, P. (2015b). INTRACELLULAR TRANSPORT. PI4P/phosphatidylserine countertransport at ORP5- and ORP8-mediated ER-plasma membrane contacts. *Science (New York, N.Y.)*, *349*(6246), 428–432.

Coleman, J. A., Quazi, F., & Molday, R. S. (2013). Mammalian P4-ATPases and ABC transporters and their role in phospholipid transport. *Biochimica et Biophysica Acta*, *1831*(3), 555–574.

Covill-Cooke, C., Hirashima, T., Kawano, S., Ganellin, J., Moody, A., van Schie, S. N. S., John Peter, A. T., Saito, C., Endo, T., & Kornmann, B. (2024). Compositional flexibility of the ER-mitochondria encounter structure. In *bioRxiv*. bioRxiv. https://doi.org/10.1101/2024.11.26.625358

Cullis, P. R., & de Kruijff, B. (1979). Lipid polymorphism and the functional roles of lipids in biological membranes. *Biochimica et Biophysica Acta*, *559*(4), 399–420.

de Saint-Jean, M., Delfosse, V., Douguet, D., Chicanne, G., Payrastre, B., Bourguet, W., Antonny, B., & Drin, G. (2011). Osh4p exchanges sterols for phosphatidylinositol 4-phosphate between lipid bilayers. *The Journal of Cell Biology*, *195*(6), 965–978.

Denison, S. R., Wang, F., Becker, N. A., Schüle, B., Kock, N., Phillips, L. A., Klein, C., & Smith, D. I. (2003). Alterations in the common fragile site gene Parkin in ovarian and other cancers. *Oncogene*, *22*(51), 8370–8378.

Donkor, J., Sariahmetoglu, M., Dewald, J., Brindley, D. N., & Reue, K. (2007). Three mammalian lipins act as phosphatidate phosphatases with distinct tissue expression patterns. *The Journal of Biological Chemistry*, *282*(6), 3450–3457.

Ejsing, C. S., Sampaio, J. L., Surendranath, V., Duchoslav, E., Ekroos, K., Klemm, R. W., Simons, K., & Shevchenko, A. (2009). Global analysis of the yeast lipidome by quantitative shotgun mass spectrometry. *Proceedings of the National Academy of Sciences of the United States of America*, *106*(7), 2136–2141.

Ernst, R., Ejsing, C. S., & Antonny, B. (2016). Homeoviscous adaptation and the regulation of membrane lipids. *Journal of Molecular Biology*, *428*(24 Pt A), 4776–4791.

Falzone, M. E., Malvezzi, M., Lee, B.-C., & Accardi, A. (2018). Known structures and unknown mechanisms of TMEM16 scramblases and channels. *The Journal of General Physiology*, *150*(7), 933–947.

Folch, J., Lees, M., & Sloane Stanley, G. H. (1957). A simple method for the isolation and purification of total lipides from animal tissues. *The Journal of Biological Chemistry*, *226*(1), 497–509.

Friedman, J. R., Kannan, M., Toulmay, A., Jan, C. H., Weissman, J. S., Prinz, W. A., & Nunnari, J. (2018). Lipid homeostasis is maintained by dual targeting of the mitochondrial PE biosynthesis enzyme to the ER. *Developmental Cell*, *44*(2), 261-270.e6.

Glasgow, R. I. C., Singh, V., Peña-Pérez, L., Wilhalm, A., Moedas, M. F., Moore,

D., Rosenberger, F. A., Li, X., Atanassov, I., Saba, M., Cipullo, M., Rorbach, J., Wedell, A., Freyer, C., Amunts, A., & Wredenberg, A. (2025). The mitochondrial methylation potential gates mitoribosome assembly. *Nature Communications*, *16*(1), 5388.

Golla, V. K., Boyd, K. J., & May, E. R. (2024). Curvature sensing lipid dynamics in a mitochondrial inner membrane model. *Communications Biology*, *7*(1), 29.

Greene, A. W., Grenier, K., Aguileta, M. A., Muise, S., Farazifard, R., Haque, M. E., McBride, H. M., Park, D. S., & Fon, E. A. (2012). Mitochondrial processing peptidase regulates PINK1 processing, import and Parkin recruitment. *EMBO Reports*, *13*(4), 378–385.

Guillén-Samander, A., Leonzino, M., Hanna, M. G., Tang, N., Shen, H., & De Camilli, P. (2021). Correction: VPS13D bridges the ER to mitochondria and peroxisomes via Miro. *The Journal of Cell Biology*, *220*(8). https://doi.org/10.1083/jcb.20201000405052021c

Harris, E. H. (2001). Chlamydomonas as a model organism. *Annual Review of Plant Physiology and Plant Molecular Biology*, *52*(1), 363–406.

Hewlett, B., Singh, N. P., Vannier, C., & Galli, T. (2021). ER-PM contact sites - SNARING actors in emerging functions. *Frontiers in Cell and Developmental Biology*, *9*, 635518.

Hoffmann, D. Y., & Shachar-Hill, Y. (2023). Do betaine lipids replace phosphatidylcholine as fatty acid editing hubs in microalgae? *Frontiers in Plant Science*, *14*, 1077347.

Hollenstein, D. M., & Kraft, C. (2020). Autophagosomes are formed at a distinct cellular structure. *Current Opinion in Cell Biology*, *65*, 50–57.

Holthuis, J. C. M., & Menon, A. K. (2014). Lipid landscapes and pipelines in membrane homeostasis. *Nature*, *510*(7503), 48–57.

Houtkooper, R. H., & Vaz, F. M. (2008a). Cardiolipin, the heart of mitochondrial metabolism. *Cellular and Molecular Life Sciences*, *65*(16), 2493–2506.

Houtkooper, R. H., & Vaz, F. M. (2008b). Cardiolipin, the heart of mitochondrial metabolism. *Cellular and Molecular Life Sciences*, *65*(16), 2493–2506.

Hutchins, P. D., Russell, J. D., & Coon, J. J. (2018). LipiDex: An integrated software package for high-confidence lipid identification. *Cell Systems*, *6*(5), 621-625.e5.

Ikon, N., & Ryan, R. O. (2017). Cardiolipin and mitochondrial cristae organization. *Biochimica et Biophysica Acta. Biomembranes*, *1859*(6), 1156–1163.

John Peter, A. T., Petrungaro, C., Peter, M., & Kornmann, B. (2022). METALIC reveals interorganelle lipid flux in live cells by enzymatic mass tagging. *Nature Cell Biology*, *24*(6), 996–1004.

Jumper, J., Evans, R., Pritzel, A., Green, T., Figurnov, M., Ronneberger, O., Tunyasuvunakool, K., Bates, R., Žídek, A., Potapenko, A., Bridgland, A., Meyer, C., Kohl, S. A. A., Ballard, A. J., Cowie, A., Romera-Paredes, B., Nikolov, S., Jain, R., Adler, J., … Hassabis, D. (2021). Highly accurate protein structure prediction with AlphaFold. *Nature*, *596*(7873), 583–589.

Kamerkar, S., Singh, J., Tripathy, S., Bhonsle, H., Kumar, M., & Mallik, R. (2021). In-vitro Reconstitution of Membrane Contact Sites between the Endoplasmic Reticulum and Lipid Droplets. In *Cell Biology* (biorxiv;2021.06.07.447315v1). bioRxiv. https://www.biorxiv.org/content/10.1101/2021.06.07.447315v1.full

Kaplan, M. R., & Simoni, R. D. (1985a). Transport of cholesterol from the endoplasmic reticulum to the plasma membrane. *The Journal of Cell Biology*, *101*(2), 446–453.

Kaplan, M. R., & Simoni, R. D. (1985b). Transport of cholesterol from the endoplasmic reticulum to the plasma membrane. *The Journal of Cell Biology*, *101*(2), 446–453.

Kasianowicz, J., Benz, R., & McLaughlin, S. (1984). The kinetic mechanism by which CCCP (carbonyl cyanide m-chlorophenylhydrazone) transports protons across membranes. *The Journal of Membrane Biology*, *82*(2), 179–190.

Kawano, S., Tamura, Y., Kojima, R., Bala, S., Asai, E., Michel, A. H., Kornmann, B., Riezman, I., Riezman, H., Sakae, Y., Okamoto, Y., & Endo, T. (2018). Structure-function insights into direct lipid transfer between membranes by Mmm1-Mdm12 of ERMES. *The Journal of Cell Biology*, *217*(3), 959–974.

Kim, J. H., Lee, S.-R., Li, L.-H., Park, H.-J., Park, J.-H., Lee, K. Y., Kim, M.-K., Shin, B. A., & Choi, S.-Y. (2011). High cleavage efficiency of a 2A peptide derived from porcine teschovirus-1 in human cell lines, zebrafish and mice. *PloS One*, *6*(4), e18556.

Kim, Y. J., Guzman-Hernandez, M.-L., Wisniewski, E., & Balla, T. (2015). Phosphatidylinositol-phosphatidic acid exchange by Nir2 at ER-PM contact sites maintains phosphoinositide signaling competence. *Developmental Cell*, *33*(5), 549–561.

Kolehmainen, J., Black, G. C. M., Saarinen, A., Chandler, K., Clayton-Smith, J., Träskelin, A.-L., Perveen, R., Kivitie-Kallio, S., Norio, R., Warburg, M., Fryns, J.-P., de la Chapelle, A., & Lehesjoki, A.-E. (2003). Cohen syndrome is caused by

mutations in a novel gene, COH1, encoding a transmembrane protein with a presumed role in vesicle-mediated sorting and intracellular protein transport. *American Journal of Human Genetics*, *72*(6), 1359–1369.

Kopec, K. O., Alva, V., & Lupas, A. N. (2010). Homology of SMP domains to the TULIP superfamily of lipid-binding proteins provides a structural basis for lipid exchange between ER and mitochondria. *Bioinformatics (Oxford, England)*, *26*(16), 1927–1931.

Kornmann, B., Currie, E., Collins, S. R., Schuldiner, M., Nunnari, J., Weissman, J. S., & Walter, P. (2009a). An ER-mitochondria tethering complex revealed by a synthetic biology screen. *Science (New York, N.Y.)*, *325*(5939), 477–481.

Kornmann, B., Currie, E., Collins, S. R., Schuldiner, M., Nunnari, J., Weissman, J. S., & Walter, P. (2009b). An ER-mitochondria tethering complex revealed by a synthetic biology screen. *Science (New York, N.Y.)*, *325*(5939), 477–481.

Kumar, N., Leonzino, M., Hancock-Cerutti, W., Horenkamp, F. A., Li, P., Lees, J. A., Wheeler, H., Reinisch, K. M., & De Camilli, P. (2018). VPS13A and VPS13C are lipid transport proteins differentially localized at ER contact sites. *The Journal of Cell Biology*, *217*(10), 3625–3639.

Künzler, K., & Eichenberger, W. (1997). Betaine lipids and zwitterionic phospholipids in plants and fungi. *Phytochemistry*, *46*(5), 883–892.

Lang, A. B., John Peter, A. T., Walter, P., & Kornmann, B. (2015). ER-mitochondrial junctions can be bypassed by dominant mutations in the endosomal protein Vps13. *The Journal of Cell Biology*, *210*(6), 883–890.

Lee, S.-K., Ham, H.-J., Park, S., Lee, H. E., Mun, J. Y., Jang, D.-J., & Lee, J.-A. (2025). VPS13B recruits lipid vesicles to promote mitochondrial fission and quality

control. *Nature Communications*, 1–15.

Lesage, S., Drouet, V., Majounie, E., Deramecourt, V., Jacoupy, M., Nicolas, A., Cormier-Dequaire, F., Hassoun, S. M., Pujol, C., Ciura, S., Erpapazoglou, Z., Usenko, T., Maurage, C.-A., Sahbatou, M., Liebau, S., Ding, J., Bilgic, B., Emre, M., Erginel-Unaltuna, N., … International Parkinson's Disease Genomics Consortium (IPDGC). (2016). Loss of VPS13C function in autosomal-recessive parkinsonism causes mitochondrial dysfunction and increases PINK1/Parkin-dependent mitophagy. *American Journal of Human Genetics*, *98*(3), 500–513.

Lin, Y., Laurent, C., Lambert, C., Van Schie, S. N. S., Michel, A.H, Kornmann, B., (2026). BLT: a versatile *in vivo* platform for quantitative analysis and genetic dissection of organelle-specific lipid transport, *In preparation*

Liu, X., & Hajnóczky, G. (2011). Altered fusion dynamics underlie unique morphological changes in mitochondria during hypoxia-reoxygenation stress. *Cell Death and Differentiation*, *18*(10), 1561–1572.

Loewen, C. J. R., Roy, A., & Levine, T. P. (2003a). A conserved ER targeting motif in three families of lipid binding proteins and in Opi1p binds VAP. *The EMBO Journal*, *22*(9), 2025–2035.

Loewen, C. J. R., Roy, A., & Levine, T. P. (2003b). A conserved ER targeting motif in three families of lipid binding proteins and in Opi1p binds VAP. *The EMBO Journal*, *22*(9), 2025–2035.

Long, Q., Zhao, D., Fan, W., Yang, L., Zhou, Y., Qi, J., Wang, X., & Liu, X. (2015). Modeling of mitochondrial donut formation. *Biophysical Journal*, *109*(5), 892–899.

Mari, M., Tooze, S. A., & Reggiori, F. (2011). The puzzling origin of the autophagosomal membrane. *F1000 Biology Reports*, *3*, 25.

Martin, J., Mahlke, K., & Pfanner, N. (1991). Role of an energized inner membrane in mitochondrial protein import. Delta psi drives the movement of presequences. *The Journal of Biological Chemistry*, *266*(27), 18051–18057.

Mesmin, B., Bigay, J., Moser von Filseck, J., Lacas-Gervais, S., Drin, G., & Antonny, B. (2013). A four-step cycle driven by PI(4)P hydrolysis directs sterol/PI(4)P exchange by the ER-Golgi tether OSBP. *Cell*, *155*(4), 830–843.

Michel, A. H., & Kornmann, B. (2022). SAturated Transposon Analysis in Yeast (SATAY) for deep functional mapping of Yeast genomes. *Methods in Molecular Biology (Clifton, N.J.)*, *2477*, 349–379.

Moessinger, C., Klizaite, K., Steinhagen, A., Philippou-Massier, J., Shevchenko, A., Hoch, M., Ejsing, C. S., & Thiele, C. (2014). Two different pathways of phosphatidylcholine synthesis, the Kennedy Pathway and the Lands Cycle, differentially regulate cellular triacylglycerol storage. *BMC Cell Biology*, *15*(1), 43.

Moser von Filseck, J., Čopič, A., Delfosse, V., Vanni, S., Jackson, C. L., Bourguet, W., & Drin, G. (2015). INTRACELLULAR TRANSPORT. Phosphatidylserine transport by ORP/Osh proteins is driven by phosphatidylinositol 4-phosphate. *Science (New York, N.Y.)*, *349*(6246), 432–436.

Murley, A., Sarsam, R. D., Toulmay, A., Yamada, J., Prinz, W. A., & Nunnari, J. (2015). Ltc1 is an ER-localized sterol transporter and a component of ER-mitochondria and ER-vacuole contacts. *The Journal of Cell Biology*, *209*(4), 539–548.

Narendra, D., Tanaka, A., Suen, D.-F., & Youle, R. J. (2008). Parkin is recruited selectively to impaired mitochondria and promotes their autophagy. *The Journal of Cell Biology*, *183*(5), 795–803.

Nath, V. R., Mishra, S., Basak, B., Trivedi, D., & Raghu, P. (2020). Extended synaptotagmin regulates membrane contact site structure and lipid transfer function in vivo. *EMBO Reports*, *21*(9), e50264.

Nishimura, T., & Stefan, C. J. (2020). Specialized ER membrane domains for lipid metabolism and transport. *Biochimica et Biophysica Acta. Molecular and Cell Biology of Lipids*, *1865*(1), 158492.

Okuda, S., Freinkman, E., & Kahne, D. (2012). Cytoplasmic ATP hydrolysis powers transport of lipopolysaccharide across the periplasm in E. coli. *Science (New York, N.Y.)*, *338*(6111), 1214–1217.

Paillusson, S., Stoica, R., Gomez-Suaga, P., Lau, D. H. W., Mueller, S., Miller, T., & Miller, C. C. J. (2016). There's something wrong with my MAM; The ER-mitochondria axis and neurodegenerative diseases. *Trends in Neurosciences*, *39*(3), 146–157.

Pfeiffer, K., Gohil, V., Stuart, R. A., Hunte, C., Brandt, U., Greenberg, M. L., & Schägger, H. (2003). Cardiolipin stabilizes respiratory chain supercomplexes. *The Journal of Biological Chemistry*, *278*(52), 52873–52880.

Prinz, W. A. (2014). Bridging the gap: membrane contact sites in signaling, metabolism, and organelle dynamics. *The Journal of Cell Biology*, *205*(6), 759–769.

Quirós, P. M., Langer, T., & López-Otín, C. (2015). New roles for mitochondrial proteases in health, ageing and disease. *Nature Reviews. Molecular Cell Biology*, *16*(6), 345–359.

Rakusanova, S., & Cajka, T. (2024). Tips and tricks for LC–MS-based

metabolomics and lipidomics analysis. *Trends in Analytical Chemistry: TRAC*, *180*(117940), 117940.

Raychaudhuri, S., Im, Y. J., Hurley, J. H., & Prinz, W. A. (2006). Nonvesicular sterol movement from plasma membrane to ER requires oxysterol-binding protein-related proteins and phosphoinositides. *The Journal of Cell Biology*, *173*(1), 107–119.

Riekhof, W. R., Andre, C., & Benning, C. (2005). Two enzymes, BtaA and BtaB, are sufficient for betaine lipid biosynthesis in bacteria. *Archives of Biochemistry and Biophysics*, *441*(1), 96–105.

Riekhof, W. R., Naik, S., Bertrand, H., Benning, C., & Voelker, D. R. (2014). Phosphate starvation in fungi induces the replacement of phosphatidylcholine with the phosphorus-free betaine lipid diacylglyceryl-N,N,N-trimethylhomoserine. *Eukaryotic Cell*, *13*(6), 749–757.

Riekhof, W. R., Sears, B. B., & Benning, C. (2005a). Annotation of genes involved in glycerolipid biosynthesis in Chlamydomonas reinhardtii: discovery of the betaine lipid synthase BTA1Cr. *Eukaryotic Cell*, *4*(2), 242–252.

Riekhof, W. R., Sears, B. B., & Benning, C. (2005b). Annotation of genes involved in glycerolipid biosynthesis in Chlamydomonas reinhardtii: discovery of the betaine lipid synthase BTA1Cr. *Eukaryotic Cell*, *4*(2), 242–252.

Róg, T., Martinez-Seara, H., Munck, N., Oresic, M., Karttunen, M., & Vattulainen, I. (2009). Role of cardiolipins in the inner mitochondrial membrane: insight gained through atom-scale simulations. *The Journal of Physical Chemistry. B*, *113*(11), 3413–3422.

Rohrer, J., Schweizer, A., Russell, D., & Kornfeld, S. (1996). The targeting of

Lamp1 to lysosomes is dependent on the spacing of its cytoplasmic tail tyrosine sorting motif relative to the membrane. *The Journal of Cell Biology*, *132*(4), 565–576.

Saheki, Y., Bian, X., Schauder, C. M., Sawaki, Y., Surma, M. A., Klose, C., Pincet, F., Reinisch, K. M., & De Camilli, P. (2016). Control of plasma membrane lipid homeostasis by the extended synaptotagmins. *Nature Cell Biology*, *18*(5), 504–515.

Santos, A. X. S., & Riezman, H. (2012a). Yeast as a model system for studying lipid homeostasis and function. *FEBS Letters*, *586*(18), 2858–2867.

Santos, A. X. S., & Riezman, H. (2012b). Yeast as a model system for studying lipid homeostasis and function. *FEBS Letters*, *586*(18), 2858–2867.

Schauder, C. M., Wu, X., Saheki, Y., Narayanaswamy, P., Torta, F., Wenk, M. R., De Camilli, P., & Reinisch, K. M. (2014). Structure of a lipid-bound extended synaptotagmin indicates a role in lipid transfer. *Nature*, *510*(7506), 552–555.

Schlame, M. (2008). Thematic Review Series: Glycerolipids. Cardiolipin synthesis for the assembly of bacterial and mitochondrial membranes. *Journal of Lipid Research*, *49*(8), 1607–1620.

Schlame, M., & Greenberg, M. L. (2017). Biosynthesis, remodeling and turnover of mitochondrial cardiolipin. *Biochimica et Biophysica Acta. Molecular and Cell Biology of Lipids*, *1862*(1), 3–7.

Schröder, L. F., Peng, W., Gao, G., Wong, Y. C., Schwake, M., & Krainc, D. (2024). VPS13C regulates phospho-Rab10-mediated lysosomal function in human dopaminergic neurons. *The Journal of Cell Biology*, *223*(5). https://doi.org/10.1083/jcb.202304042

Seong, E., Insolera, R., Dulovic, M., Kamsteeg, E.-J., Trinh, J., Brüggemann, N., Sandford, E., Li, S., Ozel, A. B., Li, J. Z., Jewett, T., Kievit, A. J. A., Münchau, A., Shakkottai, V., Klein, C., Collins, C. A., Lohmann, K., van de Warrenburg, B. P., & Burmeister, M. (2018). Mutations in VPS13D lead to a new recessive ataxia with spasticity and mitochondrial defects. *Annals of Neurology*, *83*(6), 1075–1088.

Shaner, N. C., Campbell, R. E., Steinbach, P. A., Giepmans, B. N. G., Palmer, A. E., & Tsien, R. Y. (2004). Improved monomeric red, orange and yellow fluorescent proteins derived from Discosoma sp. red fluorescent protein. *Nature Biotechnology*, *22*(12), 1567–1572.

Sherman, F. (2002). Getting started with yeast. *Methods in Enzymology*, *350*, 3–41.

Shiao, Y. J., Lupo, G., & Vance, J. E. (1995). Evidence that phosphatidylserine is imported into mitochondria via a mitochondria-associated membrane and that the majority of mitochondrial phosphatidylethanolamine is derived from decarboxylation of phosphatidylserine. *The Journal of Biological Chemistry*, *270*(19), 11190–11198.

Shiino, H., Furuta, S., Kojima, R., Kimura, K., Endo, T., & Tamura, Y. (2021). Phosphatidylserine flux into mitochondria unveiled by organelle-targeted Escherichia coli phosphatidylserine synthase PssA. *The FEBS Journal*, *288*(10), 3285–3299.

Smirnova, E., Griparic, L., Shurland, D. L., & van der Bliek, A. M. (2001). Dynamin-related protein Drp1 is required for mitochondrial division in mammalian cells. *Molecular Biology of the Cell*, *12*(8), 2245–2256.

Stefan, C. J., Trimble, W. S., Grinstein, S., Drin, G., Reinisch, K., De Camilli, P.,

Cohen, S., Valm, A. M., Lippincott-Schwartz, J., Levine, T. P., Iaea, D. B., Maxfield, F. R., Futter, C. E., Eden, E. R., Judith, D., van Vliet, A. R., Agostinis, P., Tooze, S. A., Sugiura, A., & McBride, H. M. (2017). Membrane dynamics and organelle biogenesis-lipid pipelines and vesicular carriers. *BMC Biology*, *15*(1), 102.

Suzuki, J., Denning, D. P., Imanishi, E., Horvitz, H. R., & Nagata, S. (2013). Xk-related protein 8 and CED-8 promote phosphatidylserine exposure in apoptotic cells. *Science (New York, N.Y.)*, *341*(6144), 403–406.

Tilokani, L., Nagashima, S., Paupe, V., & Prudent, J. (2018). Mitochondrial dynamics: overview of molecular mechanisms. *Essays in Biochemistry*, *62*(3), 341–360.

Tong, J., Manik, M. K., & Im, Y. J. (2018). Structural basis of sterol recognition and nonvesicular transport by lipid transfer proteins anchored at membrane contact sites. *Proceedings of the National Academy of Sciences of the United States of America*, *115*(5), E856–E865.

Tsugawa, H., Cajka, T., Kind, T., Ma, Y., Higgins, B., Ikeda, K., Kanazawa, M., VanderGheynst, J., Fiehn, O., & Arita, M. (2015). MS-DIAL: data-independent MS/MS deconvolution for comprehensive metabolome analysis. *Nature Methods*, *12*(6), 523–526.

Tsugawa, H., Ikeda, K., Takahashi, M., Satoh, A., Mori, Y., Uchino, H., Okahashi, N., Yamada, Y., Tada, I., Bonini, P., Higashi, Y., Okazaki, Y., Zhou, Z., Zhu, Z.-J., Koelmel, J., Cajka, T., Fiehn, O., Saito, K., Arita, M., & Arita, M. (2020). A lipidome atlas in MS-DIAL 4. *Nature Biotechnology*, *38*(10), 1159–1163.

Ueno, S., Maruki, Y., Nakamura, M., Tomemori, Y., Kamae, K., Tanabe, H., Yamashita, Y., Matsuda, S., Kaneko, S., & Sano, A. (2001). The gene encoding a newly discovered protein, chorein, is mutated in chorea-acanthocytosis. *Nature*

Genetics, *28*(2), 121–122.

Ugur, B., Schueder, F., Shin, J., Hanna, M. G., Wu, Y., Leonzino, M., Su, M., McAdow, A. R., Wilson, C., Postlethwait, J., Solnica-Krezel, L., Bewersdorf, J., & De Camilli, P. (2024a). VPS13B is localized at the interface between Golgi cisternae and is a functional partner of FAM177A1. *The Journal of Cell Biology*, *223*(12). https://doi.org/10.1083/jcb.202311189

Ugur, B., Schueder, F., Shin, J., Hanna, M. G., Wu, Y., Leonzino, M., Su, M., McAdow, A. R., Wilson, C., Postlethwait, J., Solnica-Krezel, L., Bewersdorf, J., & De Camilli, P. (2024b). VPS13B is localized at the interface between Golgi cisternae and is a functional partner of FAM177A1. *The Journal of Cell Biology*, *223*(12). https://doi.org/10.1083/jcb.202311189

Um, J.-H., Kim, Y. Y., Finkel, T., & Yun, J. (2018). Sensitive measurement of mitophagy by flow cytometry using the pH-dependent fluorescent reporter mt-Keima. *Journal of Visualized Experiments: JoVE*, *138*. https://doi.org/10.3791/58099

Voeltz, G. K., Sawyer, E. M., Hajnóczky, G., & Prinz, W. A. (2024). Making the connection: How membrane contact sites have changed our view of organelle biology. *Cell*, *187*(2), 257–270.

Walsh, I. M., Bowman, M. A., Soto Santarriaga, I. F., Rodriguez, A., & Clark, P. L. (2020). Synonymous codon substitutions perturb cotranslational protein folding in vivo and impair cell fitness. *Proceedings of the National Academy of Sciences of the United States of America*, *117*(7), 3528–3534.

Wang, X., & Chen, X. J. (2015). A cytosolic network suppressing mitochondria-mediated proteostatic stress and cell death. *Nature*, *524*(7566), 481–484.

Wang, Y., Wang, F., Wang, R., Zhao, P., & Xia, Q. (2015). 2A self-cleaving peptide-based multi-gene expression system in the silkworm Bombyx mori. *Scientific Reports*, *5*(1), 16273.

Wirtz, K. W., & Zilversmit, D. B. (1968). Exchange of phospholipids between liver mitochondria and microsomes in vitro. *The Journal of Biological Chemistry*, *243*(13), 3596–3602.

Wong, L. H., Gatta, A. T., & Levine, T. P. (2019). Lipid transfer proteins: the lipid commute via shuttles, bridges and tubes. *Nature Reviews. Molecular Cell Biology*, *20*(2), 85–101.

Wong, L. H., & Levine, T. P. (2016). Lipid transfer proteins do their thing anchored at membrane contact sites… but what is their thing? *Biochemical Society Transactions*, *44*(2), 517–527.

Wozny, M. R., Di Luca, A., Morado, D. R., Picco, A., Khaddaj, R., Campomanes, P., Ivanović, L., Hoffmann, P. C., Miller, E. A., Vanni, S., & Kukulski, W. (2023). In situ architecture of the ER-mitochondria encounter structure. *Nature*, *618*(7963), 188–192.

Wrobel, L., Topf, U., Bragoszewski, P., Wiese, S., Sztolsztener, M. E., Oeljeklaus, S., Varabyova, A., Lirski, M., Chroscicki, P., Mroczek, S., Januszewicz, E., Dziembowski, A., Koblowska, M., Warscheid, B., & Chacinska, A. (2015). Mistargeted mitochondrial proteins activate a proteostatic response in the cytosol. *Nature*, *524*(7566), 485–488.

Yoshii, S. R., Kishi, C., Ishihara, N., & Mizushima, N. (2011). Parkin mediates proteasome-dependent protein degradation and rupture of the outer mitochondrial membrane. *The Journal of Biological Chemistry*, *286*(22), 19630–19640.

Yu, C.-H., Dang, Y., Zhou, Z., Wu, C., Zhao, F., Sachs, M. S., & Liu, Y. (2015). Codon usage influences the local rate of translation elongation to regulate co-translational protein folding. *Molecular Cell*, *59*(5), 744–754.

(N.d.). Retrieved January 4, 2026, from https://www.researchgate.net/publication/46111073_The_origin_of_the_autophagosomal_membrane

Appendix

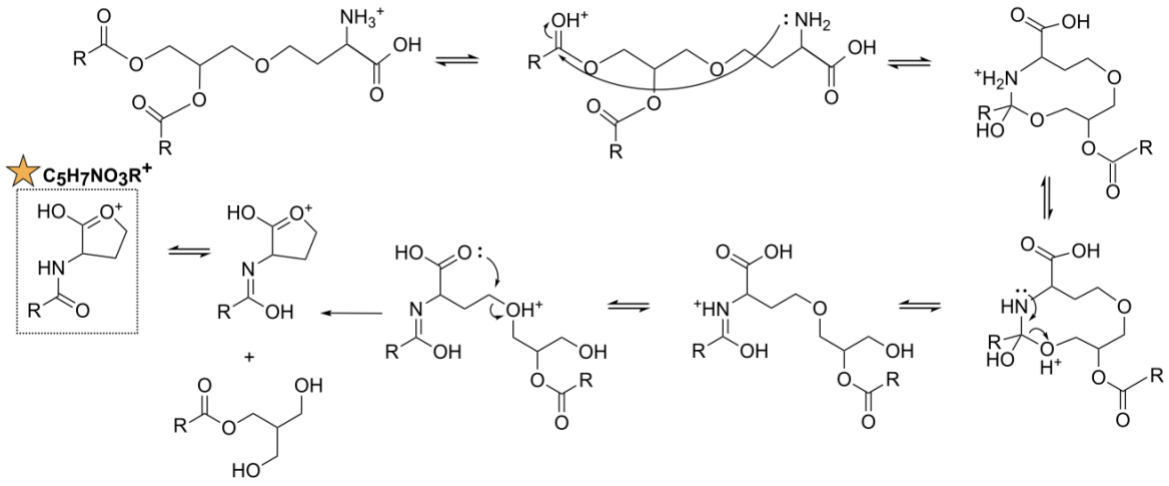

Supplementary Figure 1. Putative gas-phase intramolecular rearrangement of protonated DGHS. This proposed mechanism generates the boxed product ion, $C_5H_7NO_3R^+$, for which m/z = 129.04 + exact mass of R, where R denotes the hydrocarbon chain of one fatty acyl substituent, $C_nH_{2n-2m+1}$, with *n* equal to the number of carbons and *m*, the number of double bonds. For R = $C_{15}H_{31}$, corresponding to the 16:0 acyl chain of the DGHS 16:0/16:0 standard, this fragment is observed at m/z 340.28.

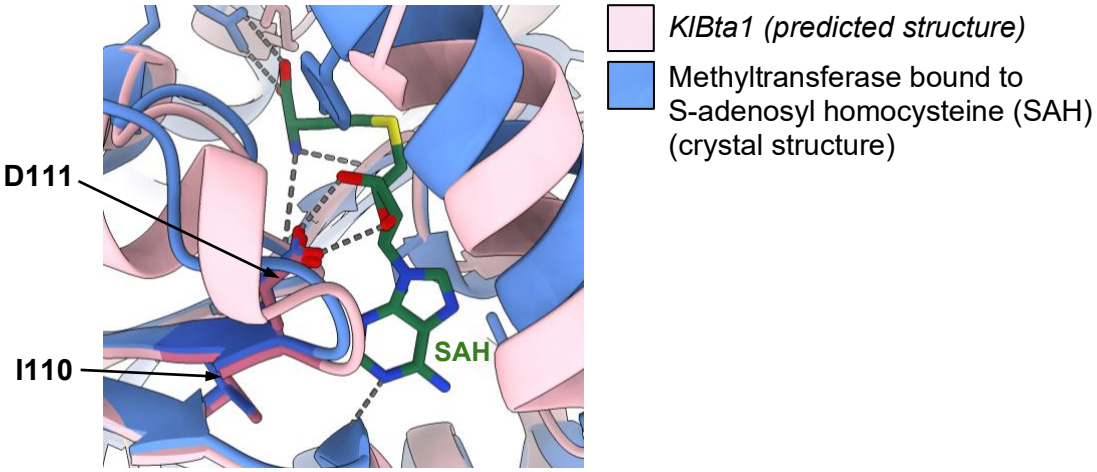

Supplementary Figure 2. Close-up view of SAM-binding residues to be mutated by alanine-mutagenesis in predicted structure of *Kl*Bta1 (pink). The structure is overlayed with the crystal structure of a methyltransferase bound to S-adenosyl homocysteine (green, PDB: 5UFN). Dashed lines indicate predicted hydrogen bonds between residues and SAH.